Master's thesis

NTNU
Norwegian University of Science and Technology
Faculty of Engineering
Department of Marine Technology

Anders Falsen Habostad

Assessment of design methods for structural response of floating wind turbines with focus on mooring line tension

Master's thesis in Marine Technology
Supervisor: Kjell Larsen and Sverre Haver
June 2019

NTNU
Norwegian University of
Science and Technology

Anders Falsen Habostad

Assessment of design methods for structural response of floating wind turbines with focus on mooring line tension

Master's thesis in Marine Technology
Supervisor: Kjell Larsen and Sverre Haver
June 2019

Norwegian University of Science and Technology
Faculty of Engineering
Department of Marine Technology

NTNU
Norwegian University of
Science and Technology

NTNU Trondheim
Norges teknisk-naturvitenskapelige universitet
Institutt for marin teknikk

MASTER THESIS SPRING 2019

for

Stud. tech. Anders Falsen Habostad

Assessment of design methods for structural response of floating wind turbines with focus on mooring line tension

Vurdering av metoder for lastvirkning for flytende vindturbiner – fokus på strekk i ankerliner

Background

Efficient structural design of floating wind turbines is important for assuring economic feasibility of large, floating wind parks. Present design methods and acceptable levels of structural response are therefore challenged. Important structural responses are mooring line tensions and bending moments in the tower. This thesis shall focus on the tension in the mooring lines.

The purpose of the mooring system is to keep the floating wind turbine safely at a required position. It normally consists of three mooring lines of chain material. The moorings must be reliable enough to prevent any free drift where power cable rupture and collisions with adjacent structures are typical consequences.

Design of the mooring system against extreme loads (ULS design) is done by establishing characteristic mooring line tensions in a short-term storm with a 50year return period and applying a safety factor to verify the assumed line strength. A long-term analysis accounting for all inherent randomness should, in principle, be used. This requires, however, a large amount of numerical analyses and is not considered standard practice today.

The overall objective of this thesis is to increase the competence related to floating wind turbines and how improved design methods could optimize design of the mooring system.

Scope of Work

1) Review relevant literature and give an overview of state-of-art of concepts for floating wind turbines. Describe possible mooring systems for floating units in general and floating wind turbines in particular. Focus on station keeping principles and main hardware components. The operation of a floating wind turbine in the three different wind speed regimes shall be briefly described.

2) Describe the time-domain analysis methods for mooring systems and how ULS characteristic wind turbine motions and line tension can be estimated using a short-term analysis method. The ULS and ALS design limit states for mooring systems with corresponding acceptance criteria outlined in rules and regulations (DNVGL-ST-0119) shall be described.

3) Present and discuss how the all sea states method and the random storms method can be

formulated for the given problem and demonstrate how q-probability mooring line tension can be estimated by the different approaches.

4) Further develop and improve the SIMO/RIFLEX model of a floating wind turbine in SIMA. Propose and plan how short term and long-term analyses can be performed and results extracted.

5) Design a mooring system for the selected floating wind turbine concept operating in a the Hywind Scotland area using a short-term approach according to DNVGL-ST-0119. Neglect fatigue limit state design.

6) Perform a long-term analysis according to the random storm method for the mooring line tension. Estimate tension with 50year and 500year return periods and compare with characteristic values estimated in 5). If time allows, a model that can be used for assessment of the tower bending moment shall be proposed.

7) Conclusions and recommendations for further work.

General information

All necessary input data for the simulation case is assumed to be provided by Equinor.

The work scope may prove to be larger than initially anticipated. Subject to approval from the supervisor, topics may be reduced in extent.
In the project, the candidate shall present his personal contribution to the resolution of problems within the scope of work.
Theories and conclusions should be based on mathematical derivations and/or logic reasoning identifying the various steps in the deduction.

The candidate should utilise the existing possibilities for obtaining relevant literature.

Report/Delivery
The thesis report should be organised in a rational manner to give a clear exposition of results, assessments, and conclusions. The text should be brief and to the point, with a clear language. Telegraphic language should be avoided.

The report shall be written in English and edited as a research report including literature survey, description of relevant mathematical models together with numerical simulation results, discussion, conclusions and proposal for further work. List of symbols and acronyms, references and (optional) appendices shall also be included. All figures, tables and equations shall be numerated.

The original contribution of the candidate and material taken from other sources shall be clearly defined. Work from other sources shall be properly referenced using an acknowledged referencing system.

The report shall be submitted in Inspera, as specified by the department of Marine Technology.
In addition, an electronic copy (pdf) to be sent to the supervisors.

Ownership
NTNU has according to the present rules the ownership of the project results. Any use of the project results has to be approved by NTNU (or external partner when this applies). The department has the right to use the results as if the work was carried out by a NTNU employee, if nothing else has been agreed in advance.

Thesis supervisor**:**
Prof. II Kjell Larsen, NTNU/Equinor
Prof. Sverre Haver, NTNU/UIS

Deadline: June 11th, 2019

Trondheim, January 29th, 2019

Kjell Larsen (sign.)

Anders Falsen Habostad (sign.)

Acknowledgement

I would like to express my gratitude to my supervisor Kjell Larsen for close follow-up of the project during the whole semester. Our weekly meetings have provided me with an increased insight in the hydrodynamic aspects of floating wind turbines and mooring system design. I would also like to thank my co-supervisor Sverre Haver- your knowledge and interest in extreme value statistics have proven very useful for my understanding of the field.

I wish to thank Carlos Eduardo Silva de Souza for always being available for assistance with SIMA when I have run into problems I have not been able to figure out myself.

I will also express my gratitude to Associate Professor Erin Bachynski for providing the first order wave load transfer functions for the CSC substructure. The discussions of characteristics of floating wind turbines have also been very useful.

Last, I would like to thank my fellow students at the Department of Marine Technology. You have been a great support in my academic development the last five years, but even more important; you have contributed to making my years at NTNU the best of my life.

Abstract

The overall objective of this thesis is to increase the competence related to floating wind turbines with special focus on design methods for the mooring system. The results from using a traditional mooring line design approach outlined in *DNVGL-ST-0119 Floating wind turbine structures* (2018) is compared with the results from a long term analysis using a peak-over-threshold (POT) method. The floating wind turbine structure under consideration is the DTU 10MW reference turbine supported by a CSC substructure first proposed by Wang (2014).

A large number of time domain simulations were needed in order to perform the long term POT analysis and a simplified model of the wind turbine was needed in order to reduce the computational time. Hence, the rotor blades and the blade pitch control system were not included in the simplified SIMA model used for the time domain simulations. Instead, the thrust force on the rotor blades was modelled using slender elements with specified wind coefficients or as constant forces, depending on the wind regime.

When using the traditional short-term approach outlined in *DNVGL-ST-0119 Floating wind turbine structures* (2018), metocean contour lines for the combination of wind speed and H_s corresponding to 50- and 500 year return periods were established. Simulations of sea states at several points along the contour lines were performed in order to identify the sea state resulting in the highest mooring line tension. It was found that the highest mooring line tension occurred for the sea state with largest significant wave height. This suggests that the mooring line tension of the floating wind turbine is more sensitive to wave loads than wind loads. In order to establish the design tension, 20 time domain simulations of this sea state were performed and a Gumbel distribution was fitted to the largest mooring line tension occurring in each of the simulations. The characteristic tension was taken as the most probable largest value found from the Gumbel distribution and the design tension was found by applying safety factors to the mean- and dynamic part of the characteristic tension.

In the Random Storm approach, the idea is to establish the long-term distribution for the largest mooring line tension in an arbitrary storm. First, a threshold of $H_s > 6m$ was used as criteria to select a storm sample. This resulted in a sample of 143 storms, each modelled as a sequence of stationary sea states referred to as storm steps. Time domain simulations

using 20 different random seeds for wind and waves for each storm step were performed in SIMA. Based on the results, the long-term distribution of the largest line response accounting for non-observed storms was obtained. This was done by first estimating the distribution of the largest response in a storm given the most probable largest response in the storm and then establishing the long term distribution of the most probable largest line response in an arbitrary storm.

By comparing the results of the traditional short term design approach to the results of the POT long term approach, it was found that the ULS design tension found using the traditional short term approach corresponds to an annual exceedance probability of less than 10^{-7}. This shows that in this case the traditional design approach provides conservative estimates for the design tension. However, long term analyses for several different wind turbine concepts in various locations should be performed in order to indicate if the safety factors outlined in *DNVGL-ST-0119 Floating wind turbine structures* (2018) can be reduced while maintaining the desired safety level.

Sammendrag

Det overordnede målet med denne oppgaven er å øke kompetansen knyttet til flytende vindturbiner med spesielt fokus på designmetoder for forankringssystemet. Resultatene fra å bruke en tradisjonell designmetode gitt i *DNVGL-ST-0119 Floating wind turbine structures* (2018) er sammenlignet med resultatene fra en langtidsanalyse ved bruk av terskelmetoden (POT-metoden). Den flytende vindturbinen under betraktning er DTU 10MW referanseturbin med en CSC-substruktur designet av Wang (2014).

Et stort antall tidsdomenesimuleringer var nødvendig for å utføre POT-analysen og det var derfor behov for en forenklet modell av vindturbinen for å redusere simuleringstiden. Derfor ble rotorbladene og kontrollsystemet for justering av vinkler på bladene ikke inkludert i den forenklede SIMA-modellen som ble brukt til tidsdomenesimuleringene. Istedenfor ble kraften på rotorbladene modellert enten ved hjelp av elementer med spesifiserte vindkoeffisienter eller som konstante krefter, avhengig av vindregimet.

Ved bruk av den tradisjonelle metoden gitt i *DNVGL-ST-0119 Floating wind turbine structures* (2018), ble det først etablert konturlinjer for kombinasjoner av vindhastighet og signifikant bølgehøyde med retureperiode 50 og 500 år. Flere punkter langs konturlinjene ble simulert for å identifisere den sjøtilstanden som resulterte i det høyeste strekket i ankerlinene. Det ble funnet at sjøtilstanden med størst signifikant bølgehøyde resulterte i det høyeste strekket i ankerlinene. Dette indikerer at forankringssystemet til den flytende vindturbinen er mer sensitivt for bølgelaster enn vindlaster. For å finne designspenningen, ble det gjennomført 20 tidsdomenesimuleringer av denne sjøtilstanden, og en Gumbel-fordeling ble tilpasset til det største ankerlinestrekket i hver av simuleringene. Det karakteristiske linestrekket er gitt som det mest sannsynlig største ankerlinestrekket i Gumbel-fordelingen, og design-linestrekket ble funnet ved å anvende sikkerhetsfaktorer på middelverdeien og den dynamiske delen av det karakteristiske linestrekket.

I terskelmetoden er ideen å etablere en langtidsfordeling for det største strekket i ankerlinene i en vilkårlig storm. Første ble terskelen $H_s > 6m$ brukt som kriterie for å etablere et utvalg av stormer. Dette resulterte i et utvalg bestående av 143 stormer, der hver storm ble modellert som en sekvens av stasjonære sjøtilstander (stormtrinn). Hvert stormtrinn ble simulert 20 ganger med ulike frøtall for bølger og vind. Basert på resultatene ble langtids-

fordeling for det største linestrekket etablert. Dette ble gjort ved først å estimere fordelingen av det største linestrekket i en storm gitt det mest sannsynlige største linestrekket i stormen, og deretter etablere en langtidsfordeling for mest sannsynlige største linestrekket i en tilfeldig storm.

Ved å sammenligne resultatene funnet ved bruk av den tradisjonelle korttidsmetoden og resultatene av POT-analysene, ble det funnet at designlinestrekket i ULS etablert ved bruk av en tradisjonelle metoden har en årlig overskridelsessannsynlighet på mindre enn 10^{-7}. Dette indikerer at i dette tilfellet gir den tradisjonelle designmetoden konservative estimater for designlinestrekket. Langtidsanalyser for flere forskjellige vindturbinekonsepter på ulike lokasjoner bør imidlertid utføres for å indikere om sikkerhetsfaktorene gitt i *DNVGL-ST-0119 Floating wind turbine structures* (2018) kan reduseres uten å redusere sikkerhetsnivået.

Contents

List of Figures

List of Tables

Abbreviations

ALS	Accidental limit state
cdf	Cumulative distribution function
FLS	Fatigue limit state
FWT	Floating wind turbine
HF	High frequency
IFORM	Inverse first-order reliability method
JONSWAP	Joint North Sea wave project
LF	Low frequency
MPM	Most probable maximum
O&G	Oil and gas
pdf	Probability density function
POT	Peak-over-threshold
ULS	Ultimate limit state
WF	Wave frequency

Nomenclature

$\boldsymbol{A(\omega)}$	frequency dependent added mass matrix
a	Generalized Pareto shape parameter
$\boldsymbol{C(\omega)}$	frequency dependent potential damping matrix
C_D	drag coefficient
C_{wind}	quadratic wind coefficient
$\boldsymbol{D_l}$	linear frequency independent damping matrix
$\boldsymbol{D_q}$	quadratic damping matrix
E	modulus of elasticity
F_G	gravitational force
$F_{Hs\|U_{10}}(h\|u)$	conditional distribution of H_s given U_{10}
F_{thrust}	thrust force
$F_{X_m\|k}(x\|k)$	cdf of the maximum 3-hour response in step m of storm k
$F_Y(y)$	long term distribution of largest line tension
$F_{Y\|\tilde{y}}(y\|\tilde{y})$	conditional distribution of largest line tension given the most probable largest line tension
$F_{Y_k\|k}(Y\|k)$	cdf of the extreme value of storm k
H_s	significant wave height
$H(\omega)$	transfer function
$\boldsymbol{h}(t-\tau)$	retardation function

I_x	moment of inertia about the x-axis
I_y	moment of inertia about the y-axis
I_z	moment of inertia about the z-axis
$\boldsymbol{K(r)}$	stiffness matrix
k_E	elastic stiffness of mooring system
k_G	geometric stiffness of mooring system
k_s	current constant for storm surge current
k_T	total stiffness of mooring system
k_w	current constant for wind generated current
l	total mooring line length
$\boldsymbol{M}$	mass matrix
n_{1y}	expected number of storms in a year
q_{1y}	annual probability of exceedance
$\boldsymbol{q_{exc}}(t, \boldsymbol{r}, \ddot{\boldsymbol{r}})$	excitation loads
S_C	characteristic capacity
S_{mbs}	minimum breaking strength
T_c	characteristic tension
$T_{c,dyn}$	characteristic dynamic tension
$T_{c,mean}$	characteristic mean tension
T_d	design tension
$T_{d,ALS}$	ALS design tension
$T_{d,ULS}$	ULS design tenion
T_H	horizontal line tension
T_P	spectral peak period
U_{10}	wind speed 10m above the sea surface

u_f	utilization factor
$\overline{V}$	mean current velocity
$v_{cur,surge}$	storm surge current speed
$v_{cur,tide}$	tidal current speed
$v_{cur,wind}$	wind generated current speed
w	mooring line weight in water
$\tilde{y}$	most probable largest line tension
z_1	variable in the Gaussian space
z_2	variable in the Gaussian space
z_{hub}	distance from sea surface to the rotor hub (119m)
α_u	Weibull shape factor for the marginal distribution of wind speed
$\beta_{m,k}$	Gumbel scale parameter in the distribution of largest line tension in step m of storm k
β_u	Weibull shape parameter for the marginal distribution of wind speed
$\beta_{Hs\|U_{10}}$	Gumbel scale parameter for the conditional distribution of H_s given wind speed
ρ_{water}	water density
ζ	wave component
Ω	heading angle for environmental loads
λ	Weibull location parameter
γ_{dyn}	load factor for the dynamic tension
$\gamma_{Hs\|U_{10}}$	Gumbel parameter for the conditional distribution of H_s given wind speed
γ_{mean}	load factor for the mean tension
$\gamma_{m,k}$	Gumbel parameter in the distribution of largest line tension in step m of storm k

Chapter 1

Introduction

1.1 Background

Offshore wind has been a business area in rapid development the last years and the prices for power produced by offshore wind turbines has decreased more than 60% since 2011, Orsted (2018). Until now, the installed capacity has mainly consisted of bottom-fixed turbines in shallow water. When installed in 2017 the Hywind Scotland Pilot Park became the world's first floating wind farm and several stakeholders predict floating wind to be the next wave within renewable energy, Equinor (2018). However, the price of floating wind turbines is still significantly higher than for bottom-fixed. Hence, an important research topic is to identify areas of cost reduction for the production, installation and operation of floating wind turbines.

An important part of a floating wind turbine is the mooring system. It has to be designed so it limits drift of the floating turbine to be within the offset criteria. If the offset criteria is violated it will in most cases result in a ruptured power cable which is expensive to replace. At the same time, it is rarely desirable to be too conservative in the design of the mooring lines as this can lead to increased costs. Hence, it is important that the design procedure ensures that the desired safety level is obtained without oversizing the mooring system.

Today, the design of mooring systems against extreme loads (ULS) is done by establishing the characteristic mooring line tension in a short term sea state (normally 3 hours) corresponding to a 50 year return period and applying a safety factor to find the required

line strength. However, a long term analysis accounting for all inherent randomness should in principle be used. This requires a large number of numerical analyses and is not considered normal practice today.

For the oil and gas industry, the safety factors applied to find the required line strength from the short term sea state analyses have been investigated thoroughly through many years. Hence, they are assumed to be tuned properly to account for the fact that the short term analysis do not account for all inherent randomness. However, for floating wind turbines, more studies comparing the short term sea state design methodology to a long term approach are required to indicate the actual safety level obtained using the standard short term approach.

1.2 Objective

The main objective of this thesis is to increase the competence related to floating wind turbines, and investigate how improved design methods can optimize mooring system design. The latter will be done by comparing the results of a traditional design approach outlined in *DNVGL-ST-0119 Floating wind turbine structures* (2018) and the results from a long term analysis using a peak-over-threshold approach.

1.3 Thesis Outline

The report documents work done both in the project thesis and the Master's thesis. Hence, Chapter 1-9 contain contributions from the project thesis work. However, these chapters also contain many new elements added in the Master's project.

Chapter 2 gives an introduction to a few different concepts of floating wind turbines.

Chapter 3 describes catenary and taut mooring systems and some key characteristics of these types of mooring systems are discussed. In addition, some anchor types are presented.

Chapter 4 covers how the equation of motion can be used to calculate floater motions. In

addition, the excitation forces are described and it is briefly discussed how they can be calculated. This chapter presents the theory behind the analyses performed in SIMA.

Chapter 5 describes the existing rules for mooring system design given in *DNVGL-ST-0119 Floating wind turbine structures* (2018). Special focus is given to how a short-term statistical approach can be used to obtain the design tension in the mooring lines.

Chapter 6 focuses on how long term statistical approaches can be used to establish ULS response characteristics. The all sea state approach and the random storm approach are described.

Chapter 7 is devoted to the metocaen data given for the Hywind Scotland location. Environmental characteristics corresponding to 50- and 500 year return periods are calculated using a POT approach. A comparison between a Weibull fitted distribution and a Generalized Pareto distribution is made.

Chapter 8 describes the simplified SIMA model. While Chapter 4 focuses on the theory behind time domain analysis in SIMA, Chapter 8 describes how the SIMA model was implemented.

Chapter 9 is dedicated to documentation of how the aerodynamic loads were modelled in the simplified SIMA model.

Chapter 10 gives a brief description of how decay tests where performed in SIMA and the natural periods in heave and pitch are compared to those of the original model proposed by Wang (2014). In addition, pullout tests are included in order to document the mooring system stiffness.

In Chapter 11 it is shown how the traditional short-term approach outlined in *DNVGL-ST-0119 Floating wind turbine structures* (2018) was used to to find the mooring line design tension.

Chapter 12 describes how a peak-over-threshold (POT) approach was used to establish the long-term distribution of the largest mooring lines tension in an arbitrary storm.

Chapter 13 compares the results of the traditional short-term design approach to the long-term distribution of the largest mooring line tension found using the POT approach.

Chapter 14 briefly explains how the simplified SIMA model can be used for long term analyses of tower bending moments.

Chapter 15 gives some concluding remarks and suggestions for further work.

Chapter 2

Floating wind turbine concepts

There are several different floater concepts which are developed to support wind turbines. They will not all be accounted for here, but some of the concepts will be briefly described in order to provide some background of the development of different concepts.

2.1 Hywind

Hywind is a floating spar substructure developed by Equinor (former Statoil). The first Hywind Demo was equipped with a 2.3 MW turbine and was installed outside Karmøy in Norway in 2009. After successfully testing the concept for eight years, the world's first floating wind farm, Hywind Scotland, was installed in 2017. The park consists of five floating wind turbines each with a capacity of 6 MW.

The Hywind Scotland substructure consists of a steel cylinder with iron ore used for fixed ballast. The unit has a total displacement of approximately 12000 tonnes and a draft of around 90 meters. Due to the large draft, the assembly of substructure and tower cannot be performed quayside. For the Hywind Scotland project, the substructure and the tower with rotor was mated outside Stord in Norway and then towed to the final destination outside Scotland.

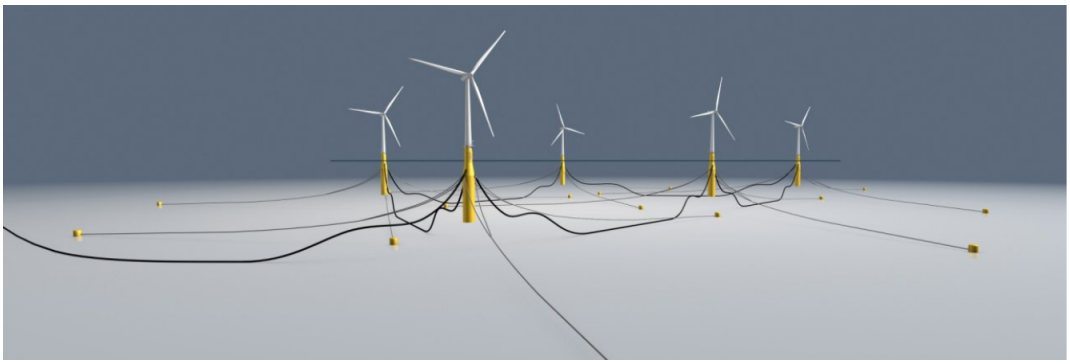

Figure 2.1: Hywind Scotland Pilot Park configuration, Equinor (2018).

The mooring system used for Hywind Scotland is a 3-line catenary system. The anchors used are suction anchors.

2.2 Windfloat

Windfloat is a floating foundation developed by Principle Power. The foundation consists of three columns connected by braces. Heave plates are connected to the base of each column in order to increase the added mass and viscous damping of the structure. The tower is connected to one of the columns, and is hence not located in the centre of the structure. The draft of the unit is typically between 10 and 20 metres depending on the size of the turbine. This is low compared to for example a spar configuration like Hywind and allows the Windfloat structure to be assembled onshore or quayside before being towed to its final location, PrinciplePower (2018).

The Windfloat foundation has a closed-loop active ballast system which distributes the ballast water between tanks in the three columns. This allows the structure to compensate for varying pitch moment due to variable wind thrust.

The first Windfloat demo was installed outside the coast of Portugal in 2011. After five years deployment, the floater was disconnected from the mooring lines and towed back to shore. There are still no full-scale floating wind farms using the Windfloat foundation, but the 1st of November 2018, Principle Power announced that Kincardine Offshore Wind Farm will use the Windfloat foundation for their 50MW build-out offshore Kincardineshire, Scotland.

Figure 2.2: Windfloat demo, PrinciplePower (2018)

2.3 CSC semi

The CSC is a semisubmersible concept originally developed by Cheny Luan at NTNU. There exists several iterations of the design, also including wave enrgy converters attached to the hull, Luan (2014). In contrast to the Windfloat concept, the CSC semi has the tower located in the center of the structure and does not have an active ballast system.

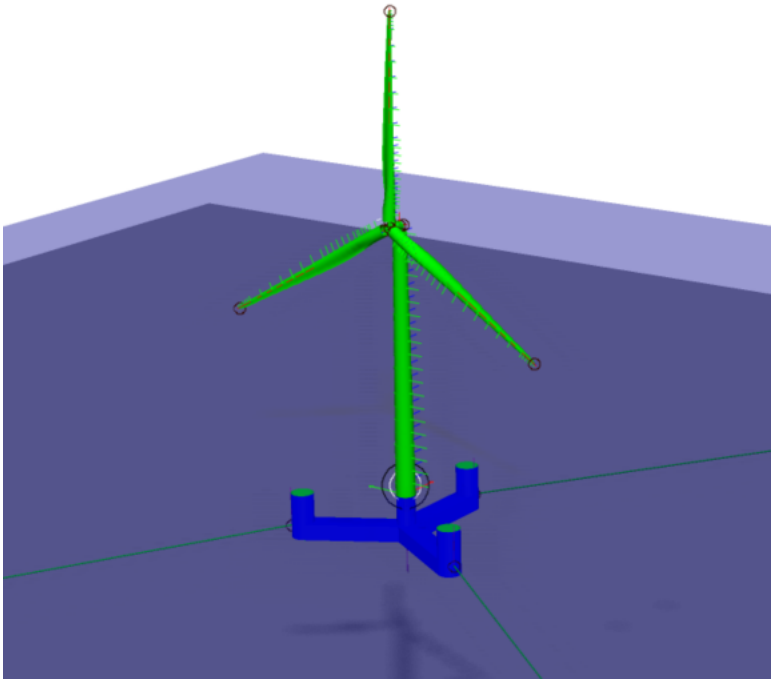

Figure 2.3: SIMA model of the CSC concept for support of the DTU 10MW reference turbine.

For this thesis, the CSC semi model developed by Wang (2014) to support the DTU 10MW reference turbine will be used. The model will be described more thoroughly in Chapter 8.

Chapter 3

Mooring systems

In order to discuss mooring line tension it is crucial to have a broad theoretical understanding of the mooring system characteristics. Hence, different important aspects of mooring systems for floating units in general and floating wind turbines in particular will be discussed in the following sections.

The main functional requirement of a mooring system is to keep the offset of a floater within an acceptable limit. This limit can be governed by several factors. For an offshore production platform it is often the risers that dictates the maximum allowable offset. For a floating wind turbine it is mainly the power cable characteristics which determines the maximum allowable offset. In addition to offset limitations, lifetime before replacement, installability and positioning ability are other important functional requirements for a mooring system, Chakrabarti (2005).

In general, there are two main types of mooring systems; catenary and taut. The focus in this thesis is on catenary systems. Hence, taut systems will only be briefly described.

3.1 Catenary system

A traditional catenary system consists of chain, in some cases in combination with wire. This is the most common type of mooring system and is applied to a broad range of different ships and offshore structures. Hywind Scotland uses a 3-line catenary mooring system. Advan-

tages of a catenary system is that it is well tested and the characteristics of the mooring lines (chain/wire) are well documented. In addition, the system is relatively simple and performs well in a relatively broad range of water depths. However, issues might arise at large water depths where the weight of the mooring lines becomes too large.

Figure 3.1 shows a typical geometry of a catenary mooring line. X_B is the distance between the anchor and the touchdown point of the line, T is the effective tension and T_H is the horizontal force in the mooring line. The restoring forces comes primarily from geometric stiffness and elastic stiffness. The geometric stiffness can be simply explained by the fact that when the floater gets an offset in the horizontal plane, a larger part of the the mooring line will be lifted from the seabed as shown by the dotted line in Figure 3.2. At the same time, the angle between the mooring line and the horizontal plane at the connection with the vessel will decrease. These features combined result in a restoring force in the horizontal plane. The elastic stiffness is governed by the elastic properties of the mooring line material and the line length.

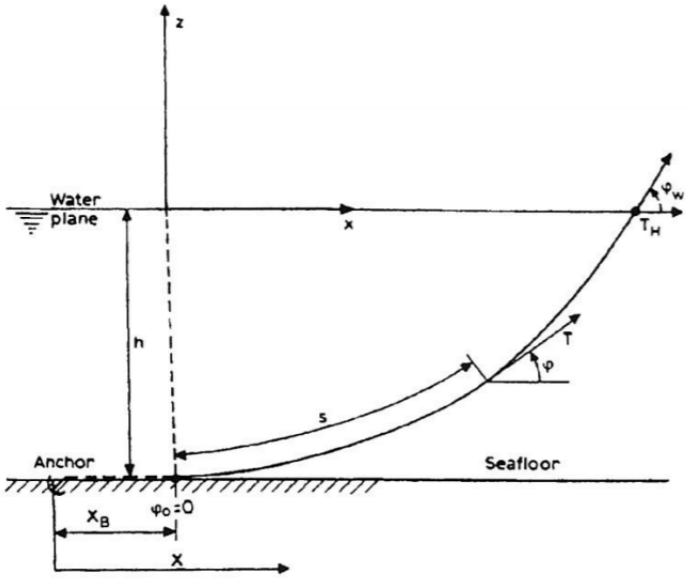

Figure 3.1: A typical catenary shape of a mooring line as illustrated in Chakrabarti (2005).

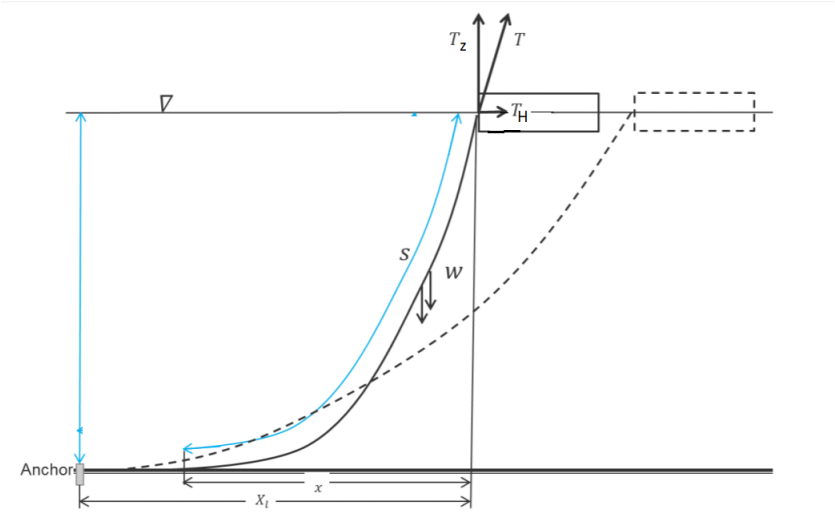

Figure 3.2: Geometry of mooring line for different offsets. Modified version of figure provided by Larsen (2015*b*).

A simple model to express the resulting total stiffness from geometric and elastic stiffness can be obtained by considering the mooring line as a series of two springs where one of the springs has stiffness equal the elastic stiffness and the other has stiffness equal to the geometric stiffness. The resulting total stiffness, k_T , of the mooring line can then be found from equation 3.1.

$$\frac{1}{k_T} = \frac{1}{k_G} + \frac{1}{k_E} \tag{3.1}$$

or explicitly written:

$$k_T = \frac{k_G \cdot k_E}{k_G + k_E} \tag{3.2}$$

where k_G is the geometric stiffness and k_E is the elastic stiffness. The force F applied resulting in an offset r in the axial direction of the mooring line can then be expressed as

$$F = k_T \cdot r \tag{3.3}$$

The behaviour of a mooring line can be described by a set of catenary equations. The cate-

nary equations are derived by considering static equilibrium of a mooring line and hence dynamics are not taken into account. Other important assumptions are that the seabed is considered flat and the bending stiffness in the mooring lines are neglected. The last will be a good assumption for chain and also for wire without too large curvature, Chakrabarti (2005).

Figure 3.3 shows a line element exposed to hydrodynamic forces in both normal (transverse) and tangential (in-line) direction. These forces are denoted D and F respectively.

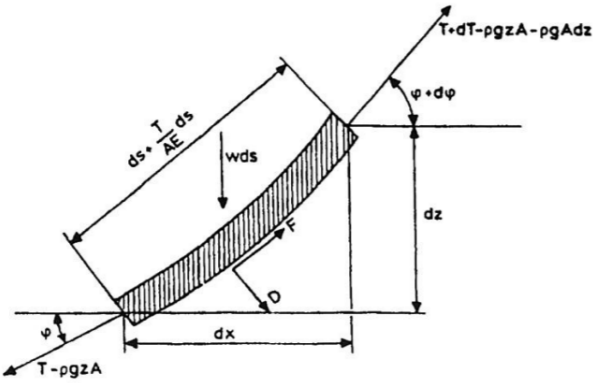

Figure 3.3: Line element from Faltinsen (1990).

According to Faltinsen (1990), the static equilibrium of the mooring line segment in both tangential and axial direction direction can be then be expressed as:

$$dT - \rho g A dz = \left[w \cdot sin(\varphi) - F(1 + \frac{T}{EA}) \right] \cdot ds \tag{3.4}$$

$$T \cdot d\varphi - \rho g A z d\varphi = \left[w cos \cdot \varphi + D(1 + \frac{T}{EA}) \right] ds \tag{3.5}$$

where T is effective line tension, w is the weight in water of the mooring line per unit length, A is the cross-sectional area of the mooring line and E is the modulus of elasticity, Faltinsen (1990).

In order to solve these equations explicitly, the hydrodynamic forces on the mooring lines are neglected. For conditions which do not involve extreme tensions in the lines it is also considered an OK approximation to neglect the elasticity of the mooring line. This results

in a set of inelastic catenary equations. These will not all be included here, references are made to Faltinsen (1990). However, the equation for the anchor diameter will be used to get an initial estimate for the anchor positions when tuning the mooring system in the SIMA-model and is hence included:

$$X_l = l + \frac{T_H}{w} \cdot cosh^{-1}\Big(1 + \frac{wh}{T_H}\Big) - \sqrt{h \cdot \Big(h + \frac{2T_H}{w}\Big)} \tag{3.6}$$

where l is the total line length, T_H is the horizontal line tension, w is the weight in water for the mooring line and h is the total water depth. This equation is important as it provides the line characteristics in terms of relation between the anchor radius, mooring line length and the horizontal tension in the line.

3.1.1 Horizontal system stiffness from catenary mooring lines

As mentioned in the previous section, the mooring lines introduces horizontal stiffness for the floater. The stiffness will be a function of the horizontal offset of the unit. For a simplified system consisting of two mooring lines with orientation in the opposite direction along the x-axis, the system restoring stiffness from the mooring system as a function of the offset is shown in Figure 3.4. As seen from the illustration, the system horizontal stiffness from mooring lines is non-linear.

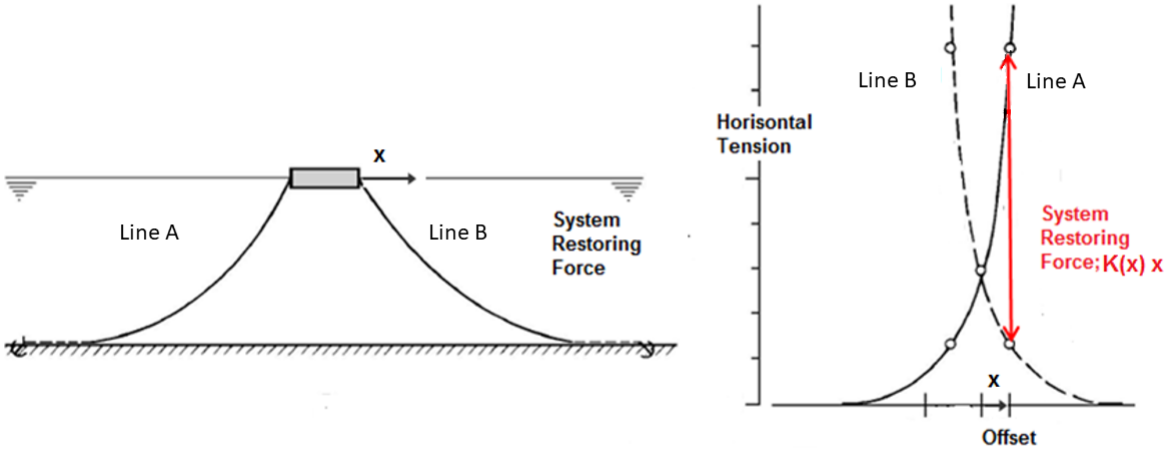

Figure 3.4: System horizontal stiffness from mooring lines. Modified version of figure from Larsen (2015*a*).

3.2 Taut system

In a taut mooring system, the mooring lines usually consists of synthetic fibre rope in a configuration as shown in Figure 3.5. The ropes usually have close to zero weight in water and the restoring forces of the mooring system comes primarily from elastic stiffness in the lines. Hence, the anchors in a taut mooring system needs to sustain significant vertical loads.

A taut mooring system consisting of synthetic fibre rope have several advantages compared to a traditional catenary system. First of all, the light weight reduces the vertical loading from mooring lines on the floating structure. Hence, taut mooring systems are often preferred for units operating in deep and ultra-deep waters. In addition, the mooring lines will have less footprint on the seabed than catenary lines considering the fact that the only contact for most taut systems is at the anchor point.

At the same time, there are also some disadvantages using a taut system compared to a

catenary. First of all, the stiffness of the mooring line is approximately inversely proportional to the length of the mooring line. That means that a taut mooring systems often require long mooring lines also in shallow and moderate water depths. Furthermore, the fibre rope has a more complex behaviour which is in general more dependent on historic loads than chain/wire. With respect to fatigue, the fibre rope in general performs worse than chain/wire, especially if a line goes into slack as this can result in local buckling of fibres, Chakrabarti (2005).

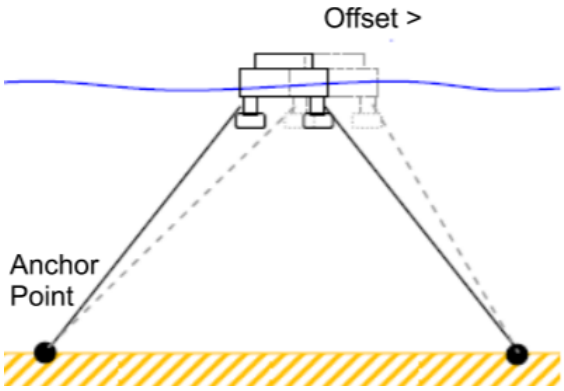

Figure 3.5: Typical taut mooring configuration as presented in Flory (2016).

3.3 Anchors

The anchors constitutes an important part of the mooring system. Hence, some different anchor alternatives are briefly described in the following section. Not all anchor types are included and for a more thorough discussion of anchor characteristics it is referred to Vryhof (2010).

Dead weight anchors

Dead weight anchors simply consists of a large weight, often in concrete or steel. The horizontal holding capacity is generated by the friction between the seabed and the weight due to the large mass. The configuration is simple, but for structures exposed to high loads, the weight of the anchor needs to be very large which makes it costly to install. Hence, the dead weight anchors are primarily used for structures exposed to smaller loads.

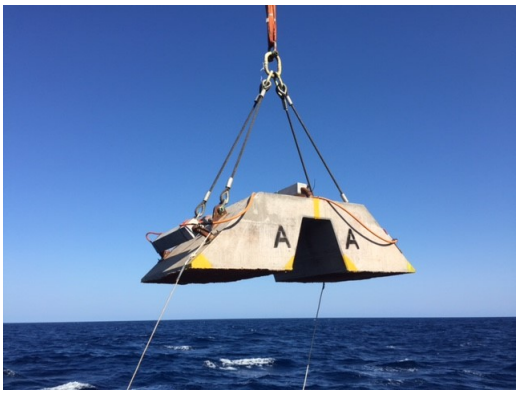

Figure 3.6: Dead weight anchor, Subcon (2018).

Drag embedment acnhor

Drag embedment anchors are installed by pulling the anchor horizontally. Due to the geometry of the anchor, this results in the anchor penetrating the seabed to a desireable depth. The horizontal holding force of the anchor is due to the soil in front of the anchor. In general, the anchor has good resistance to horizontal loads, but has a poorer resistance to vertical loads. Hence, the anchor type is rarely used in taut mooring systems. For catenary systems on the other hand, drag embedment anchors is one of the most common types of anchors used.

Figure 3.7: Drag anchor, Vryhof (2010).

Vertical load anchor

Vertical load anchors are installed similarily as drag embedment anchors. However, they are normally embedded much deeper into the soil than a typical drag embedment anchor. After embedment, the anchor configuration changes from installation mode to vertical loading mode. This involves changing the angle of the pulling point to the fluke which allows the anchor to take large vertical loads. Vertical load anchors can hence be used for taut mooring systems.

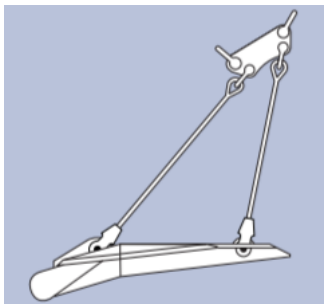

Figure 3.8: Vertical load anchor, Vryhof (2010).

Pile anchors

Pile anchors are hollow steel pipes which are normally installed by using piling hammers or vibrators to drive the piles deep into the seabed. The holding capacity of the pile anchors comes from friction between the pile and the seabed and they are in general capable of resisting both horizontal and vertical loads.

Suction Anchors

Suction anchors are hollow steel pipes with large diameter which are closed on the top. The suction anchors are installed by using a pump creating a lower pressure inside the closed pipe than on the outside. This results in the anchor being sucked into the seabed. The suction anchor can withstand both horizontal and vertical loads. For Hywind Scotland Pilot Park, suction anchors were used.

Figure 3.9: Suction anchors used for Hywind Scotland Pilot Park, Offshore Wind (2018).

3.4 General comparison of mooring systems for floating wind turbines and O&G installations

The experience from mooring floating oil and gas platforms is of course applicable also for offshore wind turbines. Still, there are some characteristics which are unique for floating wind turbines compared to oil and gas installations. This results in differences in the mooring system design.

First of all, the consequences of too large offsets are in general much higher for an offshore O&G installation than for floating wind turbines. If the mooring system of for instance a production platform fails to limit the offset to the acceptable limit, this might lead to an environmental disaster due to broken risers. In comparison, the worst consequence of too large offsets for a floating wind turbine will in most cases be a broken power cable. The risk of collision with adjacent units is present, but is considered low due to the fact that there is often approximately 1km distance downwind between each unit in order to avoid that adjacent wind turbines disturb each others incoming wind field. The safety requirements are also in general higher for oil and gas installations due to the fact that they are manned in contrast to a FWT.

A floating O&G installation will in most cases have between 8 and 20 mooring lines organized in 3-5 groups. Due to the large number of units installed in a FWT-park, it is in general beneficial to limit the number of mooring lines, and thereby the number of marine installing operations to a minimum. Hence, most floating wind turbine concepts only have three mooring lines. This is the case for both Hywind Scotland, the WindFloat test turbine and the CSC-concept. While reducing the number of installation operations, only having three mooring lines will at the same time result in very large offsets for the FWT in the case of failure in one line.

Another important feature of a typical FWT is high mean weather loading compared to traditional O&G installations. An important contribution to the this comes from the rotor thrust. Most floating wind turbines have rated wind speeds around 10-12 m/s. The thrust on the rotor is largest around these wind speeds leading to high wind loads on the turbine for relatively low wind speeds resulting in large mean offsets compared to O&G installations. In addition to the large mean offset due to wind loads, the wave frequency RAOs

in surge are considerably higher for most FWT concepts compared to traditional O&G installations, Larsen (2015*a*). This results in large wave frequency motions compared to most O&G installations. The fact that only 3 mooring lines are used also makes the mean line tension considerably higher for a FWT than for an O&G installation exposed to the same load. The combinations of high mean tensions in the mooring lines and large wave frequency motions in surge, results in large mean tension, and also large variations in tension in the mooring lines. Hence, the mooring system is very exposed to fatigue damage. For the mooring system of the units in Hywind Scotland Pilot Park, FLS was the governing design criteria.

For FWTs with a spar substructure, like for instance Hywind Scotland, the low diameter can result in too low yaw stiffness if the mooring lines are attached directly to the substructure. Hence, bridles are used as pictured in Figure 3.10.

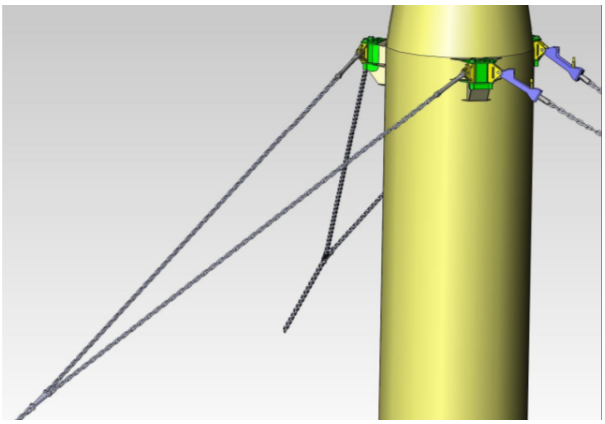

Figure 3.10: Bridles used in Hywind Scotland, Statoil (2014).

For the CSC substructure, the mooring points are far enough away from the vertical centerline of the structure to provide sufficient yaw stiffness. Hence, bridles are not required.

Chapter 4

Calculating floater motions using the equation of motions

In order to analyze the response in the mooring lines in different environmental conditions, a large number of time domain analyses will be performed in SIMA. Both the model of the floating wind turbine and the environment have to represent the real case in a sufficient manner in order to obtain good quality results of the simulations. Hence, it is crucial to understand the underlying theory of the SIMA modelling. This will be accounted for in the following subsections. How this theory is used in practice to model the floating wind turbine is described in Chapter 8.

4.1 Equation of motions

The motions of the floating wind turbine are governing for the loads experienced by the mooring lines. In general, the equation of motions for a floating vessel in six degrees of freedom can be written as

$$(\boldsymbol{M} + \boldsymbol{A}(\boldsymbol{\omega})) \cdot \ddot{\boldsymbol{r}} + \boldsymbol{C}(\boldsymbol{\omega}) \cdot \dot{\boldsymbol{r}} + \boldsymbol{D_l} \cdot \dot{\boldsymbol{r}} + \boldsymbol{D_q} \cdot \dot{\boldsymbol{r}}|\dot{\boldsymbol{r}}| + \boldsymbol{K}(\boldsymbol{r}) \cdot \boldsymbol{r} = \boldsymbol{q_{exc}}(t, \boldsymbol{r}, \dot{\boldsymbol{r}}) \tag{4.1}$$

where $\boldsymbol{M}$ is the mass matrix, $\boldsymbol{A}(\boldsymbol{\omega})$ is the frequency dependent added mass matrix, $\boldsymbol{C}(\boldsymbol{\omega})$ is the linear frequency dependent damping matrix, $\boldsymbol{D_l}$ is the frequency independent linear damping matrix, $\boldsymbol{D_q}$ is the quadratic damping matrix, $\boldsymbol{K(r)}$ is the stiffness matrix and $\boldsymbol{q_{exc}}(t, \boldsymbol{r}, \dot{\boldsymbol{r}})$ is the excitation load vector. The terms in equation 4.1 will be discussed in the following sections, but it can already be noted that equation 4.1 has both frequency dependent and time dependent terms. In order to write the equation solely in the time domain, frequency dependent added mass, $\boldsymbol{A}(\boldsymbol{\omega})$) and the frequency dependent damping, $\boldsymbol{C}(\boldsymbol{\omega})$, can be included using a convolution integral, resulting in the following equation of motion, SimoManual (2017):

$$(\boldsymbol{M} + \boldsymbol{A_\infty})\ddot{\boldsymbol{r}} + \boldsymbol{D_l} \cdot \dot{\boldsymbol{r}} + \boldsymbol{D_q} \cdot \dot{\boldsymbol{r}}|\dot{\boldsymbol{r}}| + \boldsymbol{K}(\boldsymbol{r}) \cdot \boldsymbol{r} + \int_{-\infty}^{\infty} \boldsymbol{h}(t-\tau)\dot{\boldsymbol{r}}(\tau)d\tau = \boldsymbol{q_{exc}}(t, \boldsymbol{r}, \dot{\boldsymbol{r}}) \quad (4.2)$$

where $\boldsymbol{h}(t-\tau)$ is the retardation function. $\boldsymbol{r}$ is a function of time. Both equation 4.2 and the retardation function will be further described in section 4.4.

For simplicity, the excitation loads and the equation of motions are considered only in the surge degree of freedom in the following subsections unless stated otherwise.

4.2 Excitation loads

The excitation loads on the floating wind turbine will consist of contributions from wind, waves and current.

4.2.1 Wind loads

Since the wind loads are so important for floating wind turbines, Chapter 9 is dedicated to the modelling of aerodynamic loads. Hence, details around aerodynamic modelling will not be presented here. Instead, a few important aspects of wind loads will be briefly accounted for.

The wind forces acting on the floating wind turbine can be divided into two main contributions. First of all is the thrust on the turbine blades which is governed by the rotor

blade pitch. The thrust force on the DTU 10MW reference turbine as a function of wind speed in hub height (119m above the sea surface) is shown in Figure 4.1. The wind turbine is operative for wind speeds in the range between 4 m/s and 25 m/s. For wind speeds above 25 m/s, the rotor is parked, power production is shut down and the rotor blades are feathered so they will have as small aerodynamic loads as possible.

As seen in Figure 4.1, the thrust force increases with increasing wind speed up to 11 m/s. For wind speeds higher than the rated wind speed, which for the DTU 10MW reference turbine is 11.4 m/s, the blade pitch system is activated and the rotor blades are pitched so the thrust force decreases.

For wind speeds close to the rated wind speed, the thrust force on the turbine blades will dominate the total wind loads on the structure. Further details regarding the thrust force and how it is modelled in the simplified SIMA model are presented in Chapter 9.

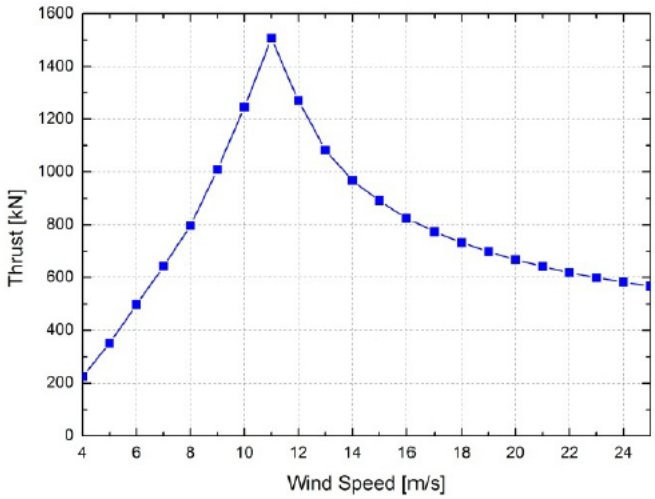

Figure 4.1: Thrust curve for the DTU 10 MW reference turbine given by Bak & Zahle (2013).

The second contribution comes from drag forces on tower, nacelle and substructure. When the turbine is parked, this is the dominating contribution to the total wind loads.

Current loads

The current velocity is assumed constant in time in each sea state. The current excitation force can then be written as

$$q_{cu}(t) = \frac{1}{2}\rho_{water} \cdot C_D \cdot A \cdot |\overline{V} - \dot{x}| \cdot (\overline{V} - \dot{x}) \tag{4.3}$$

where C_D is the drag coefficient of the substructure, A is the underwater area exposed to current, $\overline{V}$ is the constant current velocity and $\dot{x}$ is the floater LF velocity.

If it is assumed that $\overline{V}$ is significantly larger than $\dot{x}$, the current force can be approximated as

$$q_{cu}(t) \approx \frac{1}{2}\rho_{water} \cdot C_D \cdot A \cdot \overline{V}^2 - \rho_{water} \cdot C_D \cdot A \cdot \overline{V} \cdot \dot{x} \tag{4.4}$$

where the first term constitutes a constant force, while the last term is a LF damping force. The assumption of $\overline{V}$ being larger than $\dot{x}$ will not always hold. For floaters with large LF motions in areas with little current, the assumption could be questioned. However, in most cases, the periods of the low frequency motions will be so large that the LF velocity is smaller than the current speed. In the location studied in this thesis, the current velocities are high and the low frequency motions of the floater are small. Hence equation 4.4 will give a good representation of the current forces on the floater.

The current forces are included in the SIMA model by modelling the substructure as slender elements.

4.2.2 Linear wave excitation loads

The wave excitation loads are the forces and moments from incident waves acting on the unit when it is restrained from oscillating, Faltinsen (1990). There are two main contributions to the excitation loads; the Froude-Kriloff and diffraction loads. These contributions will not be explained further here, references are made to Faltinsen (1990). The most important is that the the Froude-Kriloff and diffraction loads obtained by first order potential theory are considered linear and their contributions can hence be superimposed in order to obtain the total linear wave excitation loads. In addition, the magnitude of these loads will be proportional to the wave amplitude ζ_a and the loads will act with the same frequency as the incident waves. Due to these characteristics, the relation between the wave amplitude and the load acting on the unit is often expressed in the frequency domain by a force transfer function:

$$q_{w,l}(\omega) = H(w) \cdot \zeta(\omega) \tag{4.5}$$

where $q_{w,l}(\omega)$ is the frequency dependent first order wave load, $H(w)$ is the complex force transfer function and $\zeta(\omega)$ is a wave component. In SIMA, the frequency dependent load transfer function with unit [N/m] is the input in the model, for instance obtained from a frequency domain solver like WADAM. In order to solve the equation of motion in the time domain, the linear frequency dependent wave load is rewritten using a convolution integral, SimoManual (2017):

$$q_{w,l}(t) = \frac{1}{2\pi} \int_{-\infty}^{\infty} h(\tau)\zeta(t-\tau)d\tau \tag{4.6}$$

where ζ is a time dependent wave component, h is the linear impulse response function given by the Fourier transform of the transfer function:

$$h(\tau) = \frac{1}{2\pi} \int_{-\infty}^{\infty} H(\omega)e^{i\omega\tau}d\omega \tag{4.7}$$

4.2.3 Higher order wave drift loads

In general, the higher order wave drift forces can be divided into two main contributions. The first contribution comes from the units ability to cause waves and can therefore be calculated using potential theory. The second contribution comes from viscous effects.

First, the contribution from the units ability to generate waves will be considered using second order theory. When using a first order theory to estimate linear wave forces, some important simplifications are made. First of all, the free-surface condition is satisfied on the mean free-surface and not the instantaneous free surface position. Similarly, the boundary condition of no flow through the solid body of the unit is satisfied on the mean body position and not the instantaneous position. By integrating to the instantaneous free surface and to the instantaneous wetted surface, higher order loads will be obtained. In addition, second order loads will occur by including the second order wave potential in the calculations.

The result is that in addition to the wave frequency loads, there will also be second or-

der mean drift loads and difference frequency (LF) wave drift forces. There will also be sum-frequency loads, but these are considered less relevant for a semi substructure as considered here.

The magnitude of the second order difference frequency wave loads are in general small compared to the wave frequency loads. However, due to the large periods of the wave drift forces, they will excite resonant motions in surge, sway and yaw. Due to little damping in these degrees of freedom, the resonant motions can be a significant part of the total response for large volume structures. However, the CSC substructure consists of very slender elements with little ability to generate waves. Hence, the second order wave drift loads will be negligible and are not included in the simplified model. It is therefore not considered relevant to give a thorough description of the second order wave loads here. Instead, a brief description of how SIMA in general deals with second order wave drift forces will be given in order to present a more complete picture.

The second-order transfer function for the difference-frequency force can be denoted $H^{(2-)}(\omega)$ and can be given as input in SIMA. In the same way as for the wave frequency linear transfer function, transfer functions can be obtained also for the second order loads through a diffraction analysis in for instance WADAM. It is here stated without further proof that by using the Newman method, the slow-varying second-order wave load can be expressed in the time domain as

$$q_{w,q}(t) = Re\left\{ \sum_m \sum_n \zeta_m \zeta_n H_{mn}^{(2-)}(\omega_m, \omega_n) e^{i(\omega_m - \omega_n)t} \right\} \tag{4.8}$$

where ζ_m and ζ_n are the complex Foruier components of the surface elevation with frequency ω_m and ω_n respectively. By time-averaging equation 4.8, the mean wave drift load is expressed by the following equation, SimoManual (2017).

$$\overline{q} = \frac{1}{2} Re\left\{ \sum_m \zeta_m \zeta_n^* H_{mn}^{2-} \right\} \tag{4.9}$$

For a further description of the theory behind the second order wave drift forces it is referred to SimoManual (2017).

While the second order wave drift loads will be negligible for the CSC semi, the viscous wave drift forces will on the other hand be more significant for CSC substructure and cause a mean drift load. This effect is captured by modelling the substructure of the FWT using slender elements in SIMA and integrating to the instantaneous wetted surface.

4.3 Mass, added mass, damping and stiffness

4.3.1 Mass and added mass

The first term of equation 4.1 consists of the mass forces which are proportional to the acceleration of the body. The mass matrix M consists of the structural mass for the translation degrees of freedom, and the moments of inertia in the rotational degrees of freedom. In SIMA, the mass matrix is specified as input. The mass matrix was established by considering the mass contributions from the different parts of the structure. This is further described in section 8.4.

The added mass can be viewed as the inertia added to the system due to acceleration of water particles around the structure. The added mass is frequency dependent and it is obtained by solving the radiation problem for the unit. In the radiation problem, the vessel is forced to oscillate in calm water and the resulting forces and moments are analyzed. This will not be further discussed here, references are made to Faltinsen (1990).

In SIMA the added mass is specified indirectly through the retardation function and by the added mass at $\omega = \infty$. This will be further discussed in section 4.4.

4.3.2 Damping

There are several different sources of damping in the system and these will be briefly described in the following sections.

Linear wave damping
The linear wave damping is found from solving the radiation problem. This type of damping

is related to the ability of the structure to generate waves and can be significant for damping of wave frequency motions. For the CSC substructure the linear damping will typically be relatively small due to the slender system. In SIMA the linear wave damping is indirectly specified through retardation function described in section 4.4. The linear wave damping is in general insignificant for damping of low-frequency motions considering the fact that these motions have much higher periods than the wave periods.

Viscous hydrodynamic damping

Viscous hydrodynamic damping will be important for damping of both wave frequency motions and low frequency motions. The viscous hydrodynamic damping is proportional with the square of the relative velocity between the water particles and the structure. Viscous hydrodynamic damping is incorporated in SIMA by defining slender elements for the pontoons and the columns of the substructure. Drag coefficients are defined for all slender elements and hence these will incorporate the relevant viscous forces.

Aerodynamic damping

Aerodynamic damping from turbine and tower can be important especially for damping of pitch motion. This will be further discussed in Chapter 9.

Wave drift damping

For large-volume structures, wave drift damping will be significant for damping of low frequency motions in surge. This type of damping will occur in the frequency ranges where the wave drift force coefficient increase for increasing frequencies. This causes the resistance in surge to increase when the vessel moves towards the waves due to the encounter frequency being higher than the wave frequency. Similarly, the low frequency excitation forces from the waves will decrease when the unit moves in the wave propagating direction. This will result in damping of the low frequency motions. Wave drift damping will not occur for the simplified CSC model due to the fact that wave drift loads are not included in the simplified SIMA model.

4.3.3 Stiffness

The stiffness in surge, sway and yaw comes from the restoring forces from the mooring system. For further description of the stiffness properties of the mooring system it is referred

to section 3. In heave, roll and pitch the restoring loads are primarily due to hydrostatic stiffness.

4.4 Solving the equation of motions in the time domain

There are two main approaches for solving the equation of motions- it can either be solved in the frequency domain or in the time domain. In this project, only time domain simulations will be performed and hence discussion of frequency domain solution is not included. For details of frequency domain solution of the equation of motions, reference is made to Newland (1993).

The main issue when solving the equation of motions in the time domain is that the equation has both frequency dependent and time dependent terms. In this thesis, this will be resolved by using a retardation function. For thorough description of how the retardation function is deduced, it is referred to the SIMO theory manual (SimoManual (2017)). It is here stated that the equation of motion can be rewritten to the following equation containing a convolution integral:

$$(\boldsymbol{M} + \boldsymbol{A_\infty})\ddot{\boldsymbol{r}}(t) + \boldsymbol{D_l} \cdot \dot{\boldsymbol{r}} + \boldsymbol{D_q} \cdot \dot{\boldsymbol{r}}|\dot{\boldsymbol{r}}| + \boldsymbol{K}(\boldsymbol{r}) \cdot \boldsymbol{r} + \int_{-\infty}^{\infty} \boldsymbol{h}(t-\tau)\dot{\boldsymbol{r}}(\tau)d\tau = \boldsymbol{q_{exc}}(t, \boldsymbol{r}, \dot{\boldsymbol{r}}) \quad (4.10)$$

where $\boldsymbol{h}(\tau)$ is the retardation function. The retardation function can be found from both the added mass term and the frequency dependent damping term in the equation of motion. Due to simpler numerics, it is often desirable to use the damping term and the retardation function is found by solving

$$\boldsymbol{h}(\tau) = \frac{2}{\pi} \int_0^{\infty} \boldsymbol{C}(w) cos(w\tau) d\omega \quad (4.11)$$

The result is inserted in equation 4.11 which can be solved using numerical integration in SIMO. There are several solution methods available in SIMO, in this project the Newmark-Beta procedure will be used. Further details on this method are not provided here, reference is made to SimoManual (2017).

4.4.1 Coupled approach to find mooring line tension

Solving the equation of motions in the time domain can be done either using a coupled or uncoupled approach. In the uncoupled analysis the equation of motion is first solved for the floating unit. Then, the unit motions are used as input when simulating the mooring tension. In a coupled approach, a complete model of the floating unit and the mooring system is used and the mooring line tension and body motions are simulated simultaneously.

In this thesis, a coupled time domain approach will be used to find mooring line tensions. This will be done using a coupled SIMO-RIFLEX model where the wind turbine including substructure is modelled in SIMO and the mooring system is modelled in RIFLEX. The motions of the floating wind turbine and the motions and tension responses in the mooring lines are simulated simultaneously. Hence, the stiffness from the mooring lines on the FWT will be updated for every time step.

The mooring line tension will be a function of the position, velocity and acceleration of the floater, as well as current and wave forces acting directly on the mooring lines. Time series of the mooring line tension for the whole simulation is outputted from SIMA and will be used as basis for the statistical analyses.

The SIMA model will be further explained in Chapter 8.

Chapter 5

Design Limit States for Mooring Systems

This Chapter describes existing limit states and acceptance criteria for floating wind turbines as defined in DNVGL-ST-0119. Focus will be on short term design methods for catenary systems.

5.1 Definition of relevant Limit States

According to DNV GL the **Ultimate Limit States (ULS)** correspond to "the maximum load-carrying resistance" *DNVGL-ST-0119 Floating wind turbine structures* (2018).

The **Accidental Limit States (ALS)** are "survival conditions in a damaged condition or in the presence of abnormal environmental conditions" *DNVGL-ST-0119 Floating wind turbine structures* (2018). For the mooring system, a relevant accidental limit states will typically be failure of one of the mooring lines. In addition the ALS include abnormal environmental loads, which for a floating wind turbine are loads with return period 500 years according to DNVGL-ST-0119.

In addition it should be mentioned that the **Fatigue Limit States (FLS)**, which corresponds to failure due to the effect of cycling loading is a very relevant limit state for design of mooring systems for offshore wind turbines. This is due to the aspects discussed in sec-

tion 3.4. However, this thesis will not focus on fatigue and hence FLS will not be further described.

5.2 Ultimate Loads

The design tension in a mooring line is in DNVGL-ST-0119 defined as

$$T_d = \gamma_{mean} \cdot T_{c,mean} + \gamma_{dyn} \cdot T_{c,dyn} \tag{5.1}$$

where $T_{c,mean}$ is the characteristic mean tension, $T_{c,dyn}$ is the characteristic dynamic tension and γ_{mean} and γ_{dyn} are load factors. The characteristic mean tension, $T_{c,mean}$, is defined as the mean part of the 50-year value of the line tension. The characteristic dynamic tension, $T_{c,dyn}$ is defined as the dynamic part of the 50-year value of line tension, and is caused by oscillatory low-frequency and wave-frequency effects, *DNVGL-ST-0119 Floating wind turbine structures* (2018). How these tensions are calculated is described in section 5.2.1.

An important consideration is for what turbine condition the governing ULS cases for mooring design will be found. According to the standard, both cases with 50-year return period environmental conditions where the turbine will be parked and conditions with maximum turbine thrust shall be checked.

5.2.1 Obtaining the mean- and dynamic tensions from time domain simulations

For details regarding how the characteristic mean tension and characteristic dynamic tension can be obtained from time domain simulations *DNVGL-ST-0119 Floating wind turbine structures* (2018) refers to *DNVGL-OS-E301: Position mooring* (2015). Here, several approaches are described. Those considered most relevant will be briefly accounted for in the following section, for details it is referred to *DNVGL-OS-E301: Position mooring* (2015).

Environmental input to the time domain simulations

The H_s, T_P and mean wind speed used as input for the time domain simulations should

be taken from the contour line corresponding to 50 year return period defined using an inverse FORM approach. Several sea states along this contour should checked in order to identify the combination of H_s, T_p and wind speed leading to a most unfavorable line tension.

The 50-year contour can be established under the assumption of direction-independent environmental loading acting in the direction which is most unfavorable for the mooring. This approach will be applied in this thesis. Alternatively, the directional distributions can be accounted for in a more detailed manner according to the methodology described in NORSOK N-006, *DNVGL-ST-0119 Floating wind turbine structures* (2018).

Usually, current corresponding to a 10-year return period is used in combination with the waves and wind with 50 year return period.

Statistical approach to obtain the mean- and dynamic tension from time domain simulations

When the point along the environmental contour lines resulting in the highest mooring line tension is found, there are two different approaches to establish the characteristic tensions which are described in *DNVGL-OS-E301: Position mooring* (2015). The first is to run one long time domain analysis and fit a 3-parameter Weibull distribution to the global maxima. The required length for the simulation will depend on the response under consideration. The requirement according to DNVGl-OS-E301 is that the simulation length is sufficient to provide adequate statistics for the 3 hour extreme value. If low-frequent motions are important for the response under consideration, the required simulation length is increased. A global maxima for the line tension is taken as the maximum value between to mean upcrossings. A Gumbel extreme value distribution can then be obained based on the Weibull distribution for global maxima. The characteristic dynamic tension is taken as the most probable maxima (MPM) in the Gumbel distribution. The characteristic mean tension is taken as the mean tension found in the simulation.

The second approach is quite similar, but instead of running one long analysis, 10-20 realizations of duration 3 hours are simulated. The maximum line tension from each simulation is used to obtain an extreme value sample for which a Gumbel distribution is fitted. The characteristic tension, T_c is taken as the MPM value of the Gumbel distribution. The characteristic mean tension is normally taken as the mean tension found from all simulations (this will be approximately constant independent of seed number) and the characteristic dynamic

tension is found as $T_{c,dyn} = T_{MPM} - T_{c,mean}$. When discussing characteristic tension, T_c, related to short term analysis later in the thesis, this refers to $T_c = T_{c,mean} + T_{c,dyn}$.

The latter approach will be used in this thesis.

5.2.2 Load factor requirements

Note that the load factors are functions of the consequence class. For consequence class 1, failure is unlikely to lead to unacceptable consequences such as loss of life, collision with an adjacent structure and/or environmental impacts. In consequence class 2, failure may well lead to these types of unacceptable consequences, *DNVGL-ST-0119 Floating wind turbine structures* (2018). Table 5.1 defines the requirements for load factors for design of mooring lines.

Limit state	*Load factor*	*Consequence class*	
		1	*2*
ULS	γ_{mean}	1.3	1.5
ULS	γ_{dyn}	1.75	2.2
ALS	γ_{mean}	1.00	1.00
ALS	γ_{dyn}	1.10	1.25

Table 5.1: Load factors for design of mooring lines

5.3 Resistance

The characteristic capacity of the mooring line is defined by *DNVGL-ST-0119 Floating wind turbine structures* (2018) as

$$S_C = \mu_S \cdot (1 - COV_S \cdot (3 - 6 \cdot COV_S)); \qquad COV_S < 0.10 \tag{5.2}$$

where S_C is the characteristic capacity of the body of the mooring line and μ_S and COV_S are respectively the mean value and coefficient of variation of the breaking strength of the components that make up the main body of the mooring line.

If the statistics of the breaking strength of the components are not available, the characteristic capacity can be taken as

$$S_C = 0.95 \cdot S_{mbs} \tag{5.3}$$

where S_{mbs} is the minimum breaking strength of new components.

If the strength distribution is based on test statistics, a correction of the characteristic capacity should be performed in order to account for statistical uncertainty. This will not be further discussed here, reference is made to DNVGL-ST-0119.

The mooring line will not consist only of the main body, but also for instance connection links and terminations. According to the standard, these shall have characteristic capacities which exceeds the characteristic strength of the main body with a very high level of confidence.

5.4 Design criteria

The design criterion in ULS is

$$S_C > T_d \tag{5.4}$$

where the design tension T_d is established from the procedure described in section 5.2.

The design criterion in ALS is according to *DNVGL-ST-0119 Floating wind turbine structures* (2018) similarly

$$S_C > T_d \tag{5.5}$$

with T_d is in ALS established under the assumption that one mooring line is broken or with an intact mooring system in presence of abnormal environmental loads. According to the definition of ALS given in DNVGL-OS-0119, abnormal environmental loads for a floating

wind turbine should be taken as environmental loads with 500 year return period.

The ratio between the resulting design tension obtained for the intact mooring system using the load factors given in Table 5.1, would then be of interest:

$$r = \frac{T_{d,ALS}}{T_{d,ULS}} \tag{5.6}$$

If r is significantly smaller than 1, the load factors applied in the calculation of ULS loads are sufficiently large so ULS is the governing design criteria for the intact mooring system. On the other hand, if $r \geq 1$, ALS could be the governing design criteria for the mooring system in intact condition. For the case where r is in the range around 1, the ALS case for the intact mooring system should be investigated further as a part of the design process of the mooring system.

Chapter 6

Statistical approaches for estimation of ULS characteristics

As discussed in Chapter 5, normal practice today is to use a short term approach for predicting long term extreme responses in the mooring lines. In general, a long term response analysis will provide most accurate results for the response characteristics of a floating unit, Haver (2017). There are several methods of performing long term response analysis and in this thesis the All Sea State approach and Random Storm approach (POT) will be emphasized.

6.1 Short term response analysis

Although the method will in general provide less accurate results for ULS characterestics than a long term response analysis, short term response analysis is today the preferred when analyzing complex problems where time domain simulations are required for solving the equation of motion. This is due to the effectiveness of the method considering that a relatively small amount of analyses are required compared to long term response analyses for the same type of response. A typical short term approach is described in Chapter 5.2.1.

6.2 Long term response analysis

For responses which can be considered as linearly related to the wave process, the response will be given by the response amplitude operators (RAOs) of the unit. Hence, the response analysis can be performed in the frequency domain and a long term analysis will not require much time or computer resources.

However, if the response of interest is of a strong non-linear nature, time domain analyses are often required. This will in general require a large amount of numerical simulations and is hence time consuming. Long term response analysis based on time domain simulations will be the main focus here.

6.3 All Sea States approach

Often, it is of interest to focus on the extreme responses, for example when the ULS characteristics are to be investigated. The underlying assumption for this method is that the long term climate can be modelled as a step function with constant step length. Within each step, the environmental conditions are considered stationary. In the north sea it is normal practice to choose a duration of 3 hours for each step and this value will hence be used from now. Only the largest maxima of each step is of interest. The long term probability of not exceeding a given response value of x' within an arbitrary 3-hour sea state is then given by

$$F_{X_{\Gamma,3h}}(x') = \int_h \int_t F_{X_{\Gamma_{3h}}|H_S T_P}(x'|h,t) f_{H_s T_P}(h,t) dt dh \tag{6.1}$$

where $F_{X_{\Gamma_{3h}}|H_S T_P}(x'|h,t)$ is the cumulative distribution function of the 3 hour maximum response in each step considered conditionally upon the sea state characteristics. It is here for simplicity assumed that the sea state characteristics are defined by H_s and T_P.

For problems where the environmental loading can be considered a Gaussian process and the response is of linear nature so this also can be considered a Gaussian process, it is relatively simple to establish $F_{X_{\Gamma_{3h}}|H_S T_P}(x'|h,t)$. However, for mooring systems the response can rarely be considered linearly related to the environmental loading. This is due to both second order slow drift effects, non-linear damping of the motions and non-linear stiffness in mooring lines.

The short term distribution of 3 hour extremes can therefore in general not be built on the assumption that the response process is Gaussian distributed. Hence, the global maxima cannot be assumed to be Rayleigh distributed. Instead, the Weibull distribution has proven to be a good model of the distribution of global maxima in a sea state. Following this, the Gumbel distribution is in most cases a good representation of the distribution of the 3-hour extreme value in a sea state provided that the number of global maxima of the response is large enough.

The the following approach can then be used in order to establish a long term distribution for the 3-hour maximum value:

1. Perform k 3-hour simulations of each sea state for a large number of sea states.
2. For each sea state, fit a Gumbel model to the k 3-hour response maxima found from the simulations in order to obtain the Gumbel parameters γ and β for each of the sea states.
3. The Gumbel parameters γ and β for each of the Gumbel distributions can now be used to establish a response surface for the parameters $\gamma = \gamma$(h,t) and $\beta = \beta$(h,t).
4. A long term distribution of the 3-hour maximum can now be found using equation 6.1 and the estimated γ and β values for establishing Gumbel distribution $F_{X_{\Gamma_{3h}}|H_S T_P}(x|h,t)$ for different values of h and t.

Some important assumptions when using the described approach is that sufficiently accurate numerical simulations of the response type of interest can be performed. Another important criteria is that a sufficient amount of different sea states are analyzed in order to obtain accurate estimates for $\gamma = \gamma$(h,t) and $\beta = \beta$(h,t).

The extreme response value corresponding to a return period of T years can now be found by

$$1 - F_{X_{\Gamma,3h}}(x_{\Gamma,T}) = \frac{1}{n_{T,3h}} \tag{6.2}$$

where $n_{T,3h}$ is given as

$$n_{T,3h} = 365 \cdot \frac{24}{3} \cdot T \tag{6.3}$$

An important assumption in the All Sea States approach is that individual global maxima are statistically independent. This assumption is a simplification. There will both be correlation between adjacent maxima in a stationary sea state and between maxima in adjacent sea states. The latter effect is the most important. Due to the assumption of statistical independence which is being used as in the all sea state approach, the method will normally yield results that are approximately 3-5% on the conservative side, Haver (2017).

6.4 Random Storm approach (POT)

The essence of the random storm approach is that instead of considering all sea states, only the sea states with characteristics (for example H_s) over a certain threshold value are included in the sample of sea states forming the basis for the long term extreme value prediction. This is why the random storm approach is often referred to as a peak-over-treshold (POT) approach. The method has been widely used especially in areas with hurricane environment where some extreme sea states are governing for the extreme response design conditions. The extreme storm events are rare, and therefore many years of weather data is necessary in order to obtain a sufficient storm sample. Hence, it is normal to use hindcast data.

The following section will provide a description of how the POT approach can be used to estimate ULS response characteristics based on known environmental data from measurements or hindcast.

6.4.1 Definition of a storm event

The first step of a long term extreme value prediction using the POT approach is to obtain a storm sample for the site under consideration. As previously mentioned, this is often done based on hindcast data. A criteria for environmental characteristics, for instance H_s or wind speed above a certain threshold, is used in order to obtain the sample. For an illustrative

purpose, H_s as weather characteristic will be discussed in the following section, however the same approach also can be used for wind speed. A storm event is defined as a group of adjacent sea states which all have H_s value over the selected threshold. An important assumption in a POT approach is that each storm is statistically independent. In order to reduce correlation between storms, two storm events that occurs within 24 hours are merged into one storm event.

6.4.2 Distribution of the largest value of an arbitrary storm

When a proper sample is defined, consisting of k_0 storms, each storm is modelled as a sequence of stationary sea states of constant duration, often referred to as "steps". The duration of each step has to be decided so the assumption of stationary condition is fulfilled as good as possible. In the North Sea it is normal to use 3 hours as step length, while in an area with hurricane environment a shorter step length has to be used (normally 0.5 hours).

The largest response in each step is normally assumed to follow a Gumbel distribution. The parameters of the Gumbel distributions for the extreme response for each step are normally established based on model tests or time domain simulations. According to Baarholm et al. (2010) the Gumbel parameters can be estimated by running a number of time domain simulations for each step and then use the method of moments to approximate the parameters. The distribution function of the maximum of 3-hour response in step number m of storm number k is then on the form:

$$F_{X_m|k}(x|k) = exp\Big(- exp(-\frac{x - \gamma_{m,k}}{\beta_{m,k}})\Big) \tag{6.4}$$

where X_m is the maximum response in step number m in storm number k, $\gamma_{m,k}$ is the location parameter and $\beta_{m,k}$ is the scale parameters obtained from the time series. The assumption that the extreme values are Gumbel distributed should be validated for the problem under considerations. The global maxima during a 3 hour simulation needs to be large enough for the Gumbel-assumption to hold.

When assuming that the extreme response in each storm step is statistically independent to those of the other storm steps, the distribution function of the extreme value of storm

number k with m steps, Y_k, can be written:

$$F_{Y_k|k}(Y|k) = \prod_{m=1}^{m_k} F_{X_m|k}(y|k) = exp\Bigg(- \sum_{m=1}^{m_k} exp\Big[- (\frac{y - \gamma_{m,k}}{\beta_{m,k}})\Big]\Bigg) \tag{6.5}$$

6.4.3 Predicting ULS characteristics accounting for non-observed storms

In most cases, a small amount of hindcast data is available compared to the return periods of the responses of interest. This is for instance the case when using 38 years of hindcast data as a basis for estimating ULS characteristics with 50 and 500 year return periods. To account for this, the following approach is being applied for predicting ULS response characteristics.

The long term distribution function of the extreme response in an arbitrary storm is considered conditionally upon the most probable largest response, S. Tromans & Vandersohuren (1995):

$$F_Y(y) = \int_{\tilde{y}} F_{Y|\tilde{y}}(y|\tilde{y}) f_{\tilde{Y}}(\tilde{y}) d\tilde{y} \tag{6.6}$$

It is assumed that the conditional distribution of the storm maximum response for a storm given the most probable largest response value of the storm can be approximated by a Gumbel distribution

$$F_{Y|\tilde{Y}}(y|\tilde{y}) = exp\Bigg(- exp\Big[- \frac{y - \tilde{y}}{\beta\tilde{y}}\Big]\Bigg) \tag{6.7}$$

The Gumbel distribution is fitted to the exact distribution given by equation 6.5 according to the following approach. By requiring that the most probable largest storm response maximum for each storm should be equal to the ones obtained from the exact distribution, $\tilde{y}$ is obtained for each storm by equation 6.5. For each storm, β as given in equation 12.9, is then found by requiring that the standard deviation of the Gumbel distribution should be equal to the standard deviation of the exact distribution given by equation 6.5. Hence, a sample of k_0 estimates of β is obtained. Normally, β is assumed to be relatively constant and can hence be taken as the mean value of the sample. This should however be verified by plotting

the sample of β-values against the corresponding sample of $\tilde{y}$. If scatter from storm to storm is relatively small and shows no particular trend, this suggests that using the mean value of the sample as a estimate for β is a good approximation.

The distribution function of the most probable largest value of $\tilde{Y}$ then has to be found. A sample, $\{\tilde{y}_1, \tilde{y}_2, ..., \tilde{y}_{k0}\}$ consisting of the most probable largest response values for each storm is obtained using equation 6.5. A 3-parameter Weibull distribution is fitted to to this sample as it is assumed that is a relatively good model of the distribution function of the most probable largest response, $\tilde{y}$, denoted $f_{\tilde{Y}}(\tilde{y})$.

By using the results found from the described approach, the ULS characteristics can be found from equation 6.6. The ULS characteristic response corresponding to a 50 year return period can then be found by solving

$$1 - F_Y(y_{q_{50}}) = \frac{q_{50}}{n_{1y}} \tag{6.8}$$

where $q_{50} = 0.02$, while n_{1y} is the expected number of storms each year found by

$$n_{1y} = \frac{k_0}{T_{data}} \tag{6.9}$$

where k_0 is the total number of storms in the sample and T_{data} is the number of years with measurements.

6.5 Comparison of key characteristics of the All Sea States approach and Random Storm approach

In both the all Sea States approach and the Random Storm approach two important assumptions are made regarding the statistical independence between the maximum response values. In the All Sea States approach it is assumed that all global maxima are statistically independent. This will lead to conservative results when using this method due to the fact that there will be correlation between maxima in adjacent sea states.

For the Random Storm approach, it is assumed that the extreme value for each of the step in the storm are statistically independent. In addition it is assumed that the storm extremes are statistically independent. These have both proven to be relatively good assumptions. Hence, the random storm approach is expected to yield less conservative results which are more realistic.

An exception is if a storm with characteristics corresponding to a very much higher return period than the observation period is present in the environmental data. For instance, if a storm with characteristics corresponding to a 500 year return period occurs within 50 years of hindcast data this would probably lead to overestimation of the storm characteristics for a storm with return period 50 years. Due to the fact that the Random Storm approach is based on a smaller sample of weather characteristics than the All Sea States approach it will be more sensitive to such abnormal environmental conditions present in the environmental data.

Chapter 7

Metocean data

In this chapter the H_s and mean wind speed corresponding to 50 and 500 year return periods are estimated using a POT approach. The results obtained in this chapter are used both to verify the data given in the Hywind Buchan Deep Metocean Design Basis, Mathisen et al. (2014), as well as the metocean contour lines established in Chapter 11.

7.1 Input

The metocean data used as as input for all further analyses is based on NORA10 hindcast data from Buchan Deep (the Hywind Scotland location). The hindcast data is given every third hour from the 1st of January 1980 to the 28th of February 2018. In other words, 38 years of hindcast data is provided. This is considered sufficient for later using a POT approach for estimating characteristics corresponding to 50 year return period. For the estimation of characteristics corresponding to 500 year return period, there will be a bit more uncertainty related to the the estimates based on the 38 years of data.

7.2 Scatter diagram

In some hindcast data files, the T_p values are given using logarithmic spacing. This leads to a concentration of T_p-values in discrete classes, which is not a good physical representation

of the T_p-values. Hence, the hindcast data was plotted in order to investigate if this was the case.

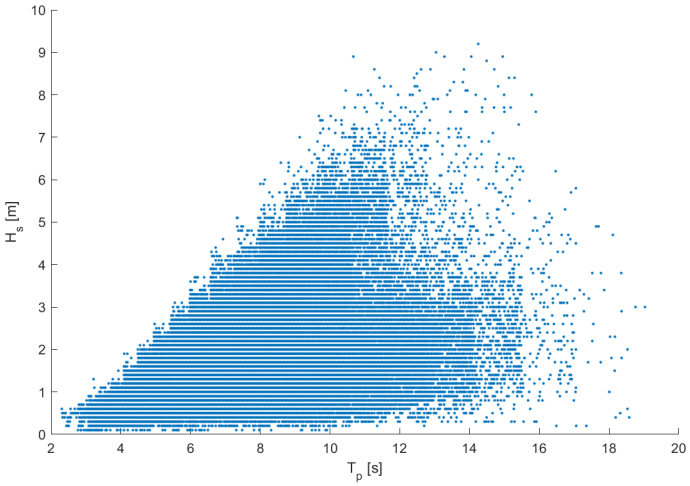

Figure 7.1: Plot of H_s vs T_p.

As seen from Figure 7.1, the T_P spacing is not discrete distributed using logarithmic spacing. This implies that the data has already been modified so the T_p values are randomized around the the logarithmic classes. Hence, no further modification of the data set is needed. The scatter diagram of the 38 years of hindcast data was then calculated. This can be found in APPENDIX A.

7.3 Weibull distribution for estimating H_s corresponding to different return periods

7.3.1 Fitting of Weibull distribution to storm extremes

First, a threshold value $H_s > 6m$ is used to define storm events using the approach described in section 6.4.1. This resulted in a total number of $n_0 = 143$ storms. The largest H_s value during each storm was selected to form a set of extremes, $\{Hs_{max,1}, Hs_{max,2}, ..., Hs_{max,143}\}$. First, the variable $x = H_s - \epsilon$, where $\epsilon = 6m$, is introduced in order to simplify the notation. The 2-parameter Weibull cumulative distribution function for the largest H_s-value in an arbitrary storm can then be fitted to the sample $\{x_1, x_2, ..., x_{143}\}$ and is given by

$$F_X(x) = 1 - exp\Big(- (\frac{x}{\alpha_X})^{\beta_X} \Big) \tag{7.1}$$

where α_X and β_X are the Weibull parameters of the distribution. The parameters α_X and β_X was found using the method of moments as described in Nielsen (2011):

$$\frac{m_2}{m_1^2} = \frac{\Gamma(1 + \frac{2}{\beta_X})}{\Gamma^2(1 + \frac{1}{\beta_X})} \tag{7.2}$$

and

$$\alpha_{H_{s,max}} = \frac{m_1}{\Gamma(1 + \frac{1}{\beta_X})} \tag{7.3}$$

where Γ is the gamma-function and m_1 and m_2 are the first and second moment of the distribution given by

$$m_k = \frac{1}{n_0} \sum_{i=1}^{n_0} x_i^k \tag{7.4}$$

n_0 is the number of storms, which for this case is 143.

The values of β_X was found using the bisection method to solve equation 7.2. Then, the value of α_X could easily be established using equation 7.3. This approach resulted in the following Weibull parameters:

Weibull parameter	**Value**
α_X	0.9007
β_X	1.1278

The fitted Weibull distribution of largest H_s-value in an arbitrary storm was then plotted together with the actual observations on Gumbel paper as seen in Figure 7.2. The values on the horizontal axis is number of meters above the threshold of 6m.

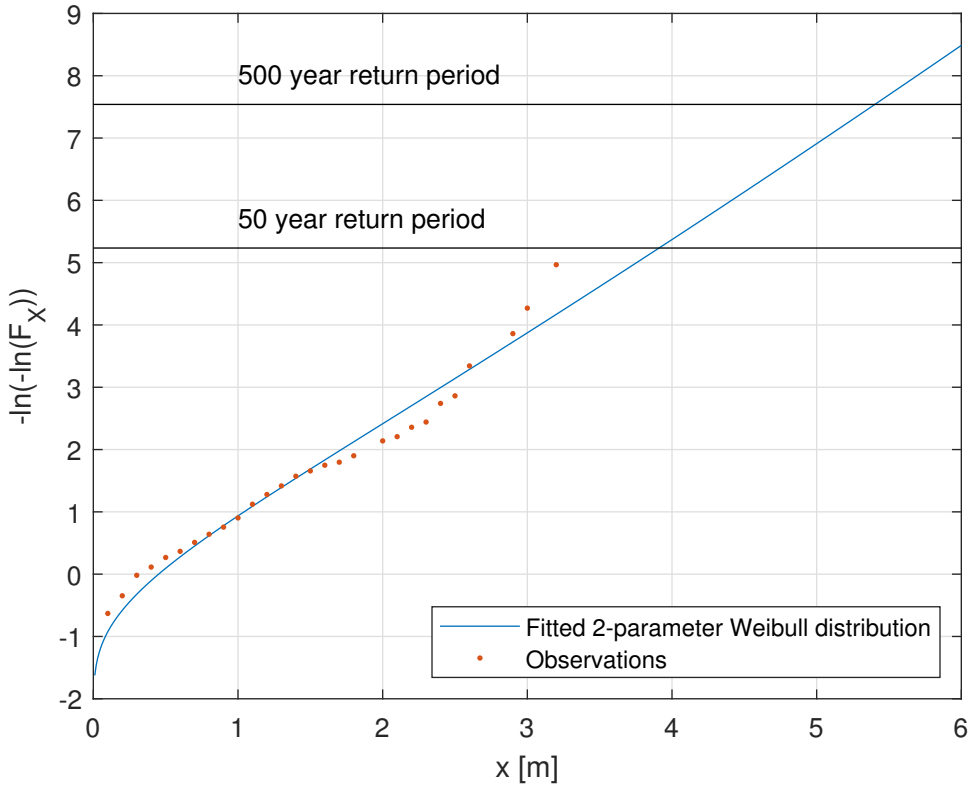

Figure 7.2: 2-parameter Weibull distribution and Hs observations plotted on Gumbel paper

7.3.2 Calculation of H_s values corresponding to different return periods

The H_s value which corresponds to a return period of T years is the H_s value which has an annual exceedance probability of $q_T = 1/T$. This can be found solving the equation 7.5 for x_q and then adding the storm threshold value:

$$1 - F_X(x_q) = \frac{q_T}{n_{1y}} \tag{7.5}$$

where q_T is given as $\frac{1}{T}$ and n_{1y} is the expected number of storms each year simply found by

$$n_{1y} = \frac{n_{storms|\epsilon}}{n_{years}} \tag{7.6}$$

where $n_{storms|\epsilon}$ is the total number of storms in the sample.

The Hs value corresponding to a return period of T years is then given by

$$h_{sq} = x_q + \epsilon \tag{7.7}$$

where ϵ in this case is 6m.

The results for the given storm threshold value of $\epsilon = 6m$ is summarized in table 7.1 and compared to the values given in the Buchan Deep Metocean Design Basis (Mathisen et al. (2014)). From now, the Buchan Deep Metocean Design Basis will be referred to as the *Metocean Design Basis*.

Return period	**Hs calculated from fitted Weibull distribution [m]**	**Hs given in Metocean Report [m]**
1 year	7.2	7.8
10 years	8.8	9.4
50 years	9.9	10.5
500 years	11.4	-

Table 7.1: Comparison between H_s values found from the fitted Weibull distribution and those given in the Metocean Design Basis.

As seen from Table 7.1, the calculated vales are 0.6m smaller than those given in the Metocean Design Basis for H_s corresponding to 1, 10 and 50 year return periods. It is expected that the POT approach applied here will give lower estimates than those obtained in the Metocean Design Basis considering the fact that an all sea state approach is applied in the Metocean Design Basis.

7.3.3 Sensitivity study of H_s-threshold

In the calculations presented in section 7.3.1, a threshold value of $\epsilon = 6m$ for the H_s was used to define a storm event. It is of interest to investigate how sensitive the results are with respect to choice of threshold value. Hence, the procedure described in section 7.3.1 was repeated for ϵ values of 3,4 and 7 m. The results are summarized in Table 7.2.

	Treshold 3m	Treshold 4m	Treshold 6m	Threshold 7m	Metocean Design Basis
Number of storms	1471	824	143	48	-
Hs, 1 year return period [m]	7.2	7.2	7.2	7.3	7.8
Hs, 10 year return period [m]	9.4	9.0	8.8	8.7	9.4
Hs, 50 year return period [m]	10.8	10.2	9.9	9.6	10.5
Hs, 500 year return period [m]	12.7	11.9	11.4	10.6	-

Table 7.2: H_s values calulated using different thresholds for storm definition.

As seen from Table 7.2, the estimated H_s value corresponding to a 50 year return period tends to increase for a lower threshold value. Note also the increase in total number of storms for decreasing threshold values. It was decided that a threshold value of 6 metres was adequate as it includes a sufficient number of storms, without including storms which will obviously not be of any importance when estimating the H_s value corresponding to a 50 year return period.

7.4 Weibull distribution for estimating wind speeds corresponding to different return periods

Instead of using the significant wave height to define storm events, wind speed can be used. The wind speeds provided in the Nora10 hindcast data represents the 1-hour mean wind speed, Mathisen et al. (2014), and is given with a sampling period of 3 hours.

By using a threshold value of $\epsilon = 23m/s$, the following Weibull parameters for the parameter $X = U_{wind} - \epsilon$ were obtained and presented in Table 7.3.

Weibull parameter	Value
α_X	1.9468
β_X	1.1534

Table 7.3: Weibull parameters for 2-parameter Wibull fit to maximum wind speeds.

The corresponding Weibull curve is plotted on Gumbel paper in Figure 7.3.

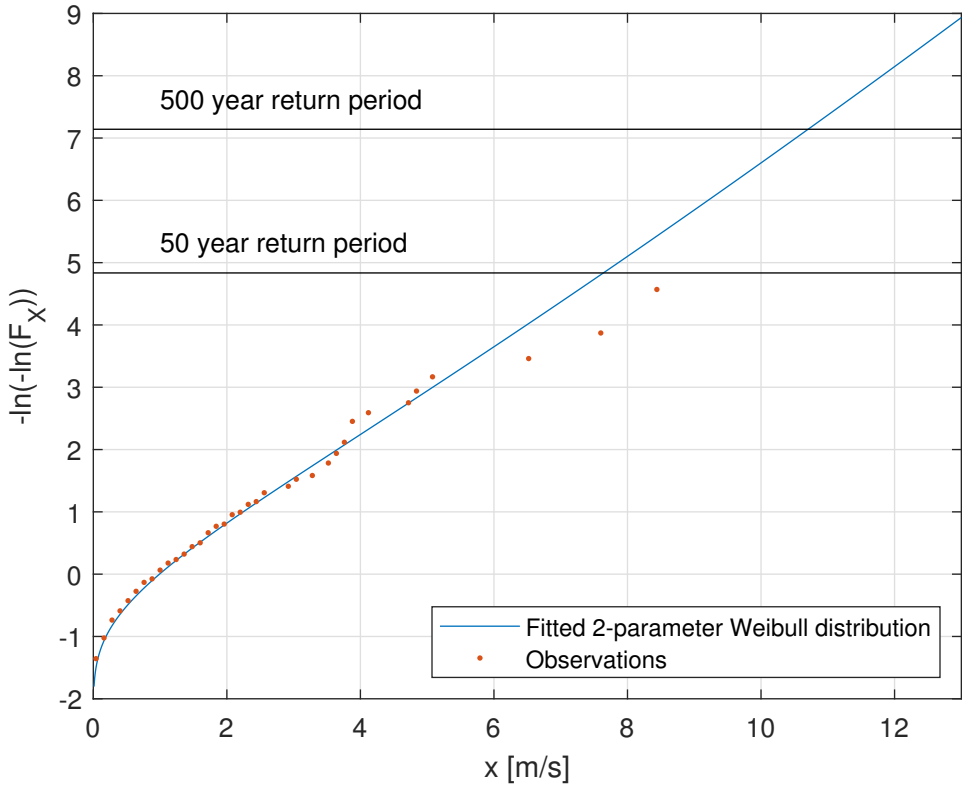

Figure 7.3: 2-parameter Weibull fit to the max wind speed in each storm plotted together with observations.

Table 7.4 shows the results of the estimated wind speeds corresponding to different return period. The values represent 1 hour wind speed based on a sampling interval of 3 hours.

	Threshold 21 m/s	**Threshold 23 m/s**	**Threshold 25 m/s**	**Metocean design basis**
Number of storms	241	96	34	-
$\boldsymbol{U_{10}}$**, 1 year return period [m/s]**	24.7	24.8	24.8	26.5
$\boldsymbol{U_{10}}$**, 10 year return period [m/s]**	28.6	28.4	28.4	29.5
$\boldsymbol{U_{10}}$**, 50 year return period [m/s]**	31.1	30.6	30.7	31.0
$\boldsymbol{U_{10}}$**, 500 year return period [m/s]**	34.7	33.7	34.0	-

Table 7.4: Wind speeds estimated using different threshold for defining a storm event.

As seen from Table 7.4, the estimated value for the wind speed corresponding to a 50 year return period is very little sensitive to the chosen threshold value. It also corresponds very well with the value given in the Metocean Design Basis.

7.5 Calculating 50 year return period H_s using a Generalized Pareto distribution for storm extremes

7.5.1 Fitting a Generalized Pareto distribution to storm extremes

An alternative to using a 2-parameter Weibull distribution to model the storm extremes is the Generalized Pareto distribution given in Haver (2018). Once again the parameter $X = H_s - \epsilon$ is introduced in order to simplify the notation. The 2-parameter Generalized Pareto distribution is then given by

$$F_X(x) = 1 - \Big[1 + \frac{a \cdot x}{b}\Big]^{-\frac{1}{a}} \tag{7.8}$$

Once again, a H_s threshold value of 6 metres is used in order to define storm events. The Generalized Pareto parameters, a and b are found by using the method of moments as given in Singh & Guo (1997):

$$a = -\frac{1}{2}\big(\frac{m_1^2}{s^2} - 1\big) \tag{7.9}$$

$$b = \frac{1}{2}m_1\big(\frac{m_1^2}{s^2} + 1\big) \tag{7.10}$$

where m_1 is the mean value of the sample and s^2 is the sample variance.

The results are shown in Table 7.5.

Generalized Pareto parameter	**Value**
a_X	-0.1290
b_X	0.9735

Table 7.5: Generalized Pareto parameters for Generalized Pareto fit to maximum H_s values.

The resulting distribution can be observed in Figure 7.4.

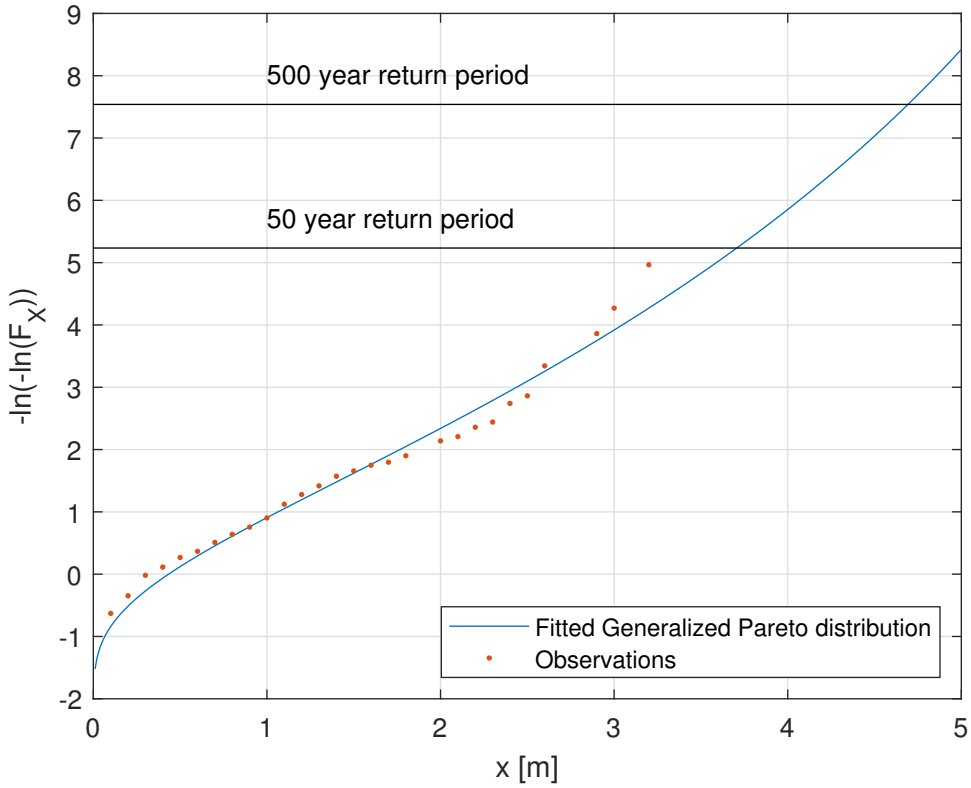

Figure 7.4: Generalized Pareto distribution.

7.5.2 Monte Carlo simulations to check if the estimators are unbiased

Both the Generalized Pareto distribution parameters, a and b, were estimated using moment estimators based on the sample of storm maxima. The sample only consists of 143 storm maxima and there is a risk that the estimated Generalized Pareto parameters are bias due to the relatively small sample they are estimated from. In order to investigate if this is the case, Monte Carlo simulations were performed in MATLAB.

First, random numbers, R, in the range (0,1) were generated using the *rand* function in MATLAB. Based on the random numbers, samples of x values could be generated based on the fitted distribution using $x = F^{-1}(R)$. 500 sets, each consisting of 143 Monte Carlo generated x-values were generated. For each of the sets, the Generalized Pareto parameters

a and b were estimated using the method of moments as described in section 7.5.1. The mean value of the 500 estimated values of a and b respectively, could be compared to the parameters obtained from the real sample. The results are shown in Table 7.6.

Generalized Pareto parameter	**Obtained from real sample**	**Mean values obtained from Monte Carlo generated samples**
a	-0.1290	-0.1440
b	0.9735	1.0305

Table 7.6: Comparison between Generalized Pareto Parameters estimated from real samples and Monte Carlo generated samples.

As seen from Table 7.6, there are some deviations between the parameter values calculated from the real sample and the Monte Carlo generated samples.

Both the distribution fitted to the real sample and that using the mean value of the parameters found from all Monte Carlo simulations are plotted as a red and green line, respectively, in Figure 7.5. In addition, the distribution functions fitted to each of the 500 Monte Carlo generated samples are plotted using blue lines in the same figure. The black, horizontal line in the figure marks the probability level corresponding to 50 year return period. The vertical lines indicates the upper and lower limit of the 90% band of the X corresponding to 50 year return period of the distribution functions based on the Monte Carlo simulated samples. This was simply found by excluding the 5% highest and 5% lowest estimates of Hs_{50} from the 500 estimates provided from the Monte Carlo simulated samples.

It is seen that the curve found from fitting to the real sample lies very close to the one based on the mean values of a_X and b_X found from the Monte Carlo simulations. The distribution function fitted to the real sample in addition provides an estimate very close to the mean value of the 90% band for Hs_{50}. This indicates that the bias in the Generalized Pareto parameters estimated from the real sample is relatively small. However, for further work it would be interesting also to establish confidence levels for the parameters a_X and b_X found from the Monte Carlo simulations and not only for the Hs_{50} resulting from the distribution functions obtained using the parameters. However, this was not performed in this project.

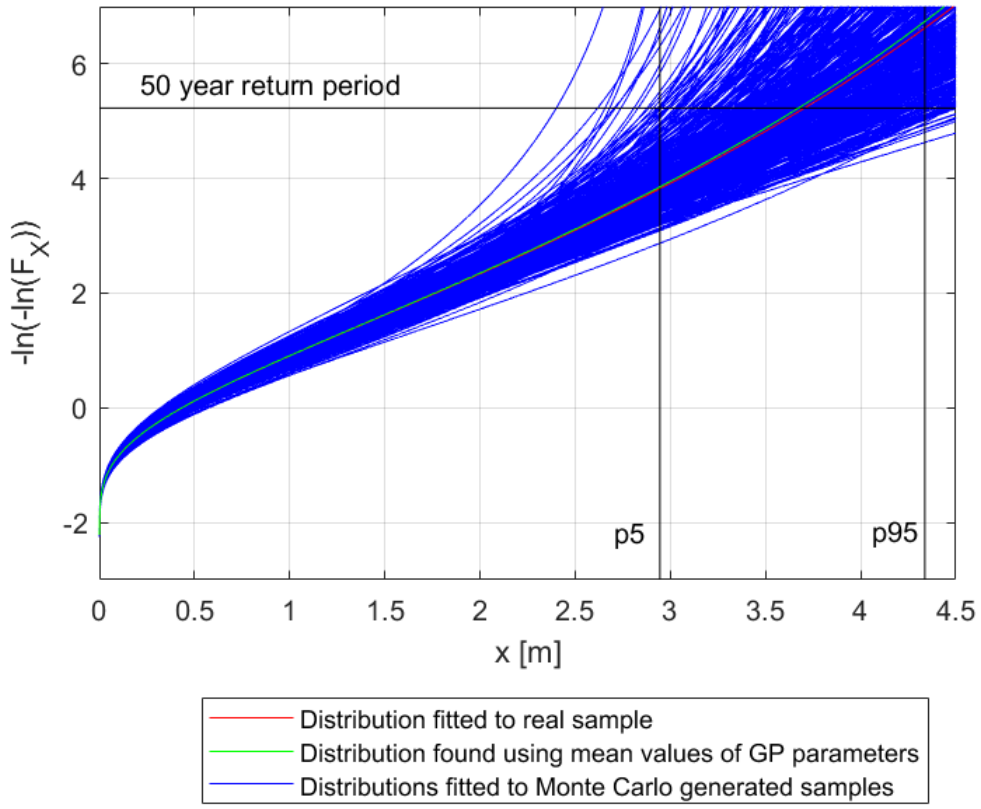

Figure 7.5: Monte Carlo simulation to generate a large sample of Hs values.

7.5.3 Comparison of fitted Generalized Pareto distribution and fitted 2-parameter Weibull distribution

In order to compare the fitted Generalized Pareto distribution with the 2-parameter Weibull distribution obtained in section 7.3.1, both distribution functions were plotted together in Figure 7.6. Comparing the curves with the observations, it seems like the Generalized Pareto distribution better captures the trend of the the observed tail values for $Hs > 8.5$.

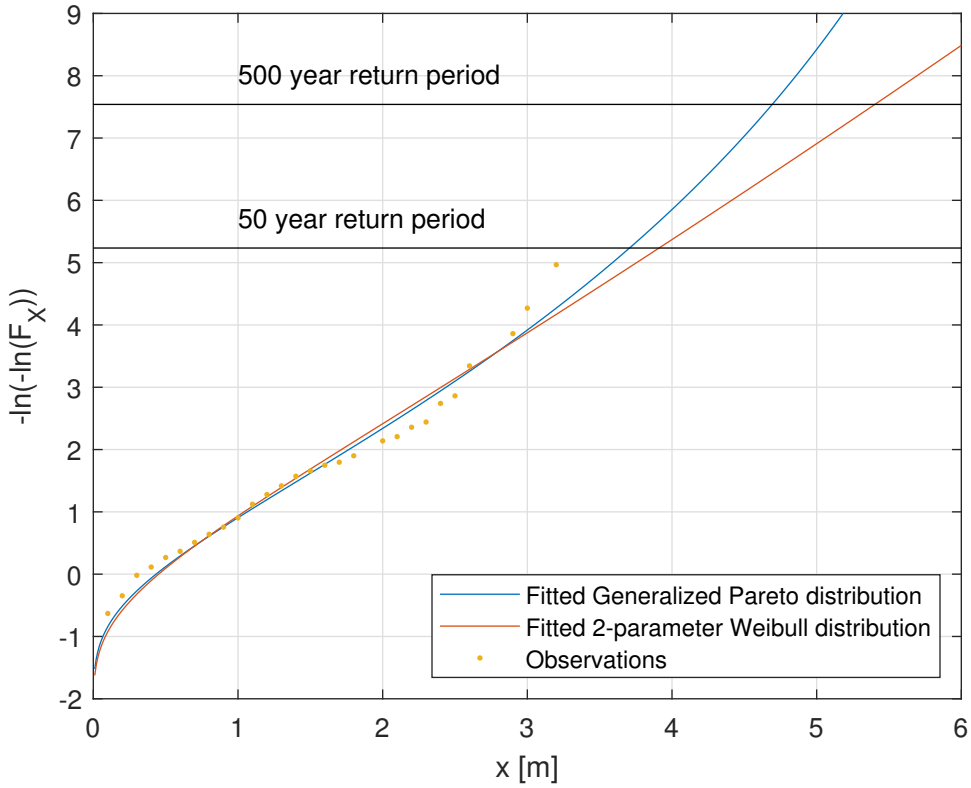

Figure 7.6: Comparison of Generalized Pareto distribution and 2-parameter Weibull distribution.

7.5.4 Calculation of H_s values corresponding to 1, 10 and 50 years return periods

The Hs values corresponding to 1, 10, and 50 years return period are compared to those obtained from the fitted Weibull distribution and the values provided in the the Metocean report, Mathisen et al. (2014).

Return period	**Hs, Generalized Pareto [m]**	**Hs, Weibull [m]**	**Hs given in Metocean Report [m]**
1 year	7.2	7.2	7.8
10 years	8.8	8.8	9.4
50 years	9.7	9.9	10.5
500 years	10.7	11.4	-

Table 7.7: Comparison between values obtained with Generalized Pareto Distribution and Weibull distribution.

As seen from the table values, the Hs corresponding to 1, 10 and 50 year return periods are estimated to be very similar according the Generalized Pareto distribution and the 2-parameter Weibull distribution. However, for the H_s value corresponding to 500 year return period, the value obtained from the Generalized Pareto distribution is significantly lower than the one obtained from the Weibull distribution. This is in good accordance with the observed curve shapes in Figure 7.6.

Chapter 8

SIMA model

SIMA version 3.6.0 which runs SIMO version 4.0.0 and RIFLEX version 7.1.1 is used for all time domain simulations in this thesis.

The SIMA model is based on the design proposed by Wang (2014). Running simulations with a full model of the floating wind turbine would be too time consuming mainly because the aerodynamic rotor load calculations require small time steps. Hence, a simplified model is needed. As a starting point for the construction of the simplified model, a SIMA-model proposed by Hole (2018) was used. This chapter will describe some main features of the model. How the aerodynamic excitation loads were modelled is described in Chapter 9.

8.1 Geometry

Some main features of the geometry are shown in Figure 8.1. The simplified SIMA model is shown in Figure 8.2. The greatest difference from a full model of the FWT is that neither the nacelle or the rotor are modelled in the simplified SIMA model. The pitch control system is hence not included either.

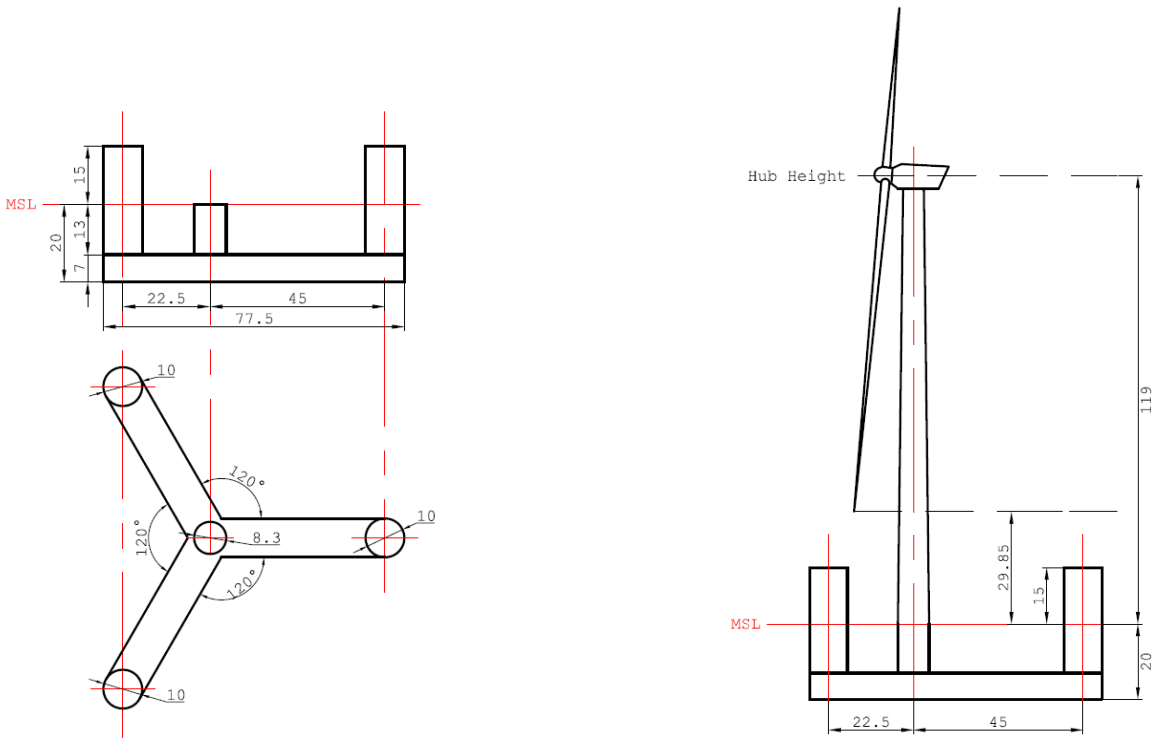

Substructure Full structure

Figure 8.1: Geometry of the structure given by Wang (2014).

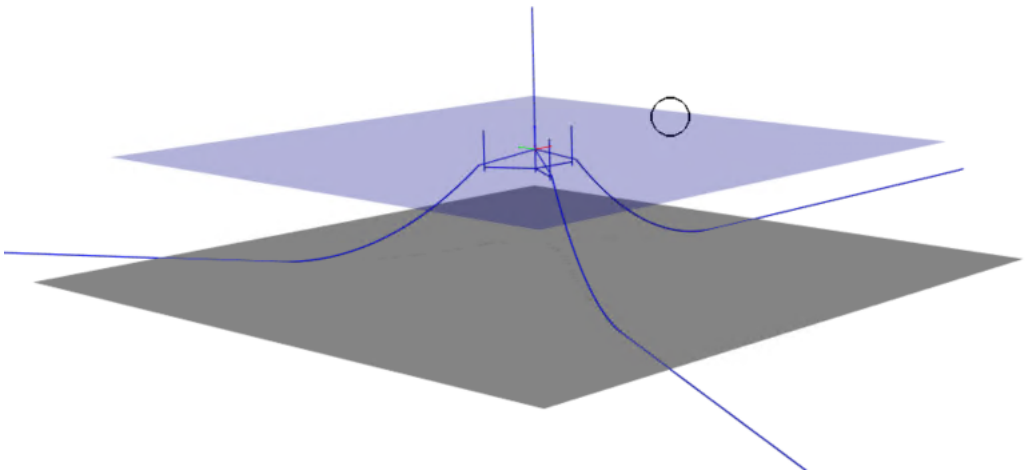

Figure 8.2: Simplified SIMA model

8.2 Definition of coordinate system

The origin of the coordinate system is, if other is not stated, located at the center of the tower when the unit is not exposed to any loads, as shown in Figure 8.3. The z- axis has positive direction out of the paper plane and z = 0 at the sea surface. The x-axis points towards the north. Figure 8.3 also shows the labeling of the three mooring lines.

Angles in the horizontal plane used for defining heading directions of waves, wind and current is defined relative to the positive x-axis and are increasing in the counter-clockwise direction as shown in the figure.

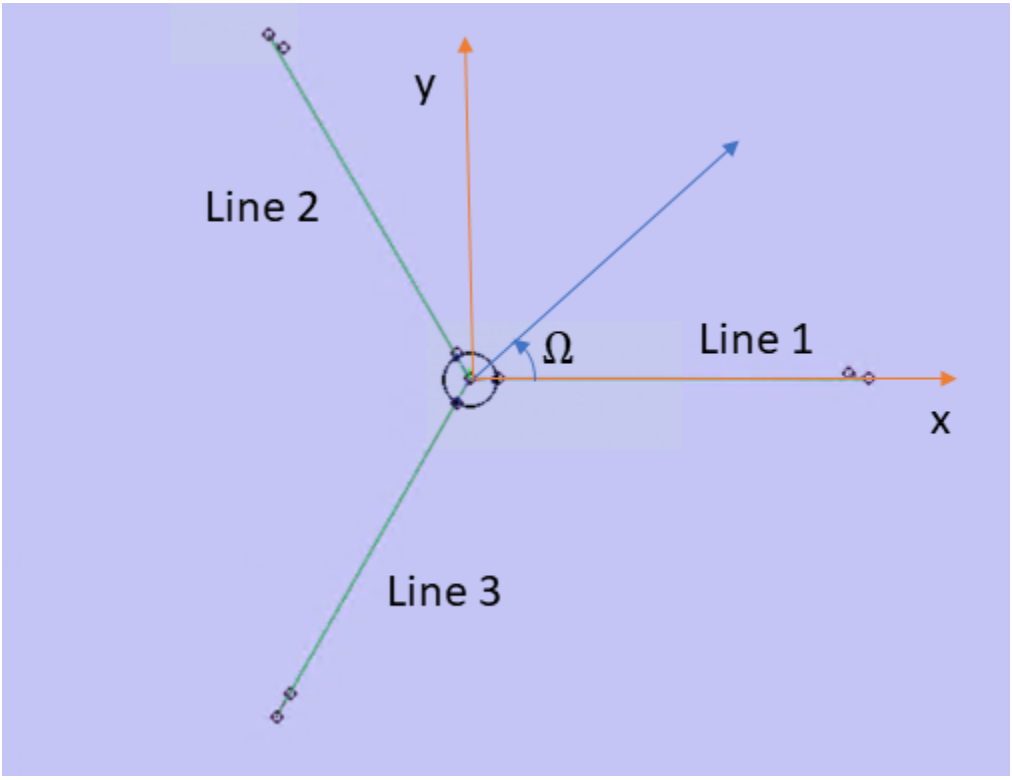

Figure 8.3: Global coordinate system. Note that the x-axis points towards the north.

8.3 SIMO body

The SIMA model consists of a SIMO body with SIMO slender elements used to model the substructure and tower. The mooring lines are modelled using RIFLEX slender system.

Some key specifications for the SIMO body are listed below:

Structural mass
The structural mass and the position of the mass center is specified on the SIMO body. This mass includes the mass from all components of the full model except mooring lines. In addition, the moments of inertia are defined. Detailed calculation of both the mass and the moments of inertia is presented in section 8.4.

Hydrostatic stiffness data
The hydrostatic stiffness data is specified directly for heave, pitch and roll and do only account for water plane stiffness.

Retardation function and first order wave load transfer function
Both the added mass at infinity frequency, the retardation function and the first order wave load transfer functions for the structure were provided by Associate Professor Erin Bachynski at the Institute for Marine Technology at NTNU. She had performed the calculations using WADAM.

Slender elements
The pontoons and columns of the substructure are modelled as slender elements where gravity and buoyancy of the elements was not included. Their function is solely to model the drag forces on the substructure correctly. Based on *DNVGL-RP-C205 Environmental conditions and environmental loads* (2017), drag coefficients of 1.95 and 0.7 were used for the pontoons and columns respectively.

8.4 Inertia

The inertia of the structure was calculated based on the weight distribution and geometry considerations given by Wang (2014). The total mass of the model was found by adding the contributions from the semi substructure, the tower, nacelle and the rotor. The geometry of the structure is pictured in Figure 8.1.

8.4.1 Mass

The mass was found by simply adding the contributions from the different structural components and the ballast. Note that the mass of the mooring lines are not included. The reference system used in Table 8.1 has origin where the waterline intersects the centre of the middle column in the substructure. All input values for the calculations are presented by Wang (2014).

Component	**Mass (tonnes)**	**COGX**	**COGY**	**COGZ**
Substructure (excluding ballast)	2588	0	0	-9.6
Ballast	10188	0	0	-16.5
Rotor	230	-7.1	0	119.0
Nacelle	446	2.7	0	121.5
Tower	628	0	0	47.6
Total	**14080**	**0**	**0**	**-5.8**

Table 8.1: Mass distribution

8.4.2 Moments of inertia

In general, the moment of inertia of a structure with respect to a given axis, i, is given by

$$I_i = \int_M r^2 dm \tag{8.1}$$

where r is the distance from the axis to the mass element dm, Lien & Løvhøiden (2015). In order to simplify the calculations, the structure is divided into several components and the contributions to the total moment of inertia is calculated separately and then added together to find the total moment of inertia of all principal axes. Here, the parallel axis theorem is a useful tool. It states that the moment of inertia about an axis i of a structural part which do not have its local centre of gravity located on the axis, can be written as a sum of the local moment of inertia of the structural component and the Steiner contribution:

$$I_i = I_{i,loc} + Ms^2 \tag{8.2}$$

where $I_{i,loc}$ is the moment of inertia of the component about a local axis passing through the components local centre of gravity and is parallel to the principle axis i. s is the distance from the local axis i, loc to the principle axis i and M is the mass of the structural component.

The coordinate system used for the calculations has origo in the mass center of the structure. Referring to the substructure in Figure 8.1, the x-axis is a horizontal line passing through the center of the tower. The key results from the calculations are presented in Table 8.2. In the following, the procedure of calculating the contributions from all components of the structure to the total moment of inertia will be described.

Pontoons (including ballast)

Each pontoon was approximated as a box with constant mass density which includes both the steel weight of the pontoon and the ballast. Due to the shape of the substructure, the moment of inertia is equal about both the x- and y-axis. Hence, only the moment of inertia about the x-axis was calculated. The local moment of inertia for the pontoon with mass center on the x-axis could simply be found from the formula

$$I_{x,loc} = \frac{1}{12}(l^2 + h^2) \tag{8.3}$$

where l is the length of the pontoon and h is the height. For the two pontoons which do not have mass center on the x-axis, the integral presented in equation 8.1 was solved:

$$I_{x,loc} = \int_M r^2 dm \approx \int_{-L/2sin(120^\circ)}^{L/2sin(120^\circ)} \int_{-h/2}^{h/2} \rho \cdot L/2 \cdot sin(120^\circ) \cdot (y^2 + z^2) dz dy \tag{8.4}$$

where L is the length of a pontoon (50m), h is the height of the pontoon (7m), ρ is the density of the column including steel and ballast water (1166 kg/m^3). It is referred to Figure 8.1 for better understanding of equation 8.4.

Columns

The columns of the substructure have a small wall thickness compared to the radius. Hence, their local moments of inertia about the x- and y-axis can be calculated by:

$$I_{x,loc} = I_{y,loc} = \frac{1}{12}(3r^2 + h^2) \tag{8.5}$$

where r is the outer radius and h is the height of each column. The local moment of inertia about the z-axis is found by using

$$I_{z,loc} = \frac{1}{2}mr^2 \tag{8.6}$$

As expected, the most significant contribution from the columns to the global moments of inertia comes from the Steiner contributions.

Tower

The tower is considered as a slender rod which goes from the pontoon to the centre of the nacelle. According to Lien & Løvhøiden (2015), the local moment of inertia about the x- and y-axis can then be found from

$$I_{x,loc} = I_{y,loc} = \frac{1}{12}mL^2 \tag{8.7}$$

where L is the length of the tower. The Steiner addition for the tower is also a significant part of the total contribution to the moment of inertia of the structure.

Rotor and nacelle

Both the rotor and nacelle are approximated as point masses, and hence only their Steiner contributions are included in the calculations.

Total result

Table 8.2 shows the results of the inertia calculations. According to Wang (2014), the total moment of inertia about the x- and y-axis should each be 2.15E+10 kgm^2, which is very similar to the results found in this thesis. The small deviation in results could be due to different simplifications used to calculate the local moments of inertia for the structural parts. Hence, the results presented in Table 8.2 are assumed to be correct and will be used in further calculations.

The results for I_z for the whole structure as shown in table very similar to those obtained by Hole (2018) and will also be used in further calculations.

Component	Mass [t]	Local I_x	Steiner x	Global I_x	Local I_y	Steiner y	Global I_y	Local I_z	Steiner z	Global I_z
Pontoons (including ballast)	11771	1.32E+09	5.03E+09	7.49E+09	-	-	7.49E+09	2.50E+09	7.36E+09	9.86E+09
Columns	1005	7.19E+07	1.07E+09	1.14E+09	7.19E+07	1.07E+09	1.14E+09	2.51E+07	2.04E+09	2.07E+09
Tower	628	9.12E+08	2.98E+09	3.89E+09	9.12E+08	2.98E+09	3.89E+09	2.98E+07	0	2.98E+07
Nacelle	446	0	6.58E+09	6.58E+09	0	6.58E+09	6.58E+09	0	0	0
Rotor	230	0	3.26E+09	3.26E+09	0	3.27E+09	3.27E+09	0	1.20E+07	1.20E+07
Total	14080		**Total I_x:**	2.12E+10		**Total I_y:**	2.12E+10		**Total I_z:**	1.20E+10

Table 8.2: Detailed calculation results for moment of inertia.

8.5 Initial mooring line design

The mooring system is modelled in RIFLEX. The initial design of the mooring lines was inspired by the system used for Hywind Scotland. The lines were modelled as 147mm chain, which is the same as used for Hywind Scotland, Statoil (2014). The mooring line length of Hywind Scotland was used as a starting point, but was modified a bit due to the difference in the location of the fairleads on the Hywind concept compared to the CSC. The final mooring line length was then chosen to be 648 metres.

In order to find a suitable anchor radius, equation 3.6 was used to provide a starting point. It was assumed that a pretension a bit above 1000kN would be appropriate. After some testing, the anchor radius was set to 627 m, resulting in a pretension of 1100kN in the lines.

The traditional design method applied in Chapter 11 was used to verify that the mooring system meets the capacity requirements outlined in *DNVGL-ST-0119 Floating wind turbine structures* (2018). This is described in Chapter 11.

Chapter 9

Modelling aerodynamic excitation forces and damping

In order to get a realistic model of the FWT, it is crucial to be able to model both the aerodynamic excitation loads and the aerodynamic damping as realistic as possible in SIMA. The aerodynamic loads on the model consists of two main contributions:
1. Thrust loads on the rotor.
2. Drag loads on the tower and the part of the substructure above water.

Two main approaches to model the aerodynamic excitation loads and damping were considered:

Approach 1: Use a combination of quadratic wind coefficients, linear damping matrices in SIMO and specified forces and moments.

Approach 2: Use slender elements in combination with specified forces and moments.

For the final model, approach 2 was used. However, Approach 1 will also be described since this provides a good physical understanding of the aerodynamic forces, as well as useful quantification of which loads are governing in each wind regime. In addition, some of the findings from modelling using Approach 1 are used in Approach 2.

Before going in detail on both approaches, some general considerations regarding the ro-

tor thrust are made in Chapter 9.1.

9.1 Thrust force on the rotor

The thrust on the rotor is governed by the blade pitch. For the DTU 10 MW reference turbine, the thrust curve is as given in Figure 9.1.

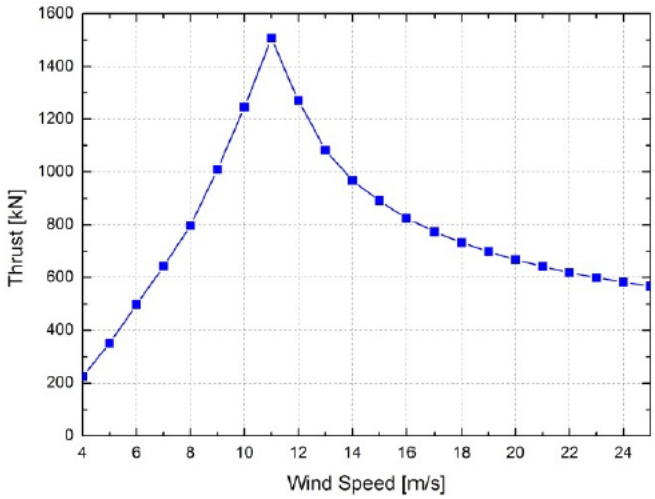

Figure 9.1: Thrust curve as presented in Wang (2014) based on Bak & Zahle (2013). The wind speed on the horizontal axis is wind speed in hub height (119m above surface).

The plot is based on point estimates of the thrust force marked as dots in the plot. Hence, the peak in the thrust curve seems to be located at 11.0 m/s. The actual peak in the thrust curve will be at wind speed 11.4 m/s, which is the rated wind speed. For wind speeds higher than the rated, the blade pitch control system is activated and the blades are pitched in order to keep the power output or the torque (depending on the operational system) constant. Hence, the thrust on the rotor will decline for increasing wind speeds above the rated.

The wind regime above the cut-in wind speed of 4 m/s can be divided into three different regimes:

1. Below rated (4-11.4m/s). In this regime, the operational pitch controller is inactive and the blade pitch is hence constant.

2. Operational regime above rated (11.4-25m/s). The blade controller is active and the blades are pitched so the thrust decreases with increasing wind speed.

3. Shutdown condition (above 25m/s). In this regime the turbine is inactive and the blades are feathered to minimize the thrust.

For a full model, the blade pitch control system will normally be included in the model. However, for the simplified model where the rotor blades are not present, the variations in thrust loads have to be modelled using another approach. This will be discussed in the following sections.

9.2 Approach 1 to model aerodynamic excitation forces and damping

The substructure is modelled using slender elements in SIMA, so the aerodynamic drag contribution from those are already included in the model. All other aerodynamic loads are included either using quadratic wind load coefficients or specified forces and moments. Due to the fact that the tower cross section is circular and that the nacelle is assumed to always have the same angle to the wind, the wind coefficients will be equal for surge and sway. In addition, the wind coefficients will be equal in pitch and roll.

9.2.1 Quadratic wind coefficients

The quadratic wind coefficients are defined so that

$$q_{aero,i} = C_{wind,i} \cdot U_{rel,ref}^2 \tag{9.1}$$

where $C_{wind,i}$ is the quadratic wind coefficient in degree of freedom i and $U_{rel,ref}$ is the relative wind speed in the reference height above the free surface. The reference height was set to 10 metres. When calculating wind coefficient contributions for elements located at other heights than 10 metres (for instance the rotor), the wind coefficient has to include the difference in wind speed from the reference height due to the wind boundary layer. This was implemented

by the use of a power law wind profile as proposed in *DNVGL-RP-C205 Environmental conditions and environmental loads* (2017) with a reference height of 10 metres:

$$U(z) = U_{10}\big(\frac{z}{10}\big)^{0.12} \tag{9.2}$$

where z is the distance above the free surface.

9.2.2 Drag loads on tower

For the tower, the drag contribution was found by dividing it into 12 sections and calculating the total tower contribution to the wind coefficients by superposition of the section contributions. The wind coefficient for sway and surge degrees of freedom will then be given by

$$C_{wind,tower,i} = \sum_{k=1}^{12} \frac{1}{2} C_{D,cyl} \cdot \rho_{air} \cdot d_k \cdot L \cdot \Big((\frac{z_k}{10})^{0.12}\Big)^2 \qquad i = 1, 2 \tag{9.3}$$

where $C_{D,cyl}$ is the drag coefficient a of a cylinder, ρ_{air} is the density of air, d_k is the mean diameter of the cross section of element k, L is the length of the element (10 metres for all elements) and z_k is the distance from the sea surface to the middle of element k.

The value of $C_{D,cyl}$ is a function both of the roughness and the Reynold's number of the flow. The Reynold's number for all flow regimes are relatively high ($Re > 10^6$), and the roughness was chosen to be $k = 5 \cdot 10^{-6}$ which corresponds to a painted steel cylinder according to *DNVGL-RP-C205 Environmental conditions and environmental loads* (2017). Based on figure 9.2, the drag coefficient was then chosen to be 0.7 for all tower sections in all wind regimes.

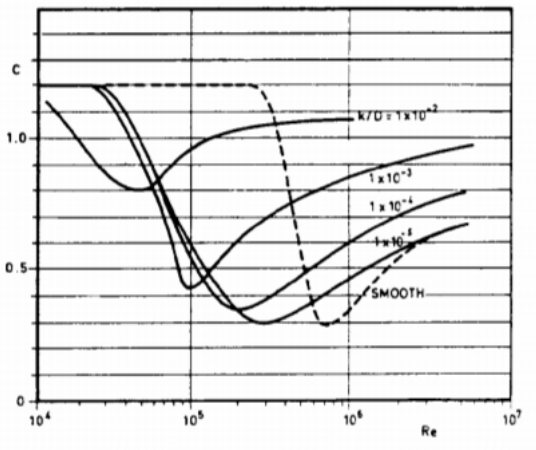

Figure 9.2: Drag coefficients as a function of wind speeds as defined in *DNVGL-RP-C205 Environmental conditions and environmental loads* (2017).

Similarly, the wind coefficients in roll and pitch were found by multiplying the drag force on each tower section by the vertical distance from the middle of the section to sea surface

$$C_{wind,tower,j} = \sum_{k=1}^{12} \frac{1}{2} C_{D,cyl} \cdot \rho_{air} \cdot d_k \cdot L \cdot z_k \cdot \left((\frac{z_k}{10})^{0.12} \right)^2 \qquad j = 4, 5 \tag{9.4}$$

where z_k is the vertical distance from the middle of the tower section to the waterline.

9.2.3 Rotor thrust

In the following sections it is discussed how the thrust excitation loads on the rotor can be modelled in the different wind regimes using quadratic wind coefficients defined on the SIMO body and specified forces and moments.

Rotor thrust below rated wind speed (0-11.4 m/s)
For wind speeds below rated, the thrust force can be approximated by

$$T = C_{w,t1} U_{rel,hub}^2 \tag{9.5}$$

where $C_{w,t1}$ is a constant and $U_{hub,rel}$ is the wind speed in the hub height. Based on the thrust values for the thrust force for wind speeds 8,9,10 and 11 m/s presented in Bak & Zahle (2013), the value of $C_{w,t1}$ was approximated using the linest quadratic regression tool in excel. $C_{w,t1}$ was found to be 12460 $N/(m/s)$. Hence, the contribution to the total wind coefficient from rotor thrust in this wind regime, can be found by

$$C_{wind,thrust1} = 12460 \cdot \left((\frac{z_{hub}}{10})^{0.12} \right)^2 \tag{9.6}$$

where z_{hub} is the hub height of 119 metres.

Rotor thrust in operational regime above rated (11.4-25 m/s)

The thrust force in this regime is in general difficult to model using quadratic wind coefficients due to the fact that the thrust force decreases for increasing wind speeds. One approach could be to apply a constant force corresponding to the the maximum thrust force at rated wind speed and define negative quadratic wind coefficients. The thrust force could then be written on the form:

$$F_{thrust} = F_{const} + C_{w,t2} \cdot U_{rel,hub}^2 \tag{9.7}$$

where F_{const} corresponds to the maximum thrust force at rated wind speed, $C_{wind,thrust}$ corresponds to a negative quadratic wind coefficient and $U_{hub,rel}$ is the relative wind speed in hub height. The issue with this way of modelling is that a negative damping will occur considering the fact that $U_{hub,rel}$ is the relative wind speed. For a real turbine, the pitch controller will be tuned in order to get maximum power output and at the same time avoid that the motion responses of the structure are too large. The response time of the controller will therefore be specified so it does not contribute to negative damping in for instance pitch. This will not be possible to avoid in the simplified model if the damping is negative. It is therefore concluded that this way of modelling the thrust force should be avoided.

Instead of trying to find a continuous expression for the thrust load, it can be modelled using specified forces and moments in SIMA. The model will then have a constant force applied which is equal to the thrust force as specified in Figure 9.1 for the mean wind speed in

the simulation. The resulting moment caused by the thrust force on the rotor will similarly be included as a constant moment. In order to illustrate, an example with a sea state with 15 m/s mean wind speed in hub height will be considered. The thrust force corresponding to 15 m/s wind speed is found to be 890kN (illustrated in Figure 9.1). This is applied as a constant force acting in the wind direction in SIMA. The moment resulting from the thrust force is simply found as

$$M_{thrust} = F_{thrust} \cdot z_{hub} = 890 \cdot 119 = 105910[kNm] \tag{9.8}$$

This will probably provide a fairly good model for the mean forces and moments caused by the rotor thrust. However, the model does not include any dynamic thrust loads. Note also that this way of modelling the thrust requires the model to be updated for each sea state simulated so the thrust force and resulting moment corresponds to the given mean wind speed in the sea state.

Shutdown condition (above 25 m/s)

When the wind speed is above 25m/s, the turbine is parked with the blades feathered and it will experience very small aerodynamic forces. Nevertheless, it was investigated how large this force is compared to the tower drag in this wind regime. This was done by performing simulations in SIMA. The model used was the example RIFLEX model of a land based turbine included in SIMA, which is modelled to correspond to the 10MW DTU reference turbine. This model was modified so all blades were pitched -90 degrees relative to their initial position to simulate a case were all blades are feathered. Then, a master-slave connection was established between the top of the tower and the rotating shaft in order to fix the turbine. In addition, the induction in the turbine was turned off to avoid use of BEM theory which is not suitable for a parked turbine. The constant wind tests were run for wind speeds of 30m/s and 35m/s.

Since the thrust loads in this case will be due to drag loads on the blades, the thrust on the blades was assumed to follow the function

$$T_{parked} = C_{w,t3} \cdot U_{hub}^2 \tag{9.9}$$

where $C_{w,t3}$ is the wind coefficient for the parked turbine. Based on the constant wind tests, $C_{w,t3}$ was approximated to be 47.0 $N/(m/s)^2$. The total wind coefficient for the parked turbine for a wind reference height of 10 metres can then be found as

$$C_{wind,thrust3} = 47 \cdot \left((\frac{z_{hub}}{10})^{0.12} \right)^2 = 85 \qquad [N/(m/s)^2] \tag{9.10}$$

9.2.4 Total aerodynamic excitation loads

The total quadratic wind coefficients for the different wind regimes are found by superposition of the tower drag and the turbine thrust. The results are summarized in table 9.1. Note that the table only includes the quadratic wind coefficients. For wind speeds between 11.4 and 25 m/s in hub height, the specified force and moment to simulate the thrust must be calculated for the mean wind speed in the sea state.

	Surge			**Pitch**		
Wind regime [m/s]	$C_{w,tower,1}$	$C_{w,rotor,1}$	$C_{w,tot,1}$	$C_{w,tower,5}$	$C_{w,rotor,5}$	$C_{w,tot,5}$
0-11.4	498	22576	23074	33843	2817274	2851117
11.4-25	498	-	-	33843	-	-
25<	498	85	583	33843	10627	44470

Table 9.1: Wind load coefficients. Note that the unit is $[N/(m/s)^2$ for the wind coefficients in surge and $[Nm/(m/s)^2$] for pitch.

It is interesting to compare the thrust force and the tower drag for the lowest and highest wind regime. It is seen that for wind speeds between in hub height between 0 and 11.4 m/s, the thrust loads on the rotor blades is the dominating contribution. On the other hand, the tower drag load is dominating for hub height wind speeds above 25 m/s when the turbine is parked.

9.2.5 Aerodynamic damping

In pitch and roll, the aerodynamic damping provided from tower and rotor is normally important, and for these degrees of freedom the aerodynamic damping will not inherently be included by the quadratic wind coefficients. To account for this, linear damping coefficients should be included in SIMA.

9.2.6 Tower contribution to aerodynamic damping

The aerodynamic damping caused by the tower is found by considering the FWT as a 2-degree of freedom system with motions only in surge and pitch. The total aerodynamic force acting on section k of the tower can be approximated as

$$F_{x,k}(z) \approx \frac{1}{2} \cdot \rho_{air} \cdot C_D \cdot d_k \cdot [U(z_k) - \dot{\theta} \cdot z_k]^2 \tag{9.11}$$

where $\dot{\theta}$ is the pitch rotational velocity of the whole semi body. It is here assumed that $U(z_k) > \dot{\theta} \cdot z_k$ for all tower sections.

Writing equation 9.11 out, the following expression is obtained:

$$F_{x,k}(z) \approx \frac{1}{2} \cdot \rho_{air} \cdot C_D \cdot d_k \cdot [U(z_k)^2 - 2U(z_k)\dot{\theta}z_k + (\dot{\theta} \cdot z_k)^2] \tag{9.12}$$

From this expression it is seen that the damping force acting in the negative x-direction due to the pitch motion is proportional to the wind speed and the pitch rotational velocity. Its absolute value can be written

$$F_{damp,x,k} = \rho_{air} \cdot C_D \cdot d_k \cdot U(z_k)\dot{\theta} \cdot z_k = D_{1,5k}\dot{\theta} \tag{9.13}$$

where $D_{1,5k}$ is the contribution from tower section element number k to the linear damping coefficient in surge due to pitch motion. Similarly as when calculating the tower contribution to the aerodynamic excitation loads, the contribution from each tower section has to be added together in order to get the total tower contribution to the aerodynamic damping. By dividing the tower into 12 sections, each with a $L = 10m$, the following expression for the damping coefficient in surge due to pitch motion is obtained

$$D_{1,5tower} = \sum_{k=1}^{12} \rho_{air} \cdot C_D \cdot d_k \cdot U_{10} \cdot (\frac{z_k}{10})^{0.12} \cdot z_k \tag{9.14}$$

Note that the damping is proportional to the wind velocity U_{10}.

The tower contribution to the damping in pitch due to pitch motion, can then be expressed as

$$D_{5,5tower} = \sum_{k=1}^{12} \rho_{air} \cdot C_D \cdot d_k \cdot U_{10} \cdot (\frac{z_k}{10})^{0.12} \cdot z_k^2 \tag{9.15}$$

9.2.7 Rotor contribution to aerodynamic damping

The damping from the rotor blades will depend on the wind regime the turbine is operating in.

Below rated wind speed (0-11.4 m/s)
The total force in x-direction from the wind on the rotor can be expressed in a similar way as for the tower section element:

$$F_{x,rotor}(z) \approx C_{w,rotor,5} \cdot [U_{10}^2 - 2U_{10}\dot{\theta} \cdot z_{hub} + (\dot{\theta} \cdot z_{hub})^2] \tag{9.16}$$

where $C_{w,rotor,1}$ was established in Chapter 9.2.4.

Following the same procedure as used when calculating the damping from the tower sections, the linear damping coefficient contribution from the rotor in surge due to pitch motion is given by

$$D_{1,5rotor} = 2C_{w,rotor,1}U_{10} \cdot z_{hub} \tag{9.17}$$

The damping coefficient in pitch due to pitch motion is given by

$$D_{5,5rotor} = 2C_{w,rotor,1}U_{10} \cdot z_{hub}^2 \tag{9.18}$$

Operational regime above rated (11.4-25 m/s)
The damping contribution from the rotor in this wind regime will for the real case depend on the blade pitch control system. Since the rotor blades are not included in this model, it

will be difficult to account for this and it was therefore concluded that the damping from the rotor will not be included in the model.

Shutdown condition (above 25 m/s)
The damping due to the rotor in this condition is found similarly as for the wind speeds below rated:

$$D_{1,5rotor} = 2C_{w,rotor,3}U_{10} \cdot z_{hub} \tag{9.19}$$

and

$$D_{5,5rotor} = 2C_{w,rotor,3}U_{10} \cdot z_{hub}^2 \tag{9.20}$$

where $C_{w,rotor,3}$ is equal to 47.0 $N/(m/s)^2$ as established in section 9.1.

9.2.8 Total aerodynamic damping coefficients

Note that for the above described procedure, the aerodynamic damping coefficients have to be updated for each sea state so it corresponds to the mean wind speed in the sea state. This will be an approximation because the wind speed will vary during the sea state.

The damping coefficients for some selected wind speeds are shown in Table 9.2.

U_{119}	$D_{1,5,tower}$	$D_{1,5,rotor}$	$D_{1,5,tot}$	$D_{5,5,tower}$	$D_{5,5,rotor}$	$D_{5,5,tot}$
11.4 m/s	4.15E+05	3.39E+07	3.43E+07	3.26E+07	4.04E+09	4.07E+09
25 m/s	9.04E+05	-	9.04E+05	7.09E+07	-	7.09E+07
39 m/s	1.47E+06	4.49E+05	1.91E+06	1.15E+08	5.35E+07	1.68E+08

Table 9.2: Linear aerodynamic damping coefficients for selected wind speeds. Unit for $D_{1,5}$ is $[Ns]$ while unit for $D_{5,5}$ is $[Nms]$

As seen from the results, the rotor contributes to significant pitch damping for wind speeds close to the rated.

Due to the assumption that the rotor is always facing the wind, we have that $D_{2,4} = D_{1,5}$ and $D_{4,4} = D_{5,5}$.

9.2.9 Challenges using Approach 1 to model the aerodynamic damping

As already mentioned, the damping will vary with the wind speed and hence the damping matrix for the model needs to be updated for each sea state so it corresponds to the mean wind speed of the sea state. Even when this is done, the damping will only correspond to the damping in the mean wind speed and therefore not capture the variations in the aerodynamic damping with varying wind speed within a sea state. The system will therefore be too heavily damped when the wind speed is below the mean wind speed in the sea state and too lightly damped when the wind speed is above the average.

Based on these considerations, it was chosen to find another way to model the tower and rotor.

9.3 Approach 2 to model aerodynamic excitation forces and damping

Instead of using quadratic wind coefficients specified and linear damping coefficients specified on the SIMO body to model aerodynamic excitation loads and damping contributions from the tower and rotor, this approach focuses on using slender elements where possible.

9.3.1 Modelling the tower using slender elements

Modelling the tower using SIMO slender elements is relatively straight-forward. The tower was modelled using 6 slender elements with $C_D = 0.7$. This way of modelling the tower will inherently account for both the excitation forces and the damping.

9.3.2 Modelling the thrust force using slender elements and specified forces

The following approaches were used to model the thrust forces in different wind regimes:

Rotor thrust below rated wind speed (0-11.4 m/s)
The rotor thrust was modelled using a slender element with length of two metres with midpoint 119 metres above the surface. The quadratic wind load coefficient is determined based on the considerations made for the wind coefficients in Approach 1 described in Chapter 9.2.3. Hence, the quadratic wind coefficient for the slender elements simulating the rotor was set to 6230 $N/(m \cdot (m/s)^2)$, which resulted in a total wind coefficient of 12460 $N/(m/s)^2$.

Rotor thrust in operational regime above rated wind speed (11.4-25 m/s)
The rotor thrust in this wind regime, is modelled in the same way as outlined in Approach 1 in Chapter 9.2.3 applying a constant force and resulting moment in order to simulate the thrust load. Similarly to Approach 1, no aerodynamic damping contributions will be included in this model.

Rotor thrust in shutdown conditions (above 25 m/s
The rotor thrust is modelled similarly as for wind speeds below the rated, except that the wind load coefficient used is 23.5 $N/(m \cdot (m/s)^2)$ which resulted in a total wind coefficient of 47 $N/(m/s)^2$ for the slender element simulating the rotor.

9.3.3 Advantages of using Approach 2

One advantage of using Approach 2 compared to using Approach 1 is that Approach 2 is simpler to model considering that the use of slender elements makes both the wind coefficients and the damping coefficients surplus. Hence, there is no need to update any damping matrix for each sea state with different wind speed.

9.4 Wind modelling in SIMA

Turbulent wind files were generated using the version 1.06 of the TurbSim software developed for the National Renewable Energy Laboratory (NREL). TurbSim is based on a statistical model to numerically simulate turbulent wind fields. Further details regarding the theoretical background for TurbSim will not be provided here, references are made to Kelley & Jonkman (2007).

Several spectral models for describing the short term stationary wind conditions are proposed in *DNVGL-RP-C205 Environmental conditions and environmental loads* (2017). From these, the Kaimal model was chosen as basis to generate the turbulent wind time series in TurbSim.

Turbulent wind time series with a length of 11200 seconds where generated for mean wind speeds in the range [1,2,3...45] m/s. For each mean wind speed, 20 different time series where generated based on 20 different random seeds, so in total 900 unique turbulent wind time series were generated. These were used as input both in the simulations used as basis for the short term analyses and the long term analyses.

Chapter 10

SIMA model verification

Some simple tests were performed in order to verify that the SIMA model had the desired abilities.

10.1 Decay tests

Decay tests were performed in surge, heave, pitch and yaw in order to verify that the natural periods of the simplified model corresponded with the natural periods of the full model. This was done by simply applying a constant load in the degree of freedom under investigation and then releasing it at a given time. From the response, the natural periods could be identified. The time series of the decay tests are shown in Figure 10.1 - 10.4.

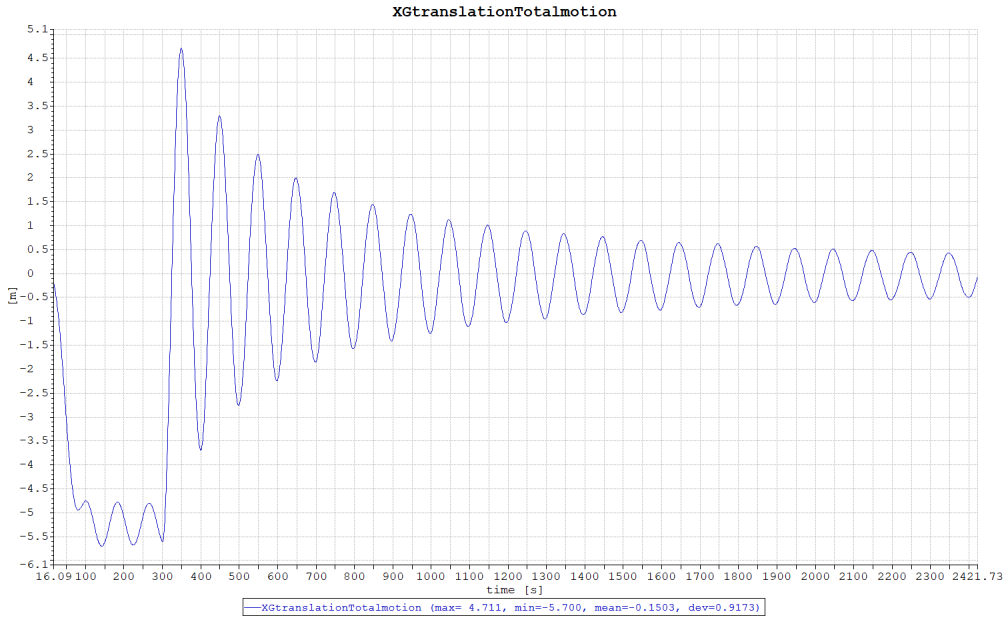

Figure 10.1: Heave decay test time series

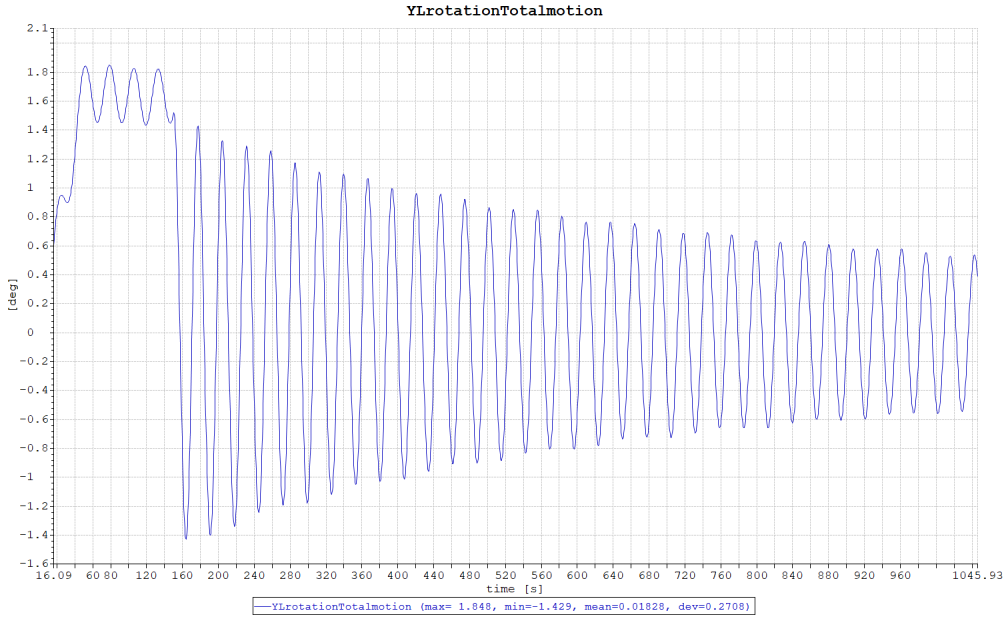

Figure 10.2: Pitch decay test time series

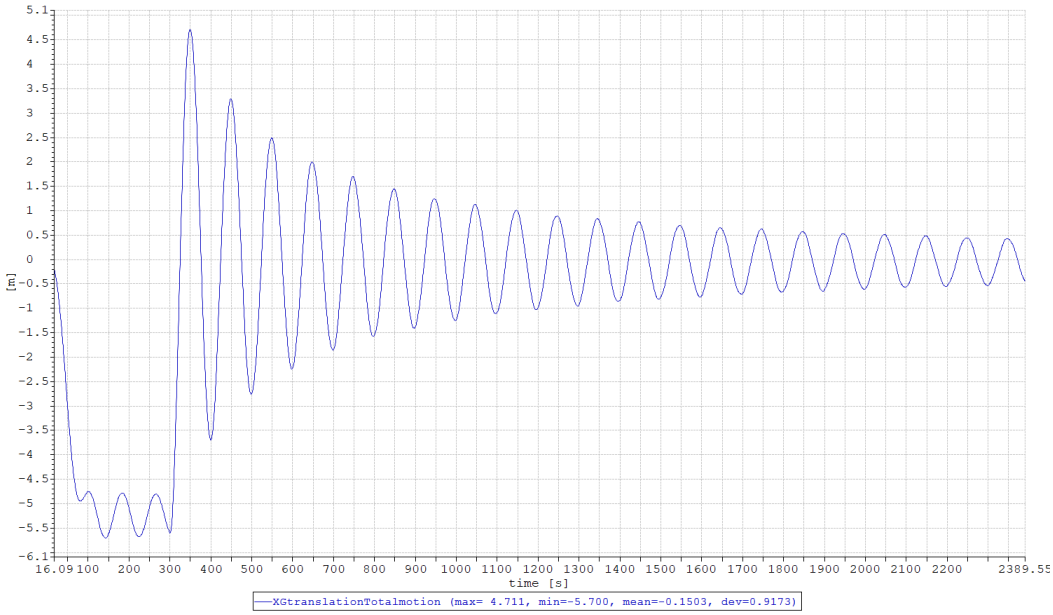

Figure 10.3: Surge decay test time series

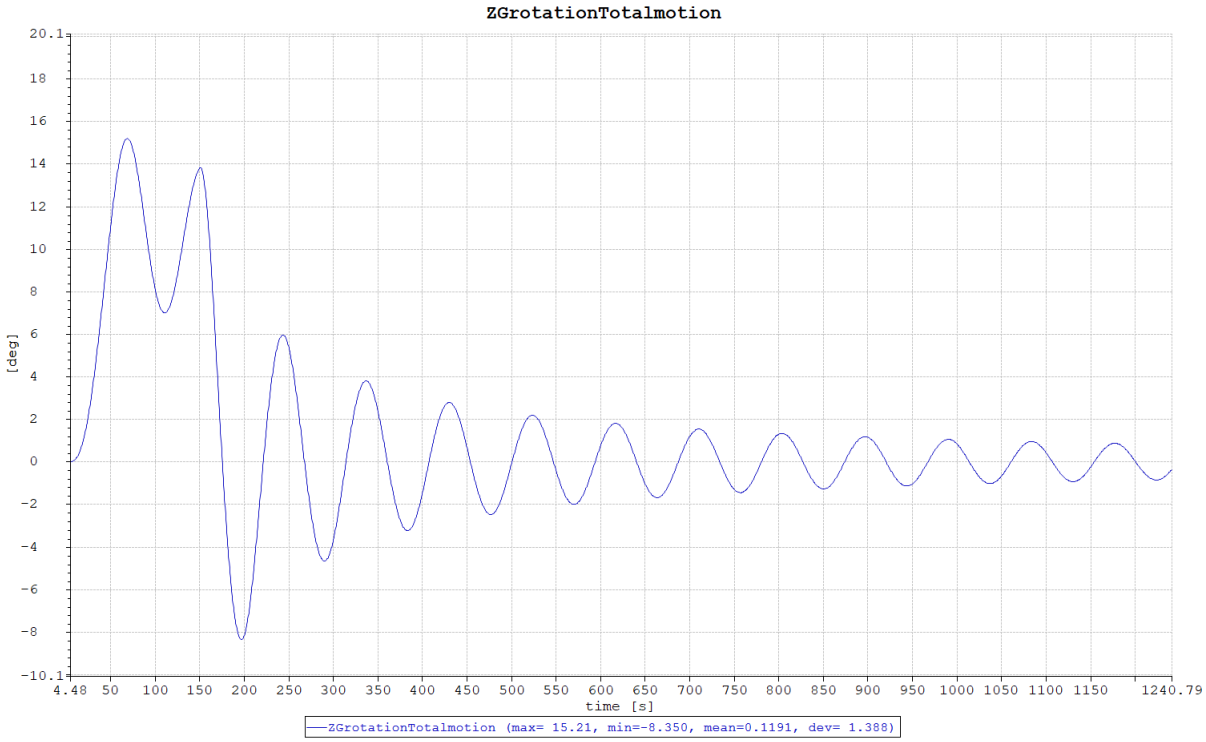

Figure 10.4: Yaw decay test time series

In Table 10.1, the natural periods obtained from the decay tests are compared to those

presented by Wang (2014).

Degree of freedom	**Natural periods simplified model [s]**	**Natural periods, original model (Wang 2014) [s]**
Heave	20.1	20.5
Pitch	27.1	29.5
Surge	99.6	-
Yaw	93.4	-

Table 10.1: Natural periods of the model.

As seen from the table, the results for the simplified and the original model described by Wang (2014) are very similar in heave. In pitch, the natural period of the simplified model is significantly lower than calculated by Wang (2014). This can be partly due to extra stiffness in pitch due to the mooring system and the deviation is considered acceptable. A natural close to 100 seconds in surge is within range expected for this type of floating wind turbine. The natural period in yaw is also considered to be within the desired range.

10.2 Pullout tests

In order to document the mooring system stiffness, pullout tests were performed. Both load directions of 0° and 180° were tested as shown in Figure 10.5 and the relations between restoring force and offset for the two load directions are plotted in Figure 10.6. In addition, the mooring line tension as a function of offset for Line 1 and 2 are plotted in the figure. Note that the offset plotted on the horizontal axis is the absolute value of the offset, so offsets in negative x-direction is still plotted as positive values. This is done to make it easier to compare stiffness for the different load directions.

As expected, the system is significantly stiffer for loading heading in 180° direction than for loading heading in 0 ° direction. This is due to the difference in mooring line orientation for the two directions. While the loading acts in-line for Line 1 for loading acting in 180°, the load with direction 0° acts in-between line 2 and 3. See Figure 10.5 for illustration.

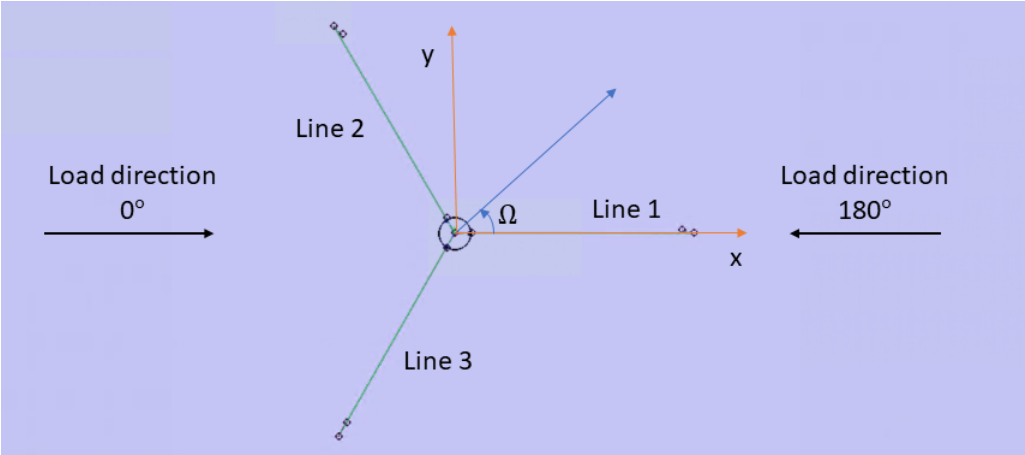

Figure 10.5: Load directions in the pullout test.

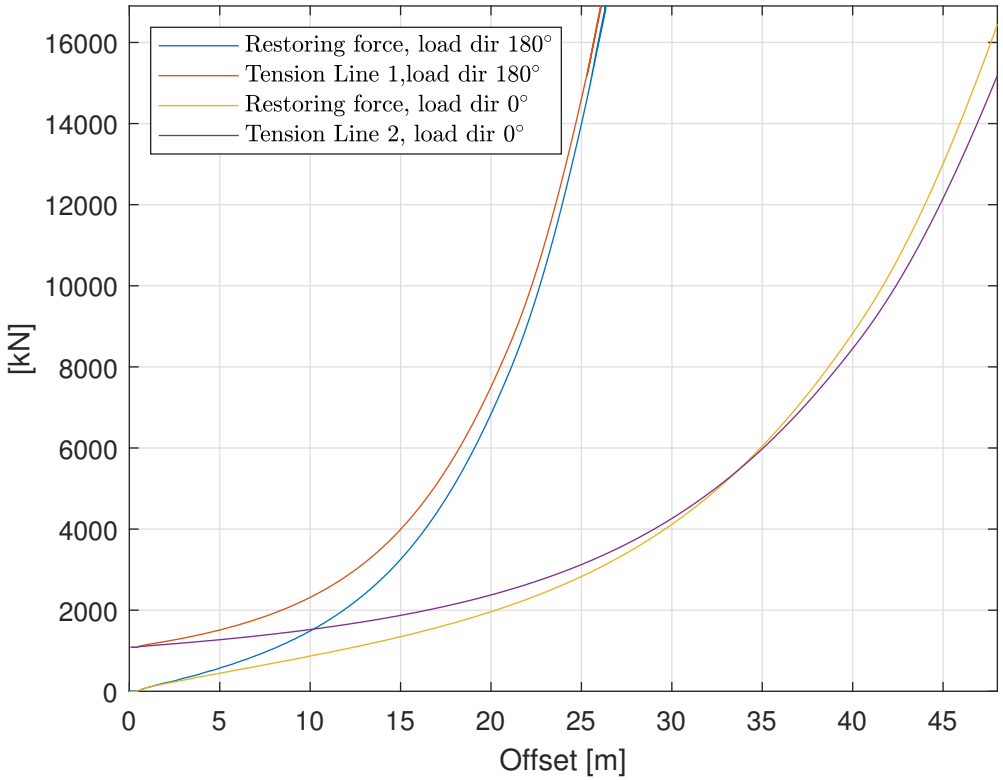

Figure 10.6: System restoring forces and mooring lines tensions as function of offset. Note that the tension will be equal in Line 2 and 3 for the load direction of 0 °, hence only the tension in Line 2 is plotted.

Chapter 11

Traditional short term approach to find design tension

The traditional approach for finding the design tension of the mooring lines was performed according to the procedure outlined in *DNVGL-ST-0119 Floating wind turbine structures* (2018) and *DNVGL-OS-E301: Position mooring* (2015) as described in Chapter 5.

11.1 Contour lines for wind speed and significant wave height

Due to the rotor thrust load, which is highest for hub height wind speed of 11.4 m/s and then decreasing for higher wind speeds, several combinations of wind speed and H_s need to be investigated in order to find the combination resulting in the highest mooring line tension. Hence, contour lines for the combination of wind speeds and significant wave height corresponding to both 50 and 500 year return periods were established. This is consistent with using an All Sea State approach on the metocean data.

In the metocean hindcast data, the wind speed is given as the 1-hour mean wind speed with sample interval 3 hours. It will further be assumed that this wind speed is representative for the mean wind speed in the whole 3 hour sea state.

The joint distribution of wind speed ten metres above sea level, U_{10}, and H_s was then

established. The reference height of 10 metres was chosen to make it eaier to compare the results with the long term wind statistics provided in the Metocean Design Basis, Mathisen et al. (2014). The values of U_{10} found from the contour will later be scaled to 119 m height using the wind profile described in *ISO 19901-1:2015* (2015).

The joint distribution of U_{10} and H_s can be written

$$f_{U_{10},Hs}(u,h) = f_{Hs|U_{10}}(h|u) \cdot f_{U_{10}}(u) \tag{11.1}$$

11.1.1 Establishing the distribution of U_{10}

The distribution of the mean wind speed in a 3 hour sea state is modelled using a 2-paramater Weibull distribution. The cumulative distribution function can be written

$$F_{U_{10}}(u) = 1 - exp\Big(- (\frac{u}{\alpha_u})^{\beta_u}\Big) \tag{11.2}$$

The Weibull parameters are found using the method of moments on all sea states. The results are shown in Table 11.1.

Weibull parameter	**Value**
α_u	9.80
β_u	2.16

Table 11.1: Weibull parameters for 2-parameter Wibull fit to maximum wind speeds.

The resulting cumulative distribution function plotted on Gumbel paper can be seen in Figure 11.1.

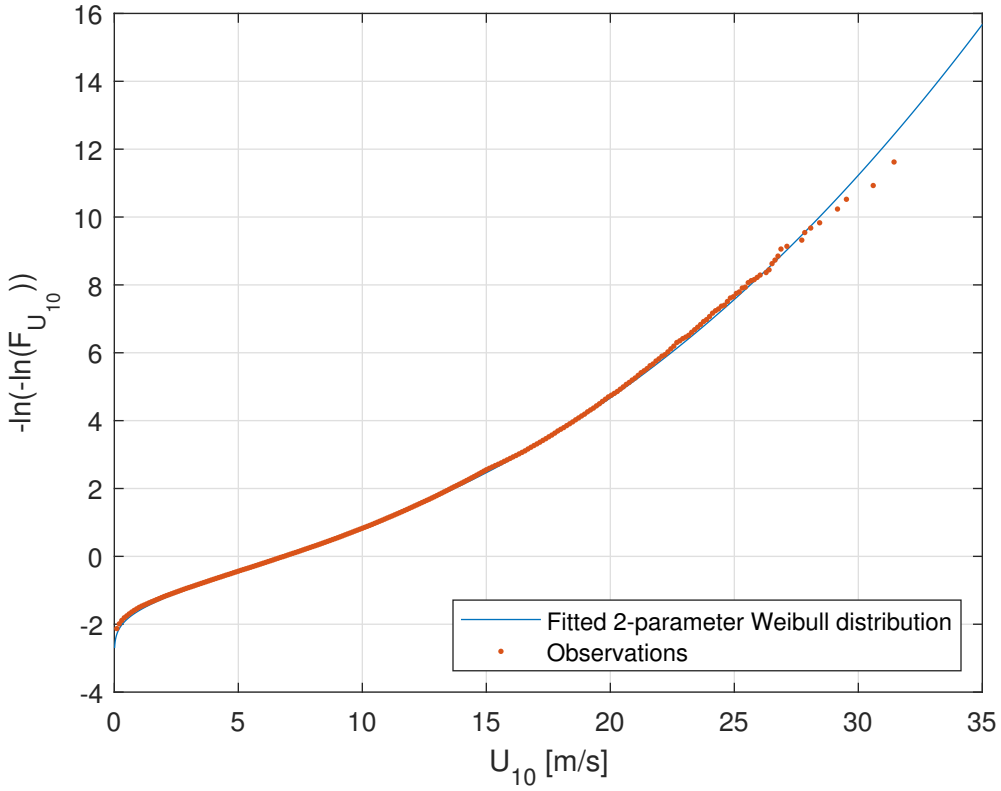

Figure 11.1: Fitted 2-paramater Weibull distribution for U_{10} based on an All Sea States approach.

Although some small deviations are found in the tail behaviour, the 2-parameter Weibull distribituion seems to represent the cumulative distribution of wind speeds sufficiently well.

11.1.2 Establishing the conditional distribution of H_s given U_{10}

Several distributions including lognormal, Weibull and Gumbel distributions were investigated in order to find a suitable distribution function for $F_{Hs|U_{10}}(h|u)$. This was done by dividing the hindcast data for wind and waves into 32 classes based on the wind speed. Class 1 includes all observations of H_s for $U_{10} \leq 1m/s$, class 2 includes the H_s values corresponding to $1 < U_{10} \leq 2m/s$ etc.

The Weibull distribution proved to underestimate the tail behaviour of the distribution of H_s given wind speed. This can be seen from the plots found in Appendix B.

Both the lognormal distribution and Gumbel distribution better describes the conditional distribution for H_s given the wind speed. Plots of the fitted cumulative distribution functions as well as the observations for selected wind classes are shown in Figure 11.2 to 11.4.

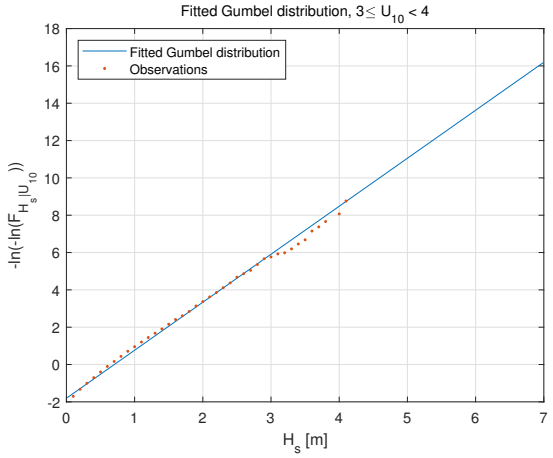

Fitted Gumbel distribution.

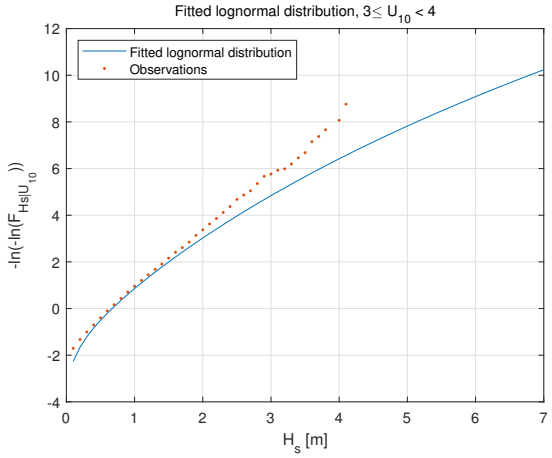

Fitted lognormal distribution.

Figure 11.2: Fitted conditional distributions of Hs for $3 < U_{10} < 4$ m/s

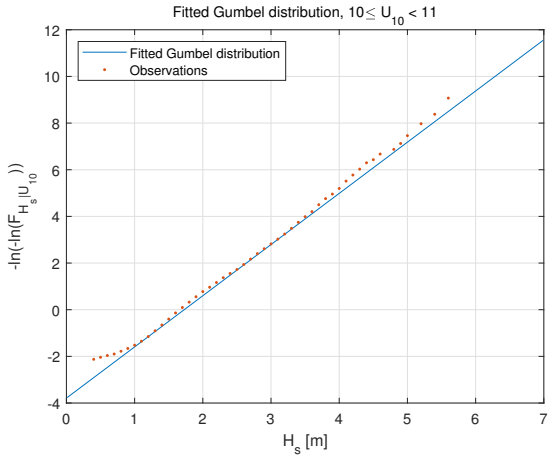

Fitted Gumbel distribution.

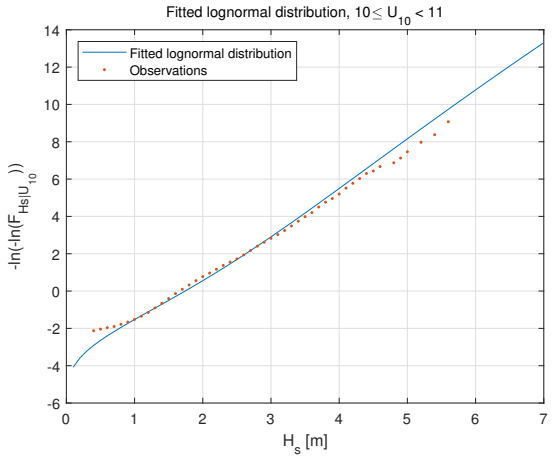

Fitted lognormal distribution.

Figure 11.3: Fitted conditional distributions of Hs for $10 < U_{10} < 11$ m/s

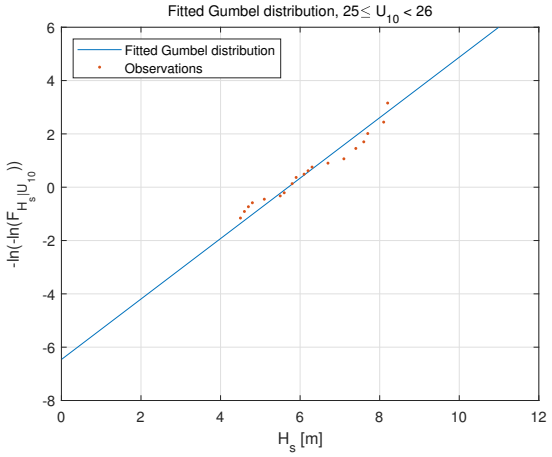

Fitted Gumbel distribution.

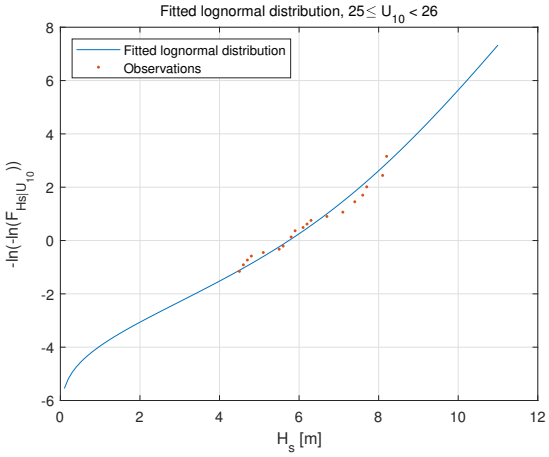

Fitted lognormal distribution.

Figure 11.4: Fitted conditional distributions of Hs for $25 < U_{10} < 26$ m/s

Plots for other wind classes can be found in Appendix B. A qualitative analysis of the plots suggests that both the Gumbel and lognormal distribution could be suitable to describe the conditional distribution of H_s given the wind speed. However, for the lower wind speeds, the lognormal distribution seems to overestimate the H_s. Hence, the Gumbel distribution was chosen to model the conditional distribution of H_s given wind speed. This is based purely on the observations made from the plots.

The conditional distribution of H_s given wind speed can then be written

$$F_{Hs|U_{10}}(h|u) = exp\left(- exp(-\frac{h - \gamma_{Hs|U_{10}}}{\beta_{Hs|U_{10}}}) \right) \tag{11.3}$$

where $\gamma_{Hs|U_{10}}$ and $\beta_{Hs|U_{10}}$ are the Gumbel parameters for the given wind speed.

The Gumbel parameters were calculated for each wind class. Then exponential functions were fitted to each of the Gumbel parameters so each of the parameters became continuous functions of the wind speed. The fit function in MATLAB using an exponential function was used for this purpose. Only wind classes up to 28 m/s were considered. This is due to the fact that above this wind speed each wind class contains so few data points that they provide inaccurate estimations of the Gumbel parameters. Hence, an extrapolation of the estimates found for the lower wind classes is considered a better approximation of the Gumbel parameters in this range. The resulting functions can be viewed in Figure 11.5 and 11.6.

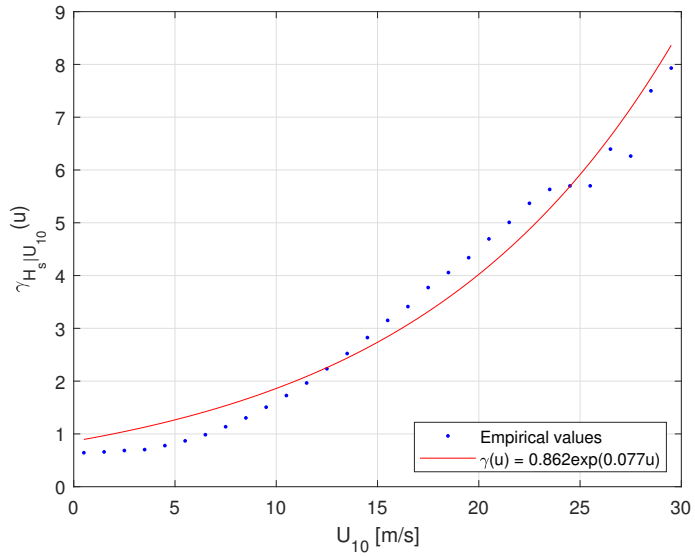

Figure 11.5: $\gamma_{H_s|U_{10}}$ as a function of wind speed.

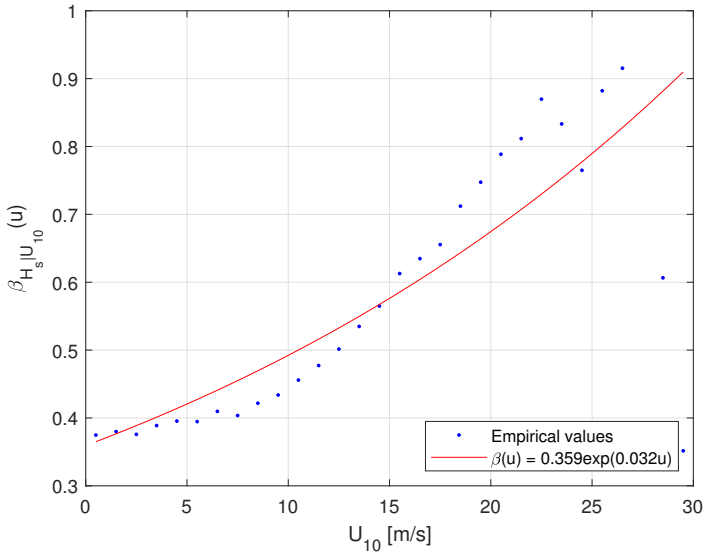

Figure 11.6: $\beta_{H_s|U_{10}}$ as a function of wind speed.

The continuous function of $\gamma_{H_s|U_{10}}$ shown in Figure 11.5 seems to be a good fit to the empirical values. The continuous function of $\beta_{H_s|U_{10}}$ does not entirely capture the trend of the empirical values. However, it is assumed to be sufficiently good.

11.1.3 IFORM method to establish contour lines

A convenient way to establish contour lines with combination of the H_s and wind speed corresponding to different return periods is to transform to problem to the Gaussian space, Haver (2017). This is done using a Rosenblatt transformation. First, the variable z_1 is introduced, so $F_{U_{10}}(u) = \Phi(z_1)$. The variable z_1 is then given explicitly as

$$z_1 = \Phi^{-1}\left[1 - exp\left(\left(-\frac{u_{10}}{\alpha_u}\right)^{\beta_u}\right)\right] \tag{11.4}$$

Similarly, the conditional distribution of Hs given U_{10} can be transformed so $F_{Hs|U_{10}}(h|u) = \Phi(z_2)$. Solving for z_2:

$$z_2 = \Phi^{-1}\left[exp\left(-exp(-\frac{h - \gamma_{Hs|U_{10}}}{\beta_{Hs|U_{10}}})\right)\right] \tag{11.5}$$

The variables z_1 and z_2 will be independent and standard Gaussian distributed, Ross et al. (2018). Hence, the joint probability density function for the variables Z_1 and Z_2 is given by

$$\phi(z_1, z_2) = \phi(z_1)\phi(z_2) = \frac{1}{2\pi}exp\Big(-\frac{1}{2}(z_1^2 + z_2^2)\Big) \tag{11.6}$$

Curves showing constant probability densities can be found simply by setting equation 11.6 equal a constant:

$$\frac{1}{2\pi}exp\Big(-\frac{1}{2}(z_1^2 + z_2^2)\Big) = K \tag{11.7}$$

Solving this equation with respect to z_1 and z_2 gives

$$z_1 + z_2 = -2ln(2\pi K) \tag{11.8}$$

From equation 11.8, it is seen that the curves representing constant probability density will have circular shapes. This is an important feature because it means that the probability

of being outside a tangent line to any point on curve will also be constant along the contour in the Gaussian space. Hence, the circular contours in the Gaussian space do not only show constant probability densities, they will also correspond to a constant probability of exceedance.

A contour line with radius c can be defined in the Gaussian space as

$$z_1^2 + z_2^2 = c^2 \tag{11.9}$$

The probability of being outside a tangent to this contour line is then given by

$$p_c = 1 - \Phi(c) = -\Phi(c) \tag{11.10}$$

Since each sea state is assumed to last for 3 hours, the the value of p_c is the exceedance probability per 3 hour. The value of p_c corresponding to a 50 year return period can then be found as

$$p_c = \frac{2 \cdot 10^{-2}}{2920} = 6.8493 \cdot 10^{-6} \tag{11.11}$$

where 2920 is the number of 3 hour sea states occurring in a year.

The radius of the contour line in the Gaussian space can then be found by solving equation 11.10 with respect to c:

$$c_{0.02} = -\Phi^{-1}(6.8493 \cdot 10^{-6}) = 4.3486 \tag{11.12}$$

Using this approach, contour lines corresponding to 1 year, 50 year and 500 year return periods were established in the Gaussian space. The contour lines were then transformed to the physical space. The transformation of the wind speed, u, is deduced from equation 11.4 and becomes:

$$u = -\alpha_u [ln(1 - \Phi(z_1))]^{1/\beta_u} \tag{11.13}$$

Similarly, the significant wave height is found by rearranging equation 11.5:

$$h = -\beta_{Hs|U_{10}} \cdot ln[-ln(\Phi(z_2))] + \gamma_{Hs|U_{10}} \tag{11.14}$$

The resulting contour lines corresponding to 1, 50 and 500 year return period are plotted together with the hindcast data. The result is shown in Figure 11.7.

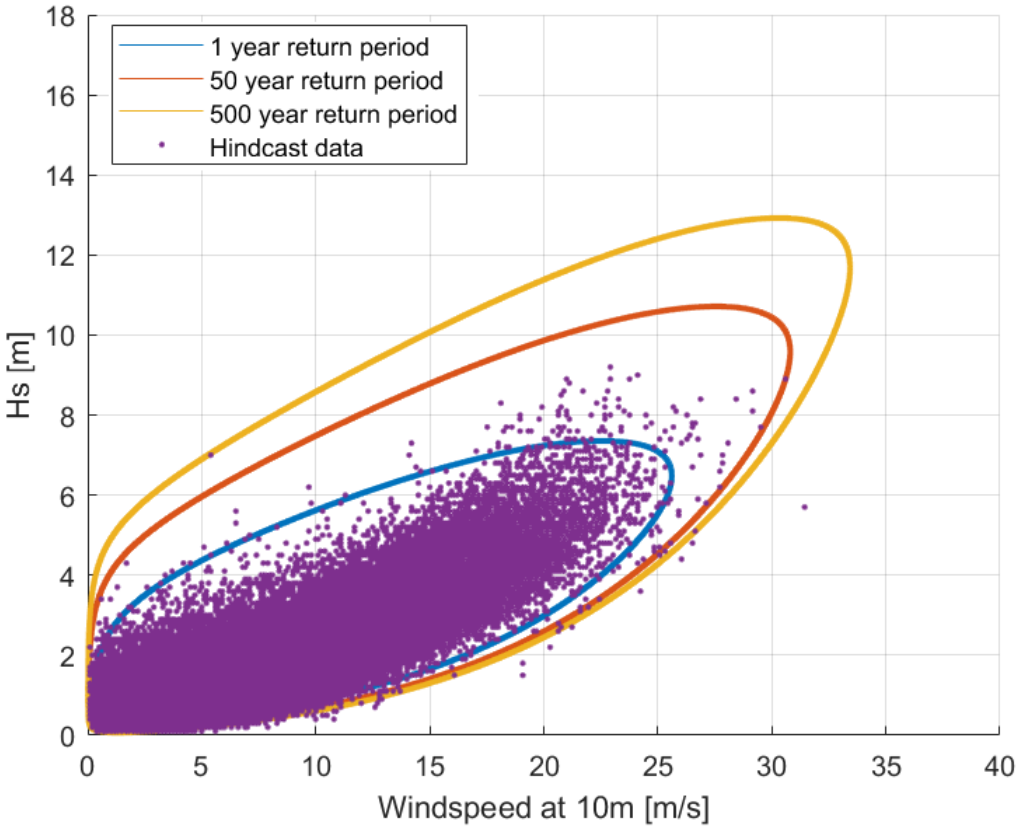

Figure 11.7: Contour plot for combinations of wind speed and Hs corresponding to 1 year return period, as well as ULS and ALS return periods.

11.1.4 Discussion of contour line results

Moving along the contour corresponding to 50 year return period, the maximum wind speed found was 30.8 m/s. This is very similar to the results from the POT analysis described in Chapter 7.4. The largest H_s value found along the 50 year contour is 10.7 m. This is

significantly larger than the value found using the POT approach described in Chapter 7.3.2 where the H_s corresponding to 50 year return period was found to be 9.9m when using a fitted Weibull distribution to calculate the H_s corresponding to 50 year return period. However, this is expected due to the fact that the contour line approach is consistent with using an All Sea States approach and the results are hence expected to be more conservative since it neglects correlation between successive sea states, Haver (2017). Comparing the 50 year return period H_s found from the contour lines to that given in the Hywind Scotland Metocean Design Basis where the 50 year return period H_s is found by using an All Sea States approach, the results only deviates with 0.2 m. The comparison of results is summarized in Table 11.2.

Characteristic corresponding to 50 year return period	**From contour line**	**Using a POT approach to fit Weibull distributions**	**Metocean design basis**
U_{10} [m/s]	30.8	30.6	31.0
H_s [m]	10.7	9.9	10.5

Table 11.2: Comparison of U_{10} and H_s values corresponding to 50 year return period.

11.2 Input conditions for ULS analysis

Four different points along the 50 year contour line for wind and H_s were investigated in order to find the combination of wind speed and H_s resulting in the highest mooring line tension. These are shown in Figure 11.8.

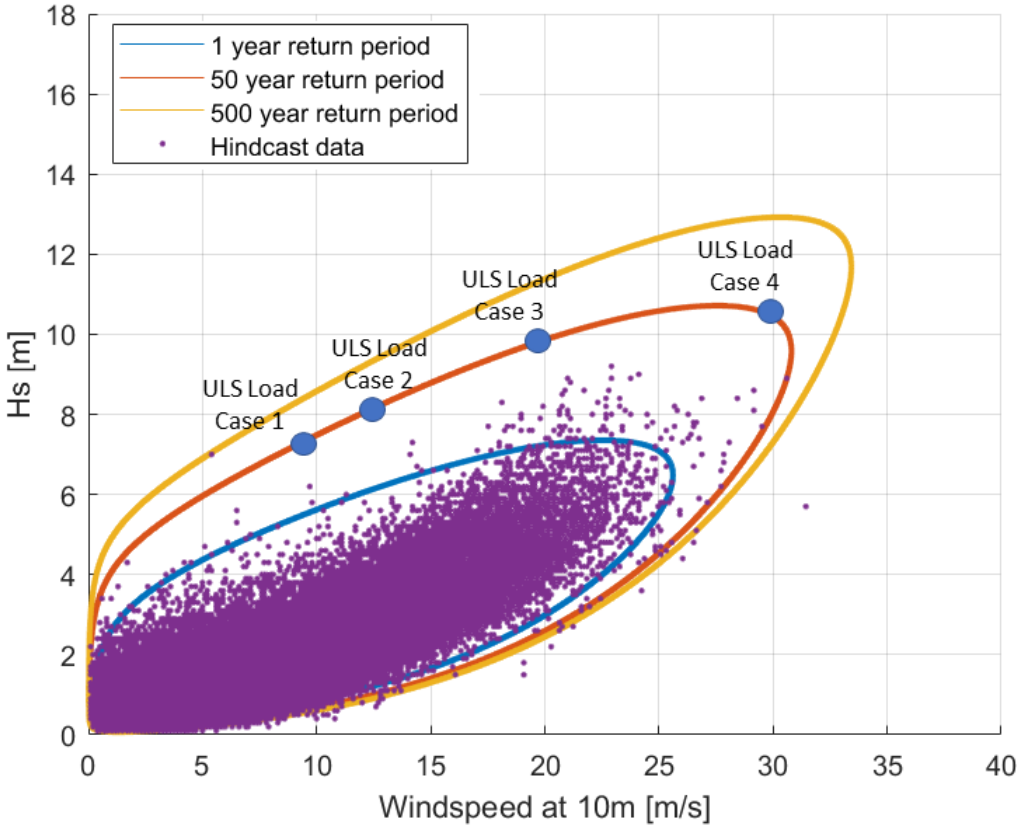

Figure 11.8: ULS load cases.

The contour line established is only 2-dimensional and did not include T_P. For simplicity, the T_p used in the short term analyses was assumed to be a function of the H_s as given in the Hywind Metocean Design Basis, Mathisen et al. (2014) and illustrated in Figure 11.9.

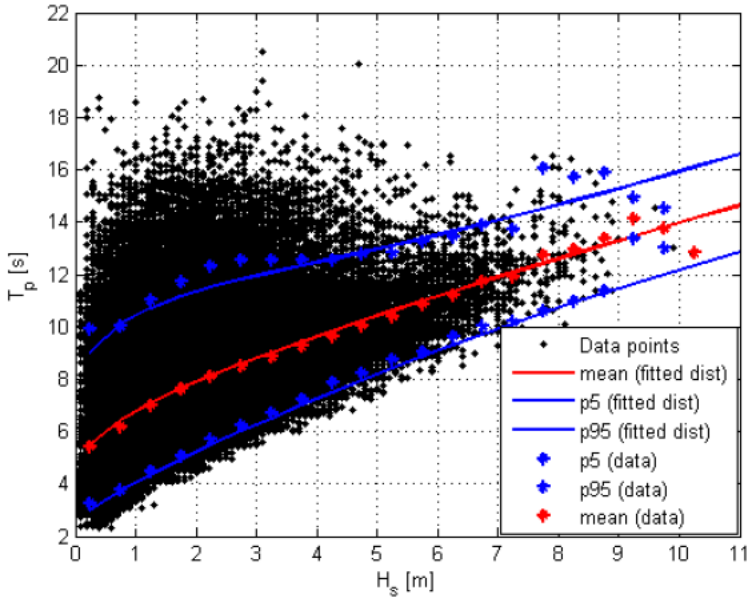

Figure 11.9: T_P for given H_s as given in Mathisen et al. (2014).

The short term analyses were first performed for the mean T_P. Sensitivity of the T_P to the design tension for the mooring lines is investigated in Chapter 11.5.

For each load case 20 three hour time domain simulations were performed in SIMA using different random seeds to generate waves and turbulent wind time series.

The environmental data specified for each load case are summarized in table 11.3. Both wind, waves and current are acting with a heading of 180 degrees. This is in-line with mooring line 1 and is assumed to be the most critical heading direction.

ULS Load Case	**Wind at 10 m [m/s]**	**Wind in hub height [m/s]**	**Hs [m]**	**Tp [s]**	**Current [m/s]**	**Heading [deg]**
1	9.2	11	7.3	12.1	1.7	180
2	12.3	15	8.1	12.7	1.7	180
3	19.8	25	9.8	13.9	1.7	180
4	29.8	39	10.7	14.4	1.7	180

Table 11.3: Environmental data for each load case in the short term analysis.

11.3 Results of ULS analysis

Based on the results from the time domain analyses, the design tension for each sea state could be established based on the mean tension and maximum dynamic tension as described in Chapter 5.2.1. The results are summarized in Table 11.4 which shows the characteristic mean tension, $T_{c,mean}$, characteristic dynamic tension, $T_{c,dyn}$, characteristic tension T_c, the design tension T_d and the utilization factor found based on the simulations of each load case. $T_{c,mean}$, $T_{c,dyn}$, T_c and T_d are explained in Chapter 5.2. The utilization factor is defined as

$$u_f = \frac{T_d}{S_c} \tag{11.15}$$

where S_c is the characteristic capacity. The characteristic capacity is $0.95 \cdot S_{mbs}$, where S_{mbs} is the maximum breaking strength of the mooring line given as 21179 kN for the 147 mm chain mooring line considered, *Ramnäs Bruk Product Catalogue* (2015). Hence, the characteristic capacity each mooring line will be 20120 kN.

ULS Load Case	$T_{c,mean}$ **[kN]**	$T_{c,dyn}$ **[kN]**	T_c **[kN]**	T_d **[kN]**	**Utilization factor**
1	4363	3558	7921	11899	0.59
2	3851	4017	7868	12036	0.60
3	3792	5888	9680	15234	0.76
4	3695	6782	10477	16673	0.83

Table 11.4: Results of short term analysis.

The dimensioning load case is Load Case 4 which is the condition with the largest H_s and largest wind speed. The design tension is found to be 16673 kN. With the selected mooring line dimensions and chain quality, this results in a utilization factor of 0.83.

Some interesting observations can be be made by comparing the mean tension and dynamic tension for each load case. It is seen that the mean tension is largest for Load Case 1 and then decreasing for the load cases with higher wind velocities. This is expected due to the fact that the wind thrust load will decrease for the increasing wind velocities over 11.4 m/s. The dynamic tension is as expected increasing for the increasing H_s. These trends are illustrated in the time series presented in Chapter 11.3.1.

The results suggest that the highest mooring line tension occurs for the sea states where the H_s is largest. This indicates that the mooring line tension is more sensitive to wave loads than wind loads. This is in good agreement with the findings of Xu et al. (2018) when investigating effect of hydrodynamic loads on a CSC substructure designed to support a 5 MW wind turbine.

11.3.1 Time series for mooring line tension and horizontal offset

In order to get a better description of the dynamic behaviour of the mooring line tension, time series of the mooring line tension in mooring line 1 are plotted for one simulation for each of ULS Load Case 1-4. In addition, the plots for surge motion of the FWT are included for each load case. Time series for heave and pitch motions are included in Appendix C.

The time series illustrate the same trend as observed in Table 11.4, that both the mean offset and the mean tension is largest for Load Case 1 and decreasing for increasing wind speeds. At the same time, it is seen that the dynamic tensions is largest for Load Case 4 and decreasing for the lower load cases. The frequency content in the time series will be discussed in Chapter 11.3.2.

Note that due to the loading direction, the offset for all load cases is in negative x-direction.

ULS Load Case 1

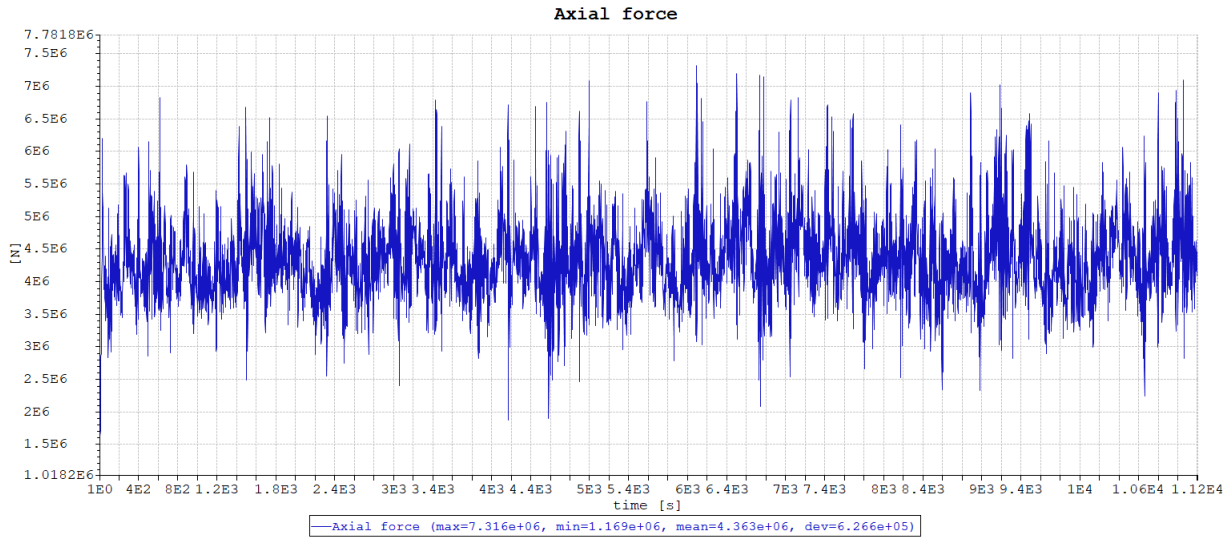

Figure 11.10: Time series of tension in mooring line 1.

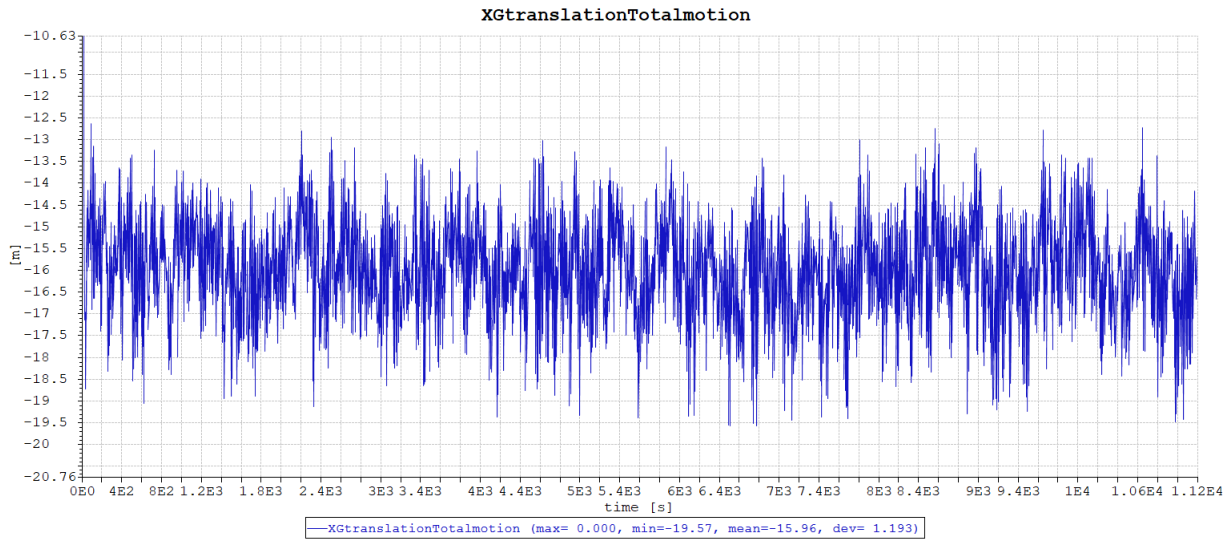

Figure 11.11: Time series of surge motion of the FWT.

ULS Load Case 2

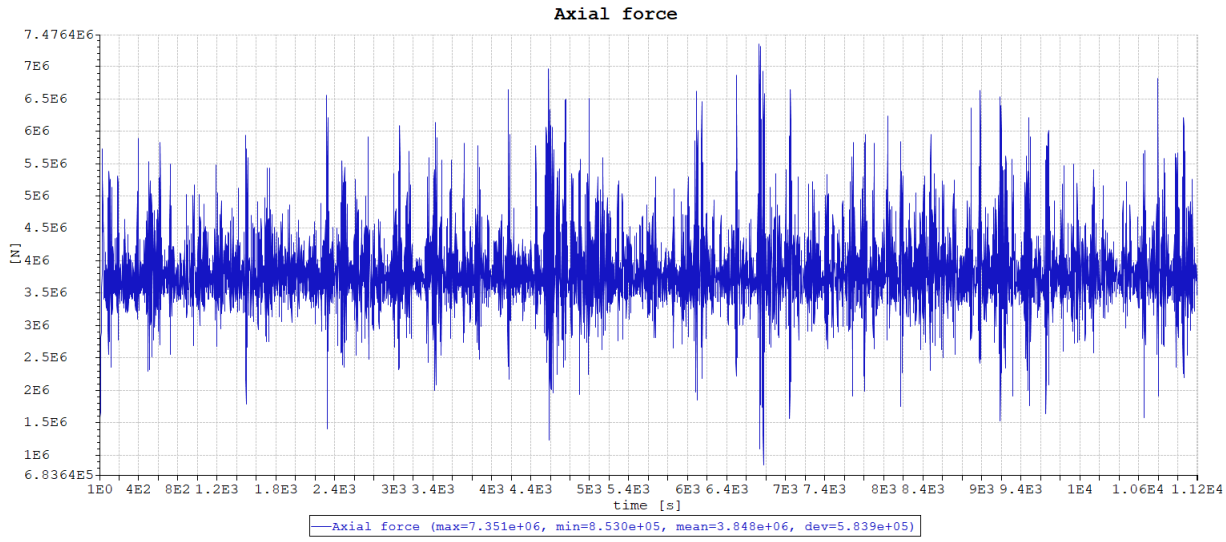

Figure 11.12: Time series of tension in mooring line 1.

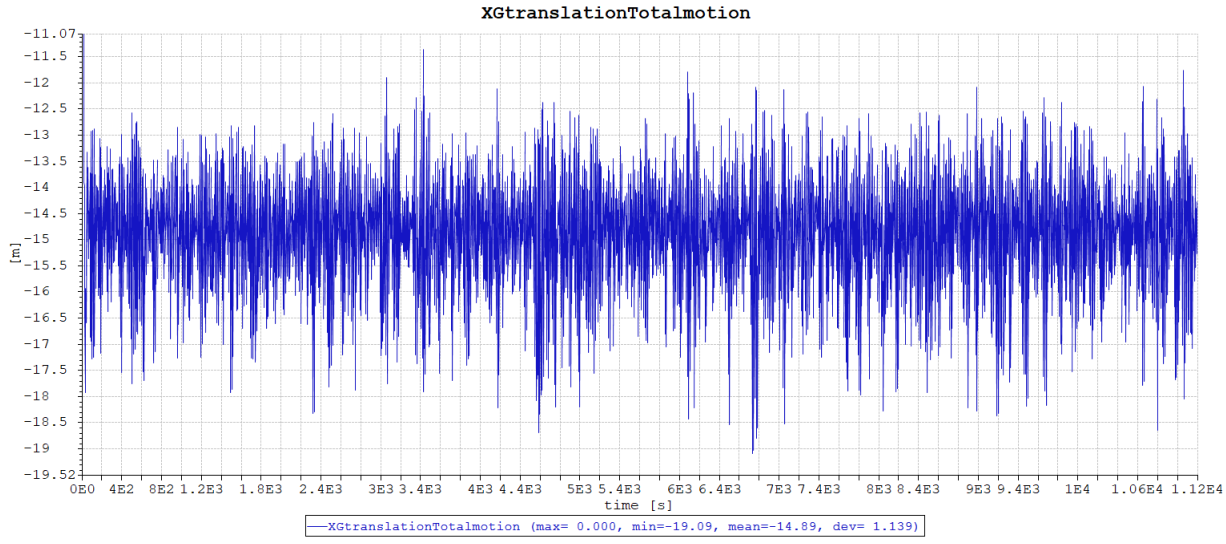

Figure 11.13: Time series of surge motion of the FWT.

ULS Load Case 3

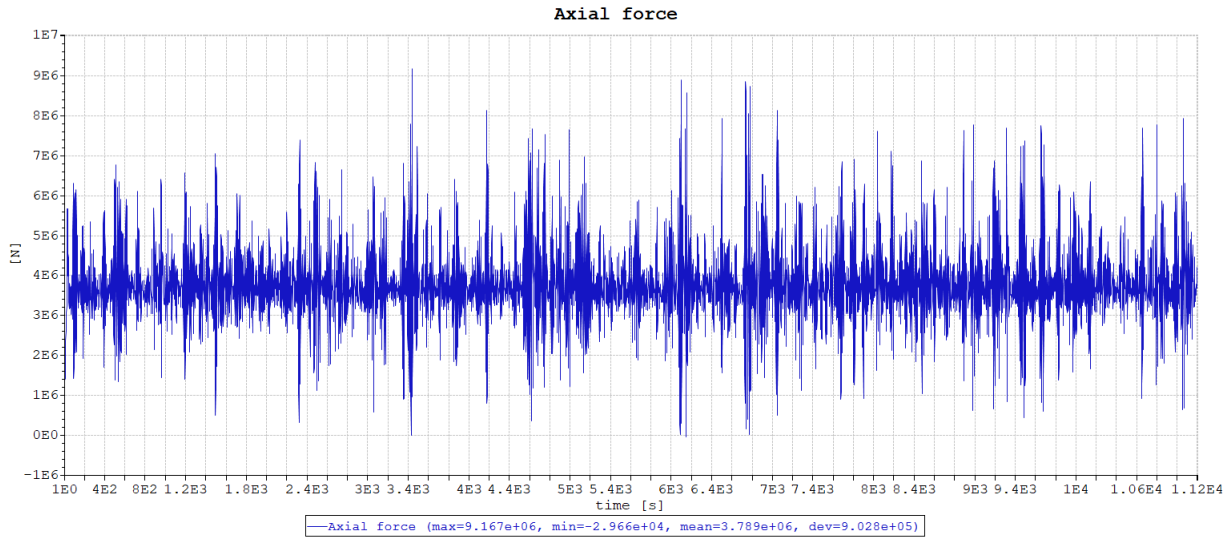

Figure 11.14: Time series of tension in mooring line 1.

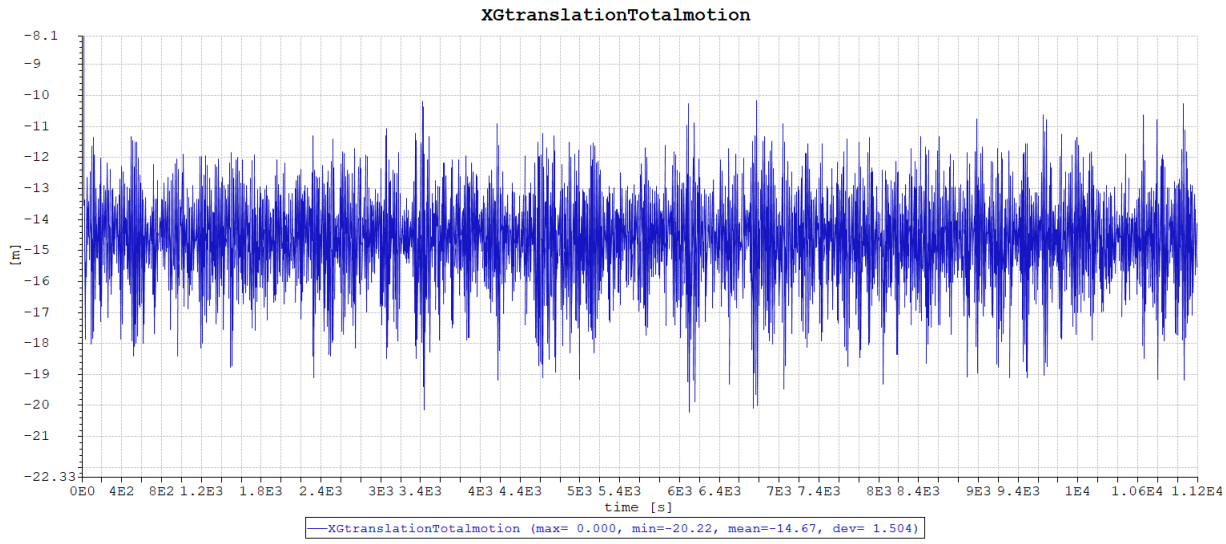

Figure 11.15: Time series of surge motion of the FWT.

ULS Load Case 4

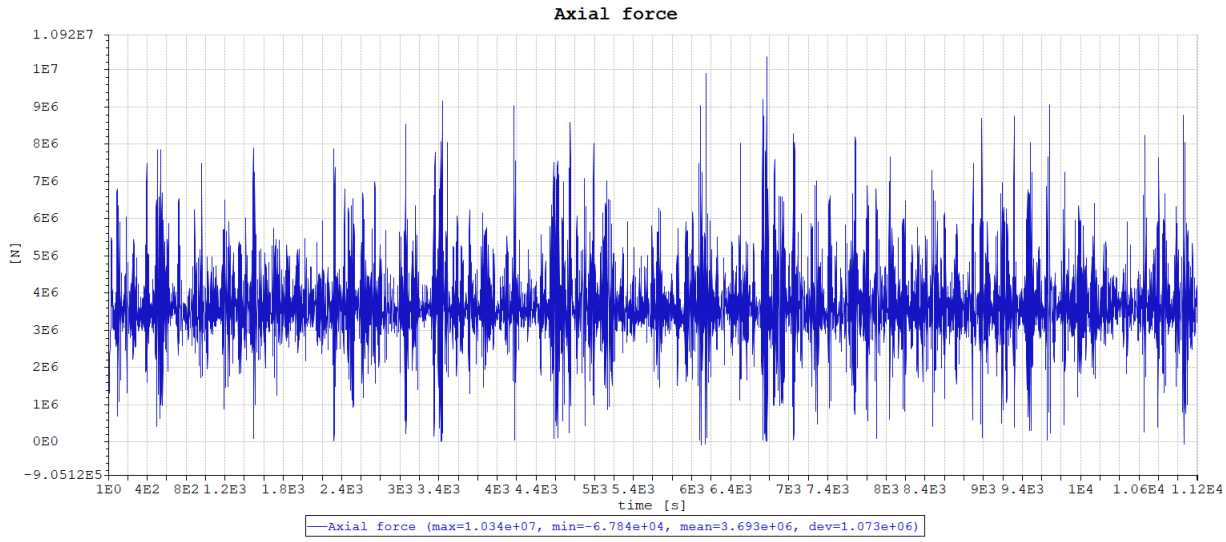

Figure 11.16: Time series of tension in mooring line 1.

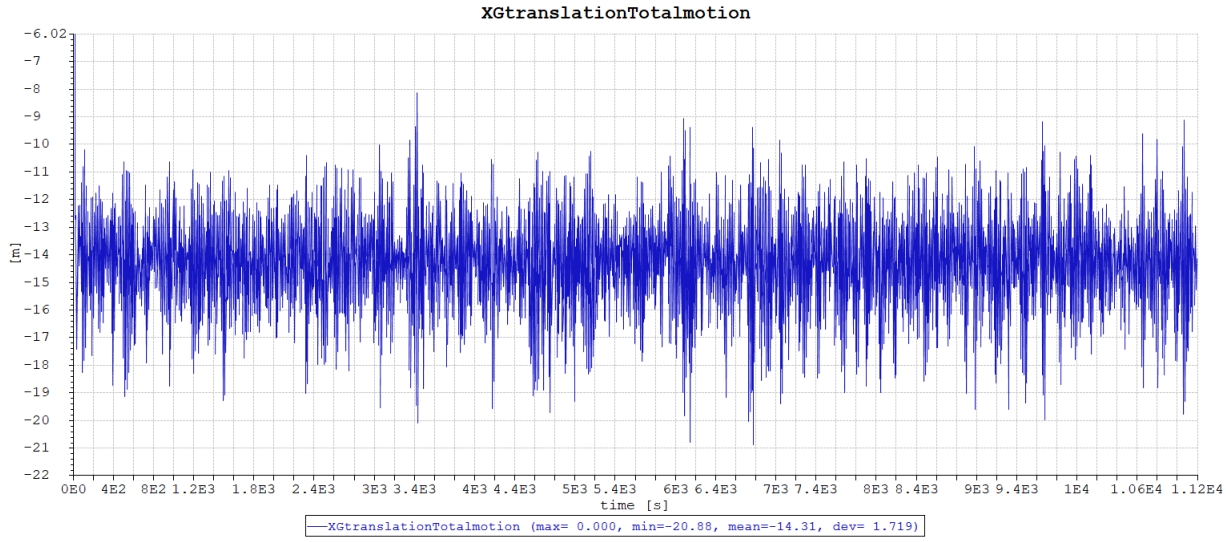

Figure 11.17: Time series of surge motion of the FWT.

11.3.2 Frequency content of mooring line response

It is of interest to get an indication on which frequency ranges that are dominating for the force in the mooring lines. Hence, time series from the simulations of Load Case 1-4 were

Fourier transformed in order to get the mooring line load spectra. The results can be seen in Figure 11.18.

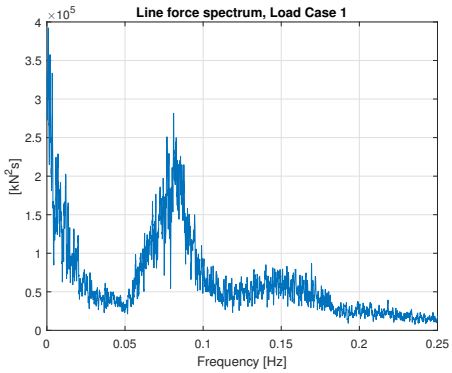

Line force spectrum, Load Case 1.

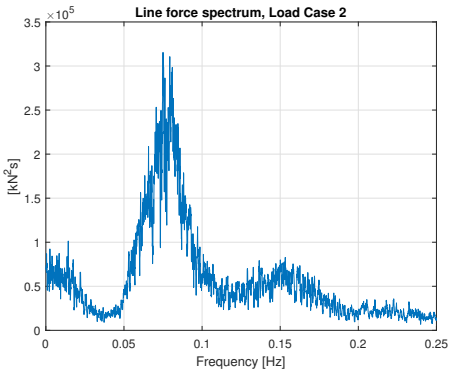

Line force spectrum, Load Case 2.

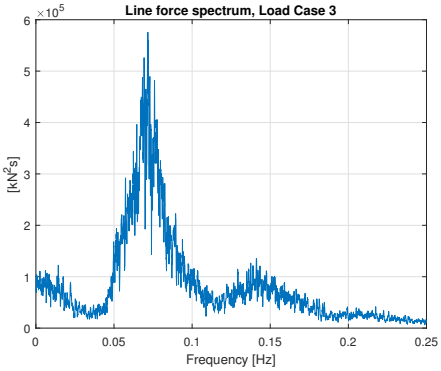

Line force spectrum, Load Case 3.

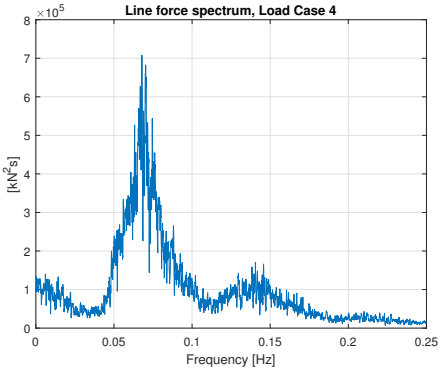

Line force spectrum, Load Case 4.

Figure 11.18: Line force spectra for all four load cases.

None of the models have second order wave drift coefficients included, so the low frequency motions of the body will be dictated mainly by wind loads. The spectra for Load Case 1 has significant content both in the wave frequency range (around the peak frequency of 0.08Hz) and also in the low-frequent range corresponding to the frequency ranges with the highest energy content in the wind spectra. This is as expected, considering that the model has slender elements simulating the effect of a rotor which results in large thrust forces from the wind. This can also be observed from the time series illustrated in Figure 11.10 and 11.11

where it is seen that low-frequency response is a significant part of both the surge motion and the resulting mooring line tension.

For Load Case 2 and 3, the force in the mooring line is dominated by components in the wave frequency range. This is expected, considering that these models only have a constant force and moment applied in order to simulate the effect of the thrust on the rotor. Therefore, the loading from the applied wind will only come from drag on tower and columns above the free water surface. These will be very small compared to the thrust loads on the rotor and the peaks are hence small compared to those located in the wave-frequency range. This can also be seen from the time series in Figures 11.12-11.15 where the response seems to be mainly consisting of wave frequency components.

Load case 4 has a qualitatively very similar line force spectra to those of Load Case 2 and 3. The largest difference is that the peaks in the wave frequency range is larger than for Load Case 2 and 3. This is expected, considering that the H_s is larger for this case and larger wave loads will hence be induced.

11.4 Sensitivity of environmental loading direction

As mentioned in Chapter 11.2, the least favorable direction for the heading of wind, waves and current was assumed to be in-line with mooring line 1. In order to investigate the response sensitivity to environmental loading heading direction, analyses were run also for the case with environmental loads heading in-between the mooring lines. This corresponds to wind, waves and current with heading 0°. The additional ULS load cases investigated are summarized in Table 11.5. Note that the only difference from ULS Load Case 1-4 is the direction of the environmental loads.

ULS Load Case	Wind at 10 m [m/s]	Wind in hub height [m/s]	Hs [m]	Tp [s]	Current [m/s]	Heading [deg]
5	9.2	11.0	7.3	12.1	1.7	0
6	12.3	15.0	8.1	12.7	1.7	0
7	19.8	25.0	9.8	13.9	1.7	0
8	29.8	39.0	10.7	14.4	1.7	0

Table 11.5: Additional ULS load cases investigated to check directional dependency of environmental loads to mooring line tension.

The resulting tension for Load Case 5-8 found in mooring line 3, where the highest tension occurred, are shown in Table 11.6. As seen from the results, environmental loading heading in-between mooring lines is less critical for the mooring system than environmental loading in-line. This is expected considering the mooring system properties documented in Chapter 10.2.

ULS Load Case	$T_{c,mean}$ [kN]	$T_{c,dyn}$ [kN]	T_c [kN]	T_d [kN]	Utilization factor
5	3902	2046	5949	8654	0.43
6	3415	1785	5200	7563	0.38
7	3345	2472	5817	8674	0.43
8	3246	2779	6025	9083	0.45

Table 11.6: Results of analysis of ULS Load Case 5-8.

11.5 Sensitivity of peak period to mooring line tension

In order to investigate how changes in peak period of the wave spectra affects the line tensions, each of ULS load cases 1-4 were also simulated using the upper and lower limit of the 90% confidence band for T_P illustrated in Figure 11.9. The T_P corresponding to the lower limit (p5) and upper limit (p95) of the 90% confidence band are shown in Table 11.7.

Corresponding ULS Load Case	Wind speed in hub height [m/s]	Hs [m]	Tp [s]			Current [m/s]
			p5	Mean	p95	
1	11.0	7.3	10.1	12.1	14.3	1.7
2	15.0	8.1	10.8	12.7	14.7	1.7
3	25.0	9.8	12.1	13.9	15.8	1.7
4	39.0	10.7	12.6	14.4	16.4	1.7

Table 11.7: T_P values used as input in the sensitivity analysis of T_P to mooring line tension.

The resulting mooring line tensions found from the analysis of the load cases using peak periods corresponding to the lower limit (p5), mean and upper limit (p95) of the 90% confidence band of T_P are summarized in Table 11.8.

Corresponding ULS Load Case	Resulting tensions [kN]									Relative difference in design tension from mean T_p to p95
	p5			Mean			p95			
	$T_{c,mean}$	$T_{c,dyn}$	T_d	$T_{c,mean}$	$T_{c,dyn}$	T_d	$T_{c,mean}$	$T_{c,dyn}$	T_d	
1	4398	3239	11386	4363	3558	11899	4329	3947	12534	5.34%
2	3892	3402	11013	3851	4017	12036	3814	4492	12820	6.52%
3	3842	5208	14108	3792	5888	15234	3752	6013	15400	1.09%
4	3749	6310	15916	3695	6782	16673	3653	6645	16379	-1.76%

Table 11.8: Resulting tensions found from the T_P sensitivity study.

For Load Case 1-3, the design tension increases with increasing peak period. For Load Case 4, the design tension increases from the simulations with T_P corresponding to p5 to the analysis with T_P corresponding to the mean. However, the design tension in Load Case 4 decreases slightly when going from the T_P corresponding to the mean value to the T_P corresponding to p95. Hence, the original estimate for the design tension found through simulations using mean T_P from the Metocean Design Basis will be taken as the ULS design tension since it is the most conservative estimate.

11.6 Check of ALS environmental load cases

Even though this thesis focuses on ULS design, it is also of interest to check the ALS criteria in the case this could provide more conservative results than the ULS criteria. As described in Chapter 5, one of the ALS cases defined in *DNVGL-ST-0119 Floating wind turbine structures* (2018) is failure of one mooring line with the presence of 50 year return period environmental loads. Since the mooring system only consists of 3 mooring lines, it is assumed that this will

not be a critical load case. If a line fails, this will lead large offsets resulting in a ruptured power cable, but as long as the mooring lines are able to rotate around their anchor connections, they will in this condition experience smaller loads than for the same environmental loads acting in-line with one mooring line. Hence, this ALS criteria is not investigated further.

However, the ALS load cases also includes abnormal environmental loads. According to *DNVGL-ST-0119 Floating wind turbine structures* (2018), that is environmental loads with return period 500 years. Here, this is taken as the load combination of H_s corresponding to 500 year return period, wind speed corresponding to 50 year return period and current speed corresponding to 10 year return period. This is consistent with an ALS load combination defined in *NORSOK N-003:2017* (2017).

Four load cases were investigated an these are summarized in Table 11.9. These are also shown in the contour lines in Figure 11.19. Both wind, waves and current have heading in 180° direction since this proved to be most unfavorable direction in the ULS analysis. Hence, the ALS load cases corresponds to ULS Load Case 1-4, but with H_s corresponding to 500 year return period instead of 50 year.

ALS Load Case	**Wind at 10m [m/s]**	**Wind in hub height [m/s]**	**Hs [m]**	**Tp [s]**	**Current [m/s]**
1	9.2	11.0	8.3	12.8	1.7
2	12.3	15.0	9.3	13.5	1.7
3	19.8	25.0	11.3	14.8	1.7
4	29.8	39.0	12.9	15.7	1.7

Table 11.9: ALS environmental load cases.

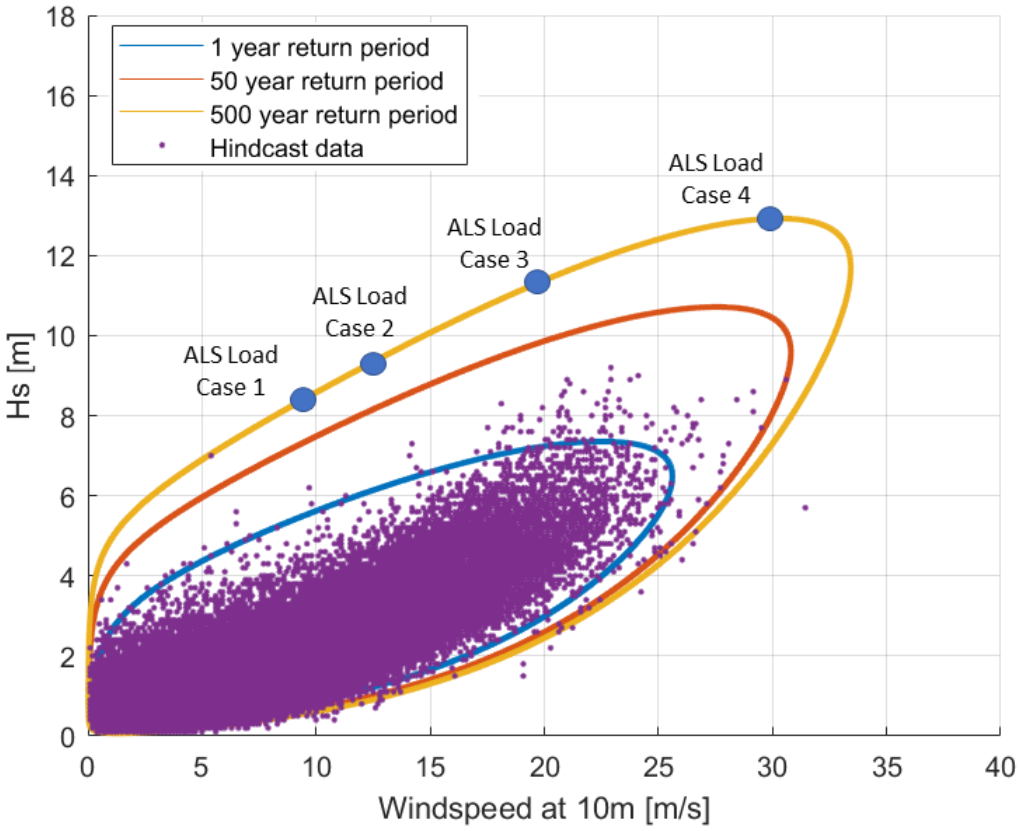

Figure 11.19: ALS Load cases.

The results of the analyses are shown in Table 11.10.

ALS Load Case	$T_{c,mean}$ **[kN]**	$T_{c,dyn}$ **[kN]**	T_c **[kN]**	T_d **[kN]**	**Utilization factor**
1	4394	4630	9024	9487	0.47
2	3888	5337	9225	9759	0.49
3	3842	7336	11178	11911	0.59
4	3846	8848	12694	13578	0.67

Table 11.10: Results of ALS analysis.

The characteristic tensions were found using the same procedure as for the ULS load cases and as expected they are higher compared to the T_c corresponding ULS load cases. The partial safety factors used for the ALS case are smaller ($\gamma_{mean} = 1.0$ and $\gamma_{dyn} = 1.10$) than

the ULS safety factors. This resulted in smaller design tension, T_d, for all ALS load cases compared to the corresponding ULS load cases. Hence, the ALS criterion is not governing and ULS criterion will be the dimensioning criterion (not taking the fatigue limit state into account). This result was expected considering that the H_s was increased only from 50- to 500 year return period, while the load factors are drastically reduced.

The highest design tension found from the ALS case will from now be referred to as $T_{d,ALS*}$ since it is not a governing design criterion.

11.7 Evaluation of initial mooring line design

The governing design tension is the ULS design tension, $T_d = 16673kN$ which resulted in a utilization factor of 0.83 of the mooring line. The initial mooring design is therefore acceptable according to the traditional short term design approach. For a real design case, it could be considered to reduce the chain dimensions in order to get a higher utilization factor and thereby a more optimized design. However, the main objective in this thesis is not to optimize the design itself, but to compare design methods. Hence, the most important is that the mooring lines have realistic dimensions to represent a real case. A utilization factor of 0.83 is considered to be within the acceptable range, and hence the initial mooring line design is kept for further analyses.

Chapter 12

POT long term analysis

A Random Storm approach was applied for the long term analysis of mooring line tension. The theory behind this is described in Chapter 6.4 and hence the following sections will focus mainly on the practical use of the method.

12.1 Input to long term analysis

First, a proper criteria for selection storms had to be chosen. The results of the short term analyses indicated that the line loads were more sensitive to wave loads than wind loads. Hence, the H_s was used as parameter for selection of storm events. A threshold of $H_s > 6m$ was chosen to define storm events. This resulted in 143 unique storm events, each consisting of a different number of storm steps. Each storm step is defined as a sea stat with duration of 3 hours. The average number of storm steps per storm was 3.6, resulting in a total number of storm steps for all storms of 514.

12.1.1 Wind and waves

The H_s and T_p used in the simulations of each storm step was taken directly as given in the NORA10 hindcast data. The wind speed given in the hindcast data is the 1-hour mean wind speed given every third hour. This was assumed to be representative for the mean wind speed for the whole 3-hour sea state. Hence, the turbulent wind time series was generated

so they had the same mean wind speed as given in the hindcast data scaled to the reference height of 119m.

The wind and wave heading directions for each sea state are defined as given in the hindcast data for each storm step.

12.1.2 Current

While the H_s and wind speed used in the long term analysis can be taken directly from the hindcast data, no proper long term data are available for current on the location. Hence, a simplified current model relating the current to the waves and wind was introduced. Here, the total current was for simplicity assumed to consist of three components; wind generated current, storm surge currents and tidal currents. This is somewhat imprecise, considering that the storm surge currents will have contributions both from atmospheric pressure differences and wind, *DNV-RP-C205 (2017)*. However, it is here assumed that the storm surge comes solely from variations in atmospheric pressure and that it is therefore possible to separate it from the wind induced currents. In the below sections it will be further elaborated on how the magnitude of the different components are estimated for each sea state.

The wind generated current can according to *DNVGL-RP-C205 Environmental conditions and environmental loads* (2017) be approximated as

$$v_{cur,wind} = k_w \cdot U_{10} \tag{12.1}$$

where $v_{cur,wind}$ is given in m/s, U_{10} is the mean wind speed 10 m above sea level given in m/s and k_w is a constant in the range 0.015 to 0.03. The value of k_w was set to 0.025.

The storm surge current is assumed to be proportional to the H_s and is hence estimated from

$$v_{cur,surge} = k_s \cdot H_s \tag{12.2}$$

where $v_{cur,surge}$ is given in m/s and k_s is a constant. The value of k_s was chosen so that

in a sea state with H_s corresponding to a 50 year return period the resulting storm surge current velocity is equal to the 50 year return period storm surge current velocity given in the Metocean Design Basis. This resulted in $k_s = 0.07$.

The depth-averaged flow of an average spring tidal current at Buchan Deep is in the Metocean Design Basis given as 0.4 m/s. In the simplified current model used for the long term analysis, the tidal current contribution to the total current is set to a constant value of 0.4 m/s for all simulations.

$$v_{cur,tide} = 0.4m/s \tag{12.3}$$

The direction of the different current components will in the real case be depending on many variables, and can also have significant variations depending on the water depth. In the simplified current model, it is assumed that all current components are acting in the wind direction. This will probably lead to conservative results.

In order to verify that the constants k_s and k_w are calibrated correctly, the current corresponding to a 10 year return period environment is estimated:

$$v_{cur,10y} \approx k_w \cdot U_{10m,10y} + k_s \cdot H_{s,10y} + v_{cur,tide} = 1.73m/s \tag{12.4}$$

Here, $U_{10m,10y}$ is the wind speed at 10m above the sea surface corresponding to a 10 year return period which was taken as 28.4 m/s according to the Weibull distribution in Chapter 7.4. Similarly, $H_{s,10y}$ was taken as 8.8 m according to the Weibull distribution established in Chapter 7.3.2. The estimate of the 10 year return period current velocity is very close the value of 1,70 m/s as given in the Metocean Design Basis. This indicates that the simplified current model at least provides reasonable estimates for the extreme values of the current. Nevertheless, it is likely that the assumption of all current components acting in the same direction in general will provide too high current speeds for most sea states.

12.1.3 Aerodynamic model

Three different models for the aerodynamic loads were used depending on if the mean wind speed in the storm step corresponded to the wind regime below rated ($U_{119} \leq 11.4m/s$), the operational regime above rated ($11.4m/s < U_{119} \leq 25m/s$) or in the shutdown condition ($25m/s < U_{119}$). The aerodynamic load models corresponding to each of the wind regimes are described in Chapter 9.2.9.

12.2 Establishing a long term distribution of largest mooring line tension

When the storm sample was selected, 20 analysis were performed for each storm step using different random wind- and wave seeds. This resulted in a total number of 10280 time domain simulations being performed, each with a duration of 11200 seconds (the first 400 seconds were assumed to include transients and was hence not included in the analyses). The POT approach described in Chapter 6.4 could then be applied to simulation results.

Mooring Line 1 was expected to experience the most severe loading since it has orientation towards the north. According to the Metocean Design Basis the largest H_s corresponding to 50 year return period is coming from the north. The results of the time domain simulations in the long-term analysis also confirmed that Line 1 experienced the highest tensions. Hence, the rest of this section is concerned with analysis of Mooring Line 1.

12.2.1 Short term variability of maximum line response within a storm

First, it is assumed that the largest line tension within a sea state is Gumbel distributed so the distribution of the maximum line tension in storm step m of storm number k is given by

$$F_{X_m|k}(x|k) = exp\Big(- exp(-\frac{x - \gamma_{m,k}}{\beta_{m,k}})\Big) \tag{12.5}$$

An estimate for the Gumbel parameters for each storm step was established using the method

of moments on the sample consisting of the largest line tension value in each of the 20 simulations of the sea state. The Gumbel parameters for the distribution of the maximum response in step number m of storm k can be approximated using the following relations, Vikenes (2018):

$$\gamma_{m,k} = \hat{\mu}_{X_{m,k}} - 0.5772\beta_{m,k} \tag{12.6}$$

$$\beta_{m,k} = \frac{\sqrt{6}}{\pi}\sigma_{X_{m,k}} \tag{12.7}$$

where $\hat{\mu}_{X_{m,k}}$ is the mean value and $\sigma_{X_{m,k}}$ is the standard deviation of the extreme value sample for storm step m in storm k obtained from the 20 time domain simulations using different wind- and wave seeds.

It is not given that the number of maxima for the mooring line tension is large enough in 3-hour sea state so the extreme value value is Gumbel distributed. The assumption that the maximum line response in each storm step is Gumbel distributed should therefore be verified. The fitted Gumbel distribution was therefore plotted together with the observed maximum line responses for some selected sea states. These are shown in Figure 12.1. The plots shows that the goodness of the Gumbel fit is varying a bit from sea state to sea state. It is still assumed that the fit is sufficiently good to model the extreme value distribution in each storm step.

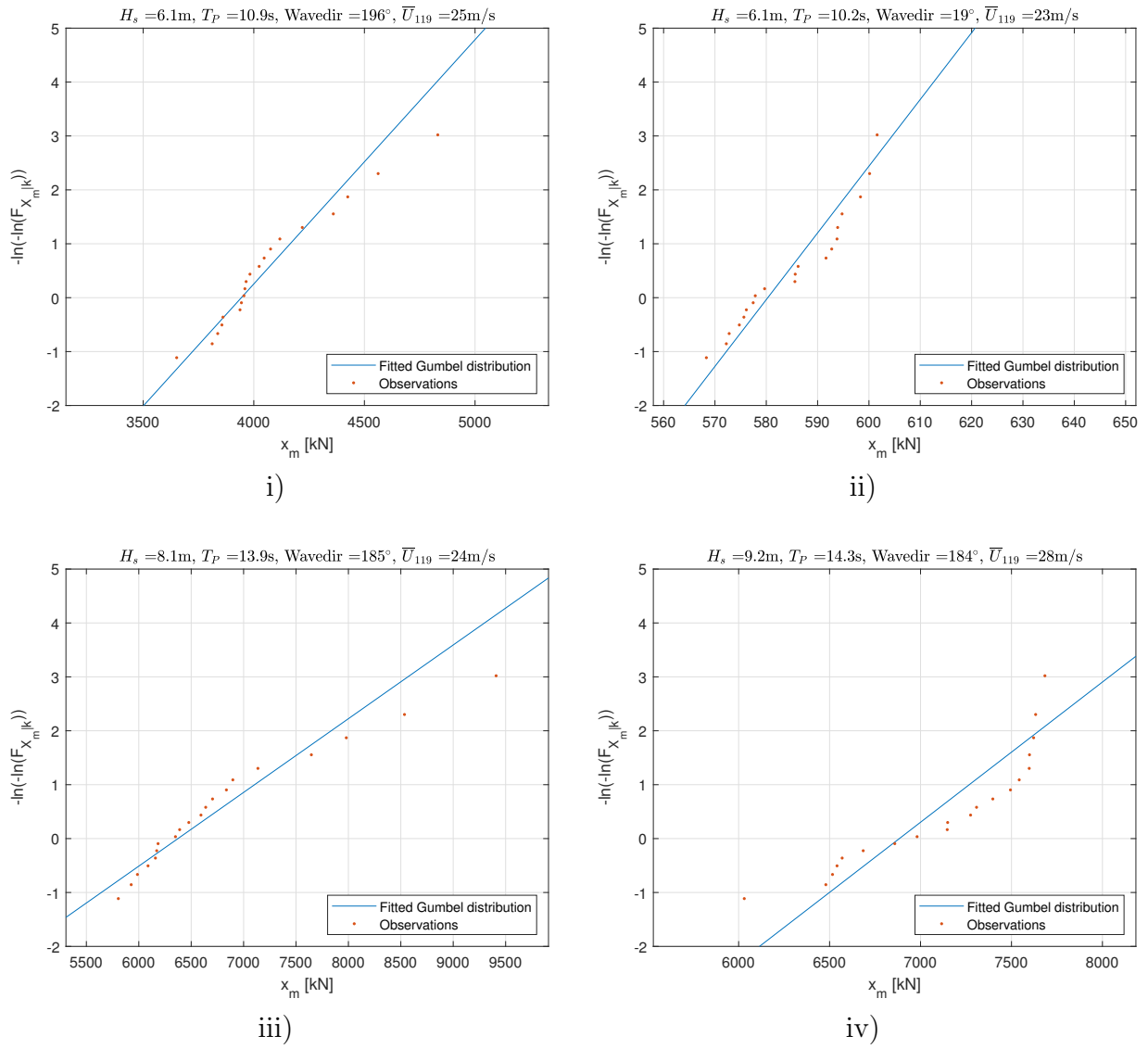

Figure 12.1: Distribution of 3-hour maxima in some selected sea states. Note that *Wavedir* refers to the wave propagating direction.

When Gumbel parameters had been established for all storm steps in a storm, the empirical distribution for the largest line tension, Y_K of storm k with m steps is then obtained as

$$F_{Y_k|k}(y|k) = \prod_{m=1}^{m_k} F_{x_m|k}(y|k) = exp\left(-\sum_{m=1}^{m_k} exp\Big[-\big(\frac{y-\gamma_{m,k}}{\beta_{m,k}}\big)\Big] \right) \tag{12.8}$$

by assuming that the storm steps within a storm are statistically independent.

It is further assumed that the exact distribution given by equation 12.8 can be approximated by a Gumbel distribution given by

$$F_{Y|\tilde{Y}}(y|\tilde{y}) = exp\bigg(- exp\Big[- \frac{y - \tilde{y}}{\beta_G \tilde{y}} \Big] \bigg) \tag{12.9}$$

It is assumed that the exact distribution is close to Gumbel distributed and estimates for $\tilde{y}_k$ is found for each storm by requiring $F_{Y_k|k}(\tilde{y}_k|k) = 0.368$ and solving for $\tilde{y}_k$.

Estimates for β_G is found from considering β_k for all storms using the relation

$$\beta_k = \frac{\sigma_{exact}}{1.28255 \tilde{y}_k} \tag{12.10}$$

where σ_{excact} is the standard deviation of the exact distribution given by equation 12.8, Haver (2017).

Normally, the mean value of all β_k gives a sufficiently good approximation for β_G, Sandbakken (2015). In order to verify whether this is a good assumption or not, β_k is plotted against $\tilde{y}_k$ for all storms. This is shown as blue dots in Figure 12.2. The plot shows for the smallest $\tilde{y}_k$, β_k is significantly lower than for the larger values of $\tilde{y}_k$. This is because the response of the mooring lines is strongly dependent on the direction of the environmental loads. The storms acting in favorable directions for Mooring Line 1 (typically with heading between 270° and 90°), results in very small environmental loads on Mooring Line 1 and for these cases the total tension consists mainly of the tension due to weight of the mooring line itself. Hence, the variance of the maximum tension within these storms will be very low relative to $\tilde{y}_k$ compared to the distributions for storms acting in more unfavorable directions where the environmental loads are governing the mooring line loads. This results in a collection of very low β_k-values corresponding to the lowest $\tilde{y}_k$.

As seen from the plot, the mean value of all 143 β_k, indicated with a blue line in the plot, gives a poor representation of the β_k corresponding to the highest values of $\tilde{y}$. Since it is the storms with highest $\tilde{y}$ that are of interest when considering extreme values corresponding to return periods of 50 years and higher, an alternative way of finding an estimate for β_G was

applied. Instead of taking the mean value of all β_k, only the β_k corresponding to y_k larger than 4000kN were considered. That is the β_k corresponding to the 45 largest $\tilde{y_k}$. For these values there seems to be no clear trend of the relation between β_k and y_k. Hence, the mean value of these β_k-values, denoted $\overline{\beta}^*$, was found to be a much better representation for the β_k corresponding to the higher values of $\tilde{y}_k$. $\overline{\beta}^*$ will therefore be used as estimate for β_G.

That gives $\beta_G = 0.0645$. Hence, the conditional distribution of y given $\tilde{y}$ is given by

$$F_{Y|\tilde{Y}}(y|\tilde{y}) = exp\left(- exp\left[- \frac{y - \tilde{y}}{0.0645\tilde{y}} \right] \right) \tag{12.11}$$

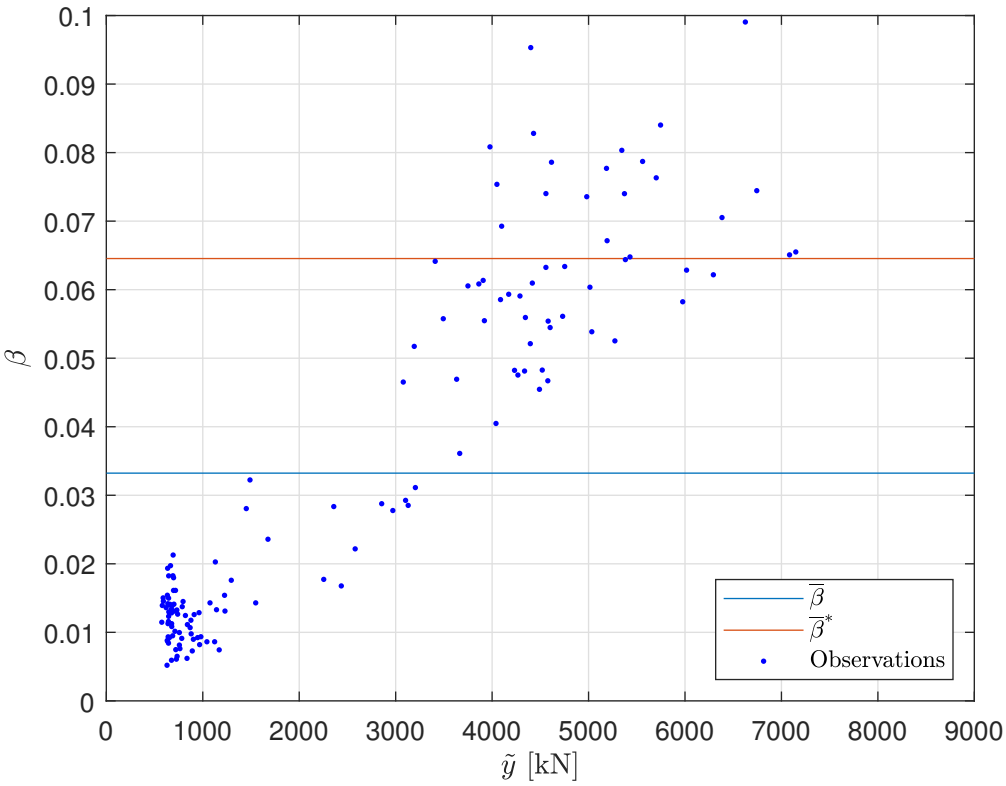

Figure 12.2: The mean value of all β_k, denoted $\overline{\beta}$, and the mean value of the β_k for the 45 largest $\tilde{y}$, denoted $\overline{\beta}^*$, plotted together with β_k for all 143 storms.

12.2.2 Long term variability of most probable maximum line tension for an arbitrary storm

The cumulative distribution function for the most probable largest line tension for an arbitrary storm, $F_{\tilde{Y}}(\tilde{y})$, is normally found by fitting a distribution to the sample $\{\tilde{y}_1, \tilde{y}_2..., \tilde{y}_{143}\}$ found from the exact distribution.

This is a sample from a mixed population consisting of both extreme values and small values of $\tilde{y}$ because the direction of the environmental loads are important for the resulting mooring line tension in Mooring Line 1 as described in Chapter 12.2.1. It will in general be difficult to find a distribution function which fits the whole population well. However, several distributions were tested in order to find the best fit possible. The following distributions where fitted to the whole sample using moment estimators to estimate the distribution parameters:

a) 2-parameter Weibull distribution

b) 3-parameter Weibull distribution with location parameter set to 500 kN

c) 3-parameter Weibull distribution where all three parameters were estimated using moment estimators

d) 3-parameter Generalized Pareto distribution where all three parameters were estimated using moment estimators

The resulting distributions are plotted on Gumbel paper together with the sample in Figure 12.3. The plots indicate that distribution a),b) and c) provide conservative estimates for the upper tail of the distribution. The Generalized Pareto distribution, d), seems to provide the best fit for the upper tail. However, for values of $\tilde{y}$ larger than the highest in the sample, the distribution might actually provide non-conservative values due to the tail shape governed by a strongly negative shape parameter of -0.486. Hence, another approach to model $F_{\tilde{Y}}(\tilde{y})$ was applied.

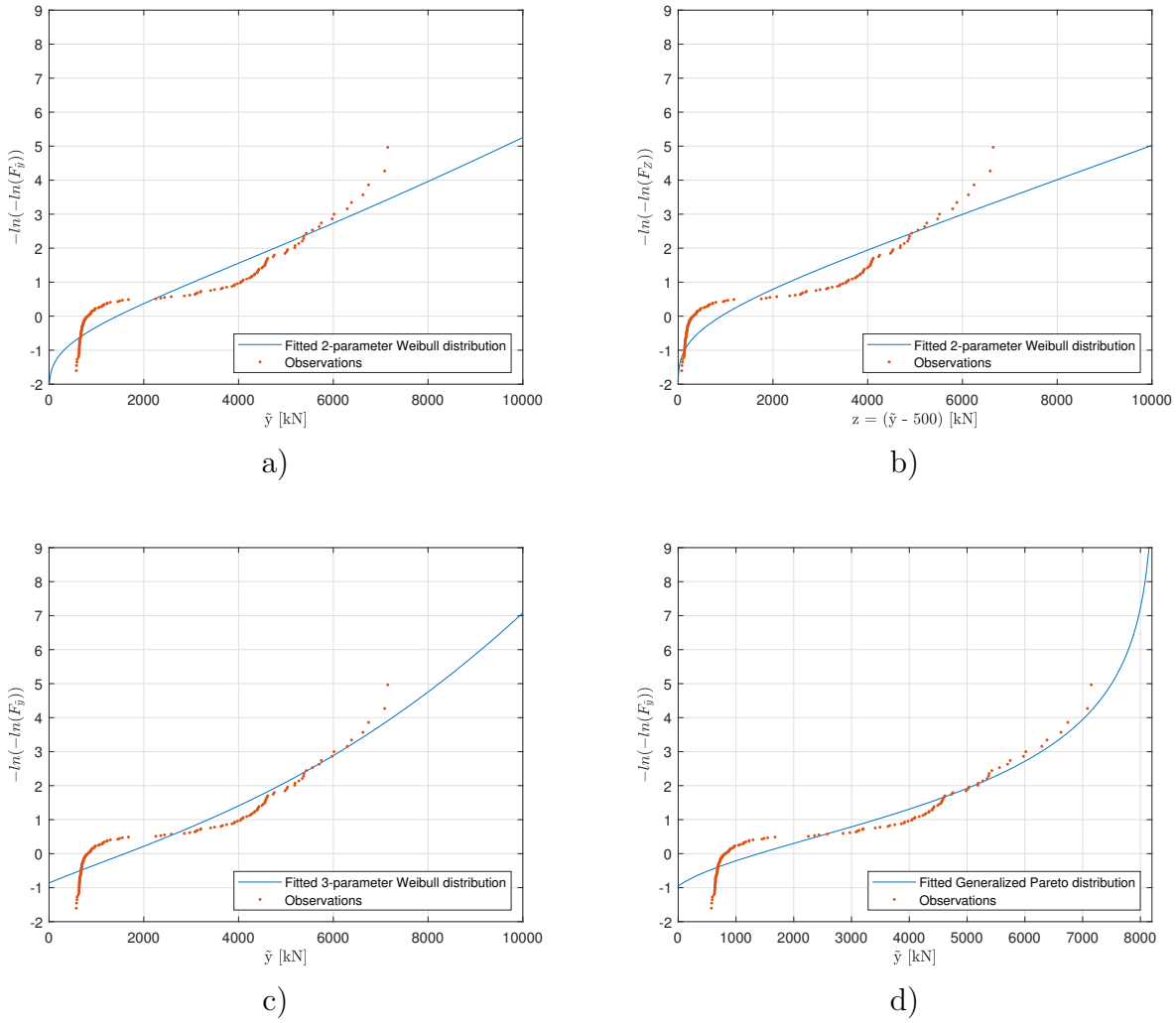

Figure 12.3: Different distribution for $F_{\tilde{Y}}(\tilde{y})$ fitted to the data.

For the maximal line response corresponding to long return periods, it is mainly the upper tail of $F_{\tilde{Y}}(\tilde{y})$ which will be of interest. Instead of considering the whole sample, a tail-fit approach was applied. First, a location parameter of 500 kN was chosen. This is slightly lower than the lowest value in the sample (575kN). The location parameter was subtracted from all values in the sample, providing a new sample where $z = \tilde{y} - 500[kN]$. This sample was plotted in Weibull paper before a linear regression was applied on the parts of the sample with z larger than 3500 kN, corresponding to the 45 largest values. The idea of the linear regression is to utilize that in the Weibull paper, the following relation yields:

$$ln[-ln(1 - F_Z(z))] = \beta_Z ln(z) - \beta_Z ln(\alpha_Z) \tag{12.12}$$

where α_Z and β_Z are the scale and shape parameters of the distribution of z, Leira et al. (2010). The linear regression curve is shown in Figure 12.4. Note that only the z-values used in the linear regression, that is the 45 largest, are included in this figure.

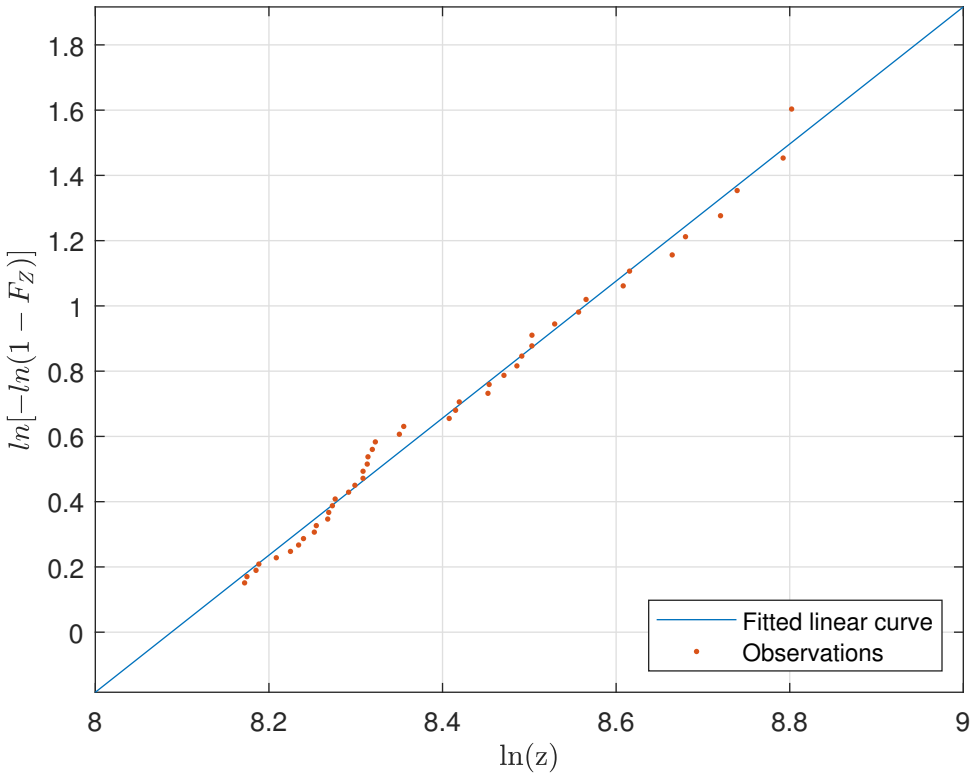

Figure 12.4: Linear regression curve found from the 45 highest values of $\tilde{y}$.

The linear regression is on the form

$$r(s) = \beta_Z \cdot s + c \tag{12.13}$$

where $s = ln(z)$ and $c = -\beta_Z ln(\alpha_Z)$. Hence, the shape parameter, β_Z, is taken as the inclination of the linear curve, while the scale parameter, α_Z is found from

$$\alpha_Z = exp(-r(0)/\beta_z) \tag{12.14}$$

This resulted in $\alpha_Z = 3250kN$ and $\beta_Z = 2.10$, which are used directly as estimates for $\alpha_{\tilde{y}}$ and $\beta_{\tilde{y}}$ in the 3-parameter Weibull distribution for $\tilde{y}$. This resulted in the following distribution:

$$F_{\tilde{Y}}(\tilde{y}) = 1 - exp\Big(- \big(\frac{\tilde{y} - \gamma_{\tilde{Y}}}{\alpha_{\tilde{Y}}}\big)^{\beta_{\tilde{Y}}}\Big) = 1 - exp\Big(- \big(\frac{\tilde{y} - 500}{3250}\big)^{2.10}\Big) \tag{12.15}$$

The distribution is plotted in Figure 12.5. From the figure it is seen that the distribution gives a good fit in the upper tail of the sample as expected.

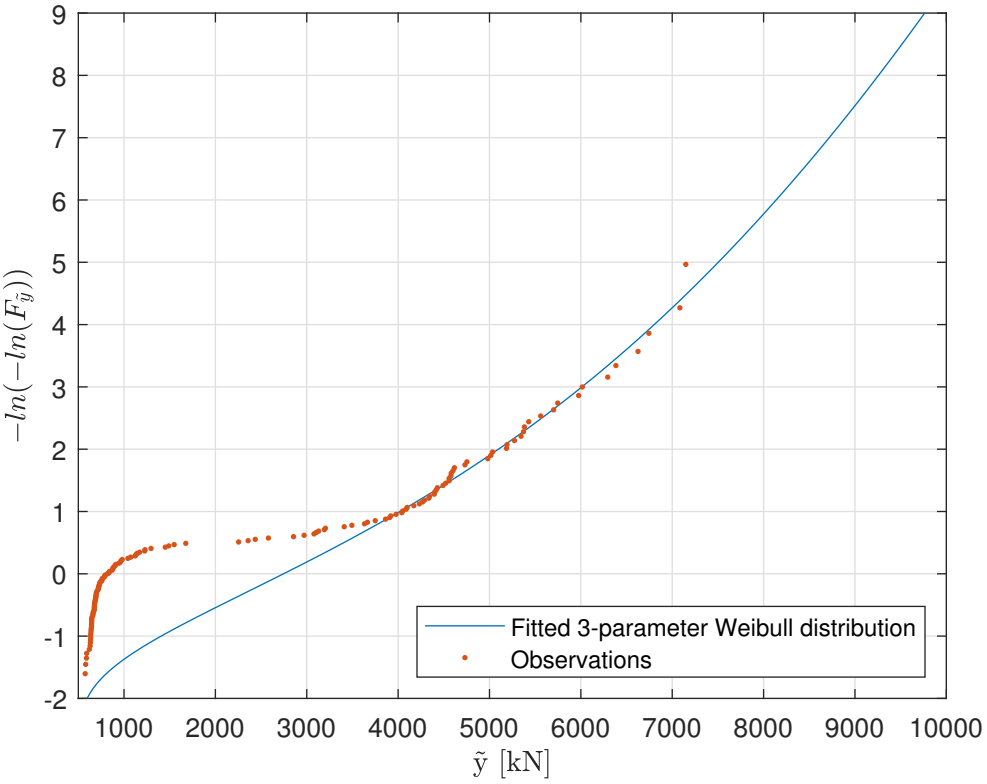

Figure 12.5: Selected distribution for $F_{\tilde{Y}}$.

12.2.3 Stability of the tail fit

As described in Chapter 12.2.2, the distribution $F_Y(\tilde{y})$ was established based only on 45 observations. There is a significant uncertainty related to a tail fit based on so few observations. The stability of the tail behaviour could have been investigated further through a bootstrapping test on the 45 observations. By using Monte Carlo simulation to generate for instance 500 new samples of $\tilde{y}$, and fitting distributions to each of the samples, an indication of the stability of the tail of the distribution will be obtained. This will be similar to the procedure described in Chapter 7.5.2.

Due to time limitations, this was not performed here. Hence, it is noted that there is uncertainty related to the tail behaviour of $F_Y(\tilde{y})$.

12.2.4 Comparison of Weibull tail fit and Generalized Pareto distribution

The Weibull tail fit is compared with the Generalized Pareto distribution fitted to the whole sample by plotting both distributions in the same figure. The result can be seen in Figure 12.6.

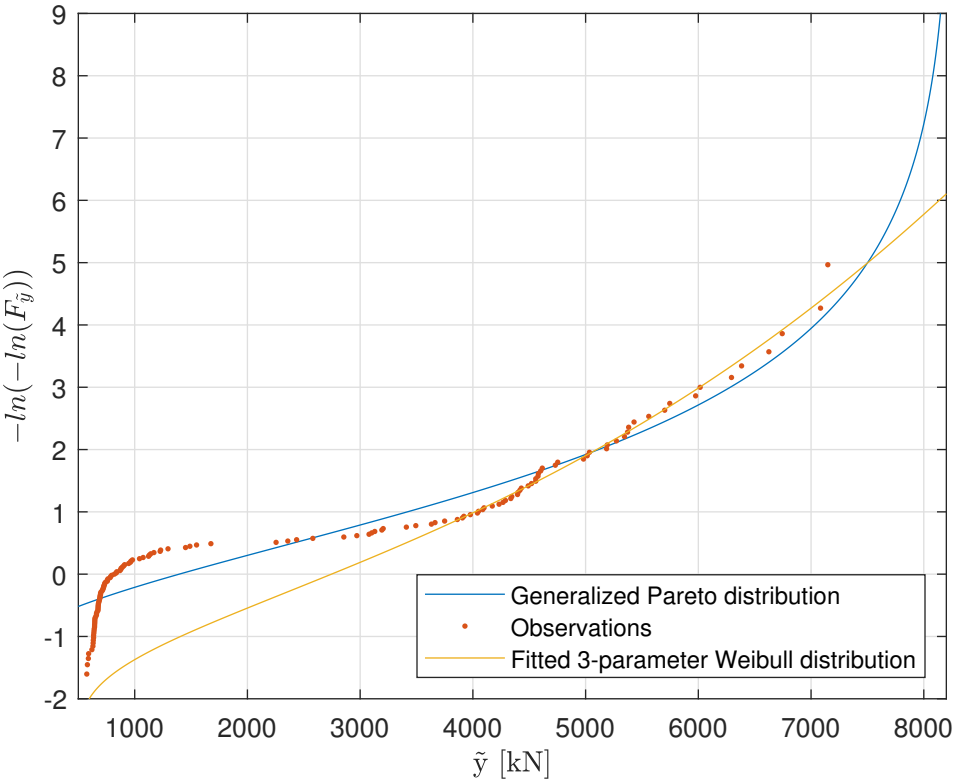

Figure 12.6: Comparison of Weibull distribution obtained by tailfitting and Generalized Pareto distribution.

As seen from the figure, the Generalized Pareto distribution seems to provide conservative estimates for the tail up to a probability level corresponding to about 40 year return period. For larger return periods, the Weibull distribution is more conservative. Considering the trend of the tail of the observations, the Weibull distribution is chosen to model $F_{\tilde{Y}}(\tilde{y})$.

12.3 Line tensions corresponding to different q-probability levels

The long term distribution of the line tension, $F_Y(y)$, is given as

$$F_Y(y) = \int_{\tilde{Y}} F_{Y|\tilde{y}}(y|\tilde{y}) f_{\tilde{Y}}(\tilde{y}) d\tilde{y} \tag{12.16}$$

where $F_{Y|\tilde{Y}}(y|\tilde{y})$ is given by equation 12.11 and $f_{\tilde{Y}}(\tilde{y})$ can be found by differentiating equation 12.15.

The line tension corresponding to different return periods could then be found by solving the equation

$$1 - F_Y(y_q) = \frac{q_{1y}}{n_{1,y}} \tag{12.17}$$

where q_{1y} is the annual probability of exceedance and the variable $n_{1,y}$ is the average number of storms per year. For the selected threshold $H_s > 6m$, $n_{1,y} = \frac{143}{38}$.

A convenient way to solve this equation without performing any explicit integration is by using an IFORM approach similarly as when calculating metocean contour lines in Chapter 11.1.3. The integral in equation 12.16 was transformed using a Rosenblatt transformation scheme introducing the variables

$$u_1 = \Phi^{-1}[F_{\tilde{Y}}(\tilde{y})] \tag{12.18}$$

$$u_2 = \Phi^{-1}[F_{Y|\tilde{y}}(y|\tilde{y})] \tag{12.19}$$

The contour lines corresponding to different return periods could then be found the same way as described in Chapter 11.1.3. The resulting contour lines corresponding to 50, 500 and 10,000 years are shown in Figure 12.7. The reason for including the tension corresponding to 10,000 year return period is because the target safety level of the mooring system is an annual probability of failure of 10^{-4}, *DNVGL-ST-0119 Floating wind turbine structures* (2018).

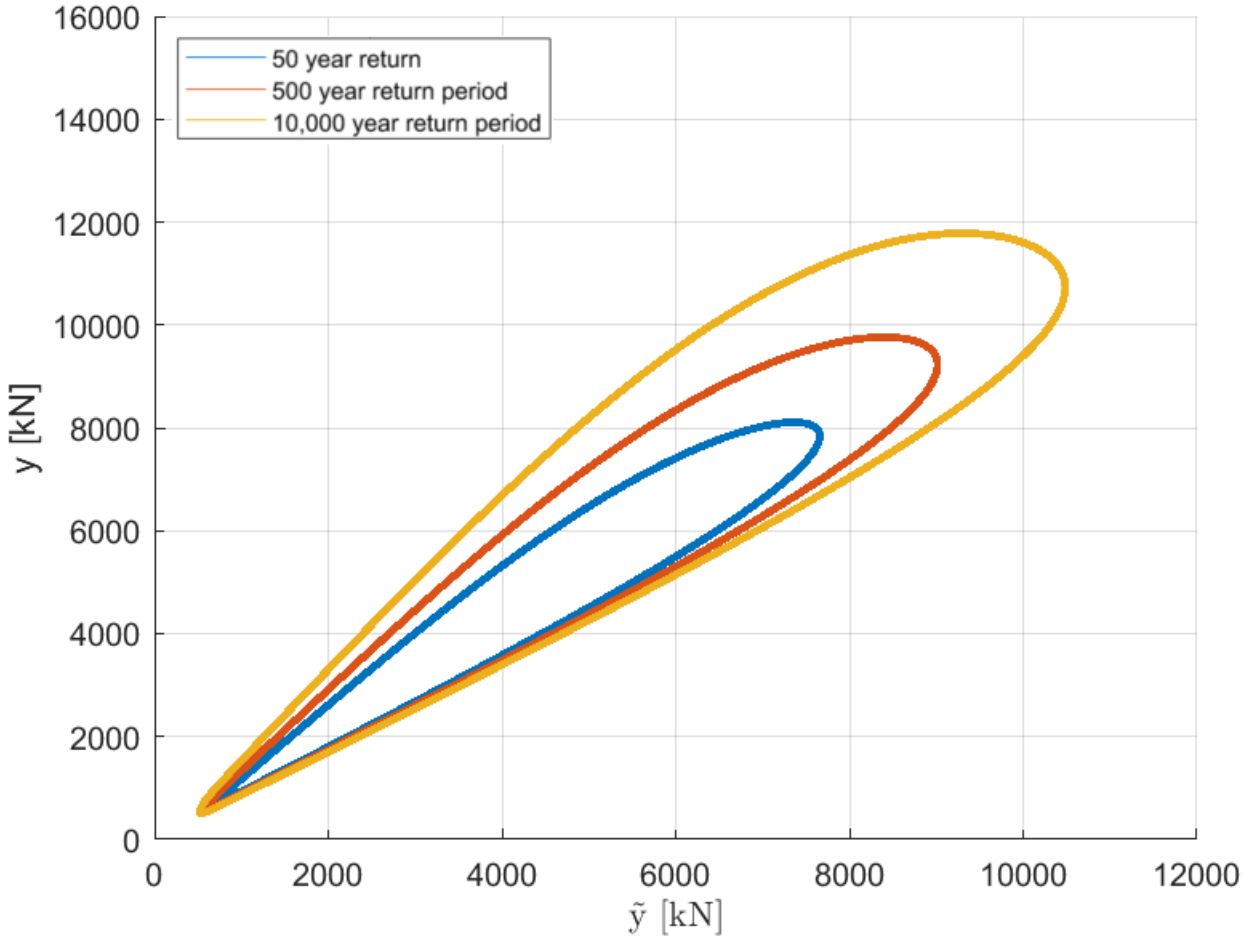

Figure 12.7: Contours corresponding to different return periods.

The maximum line tensions corresponding to the different return periods are taken as the largest values along the respective contour lines. The results are summarized in Table 12.1.

Return period	**Corresponding maximum tension given by $F_Y(y)$ [kN]**
50 years	8108
500 years	9762
10 000 years	11782

Table 12.1: Maximum tensions corresponding to different return periods.

12.4 Contour lines obtained using a Generalized Pareto distribution for $F_{\tilde{Y}}(\tilde{y})$

The results from Chapter 12.2.2 suggested that a Generalized Pareto distribution could also be suitable to model $F_{\tilde{Y}}(\tilde{y})$. Contour lines obtained using a Generalized Pareto distribution for $F_{\tilde{Y}}(\tilde{y})$ are compared to the original contours found using the Weibull distribution for $F_{\tilde{Y}}(\tilde{y})$. The result is shown in Figure 12.8.

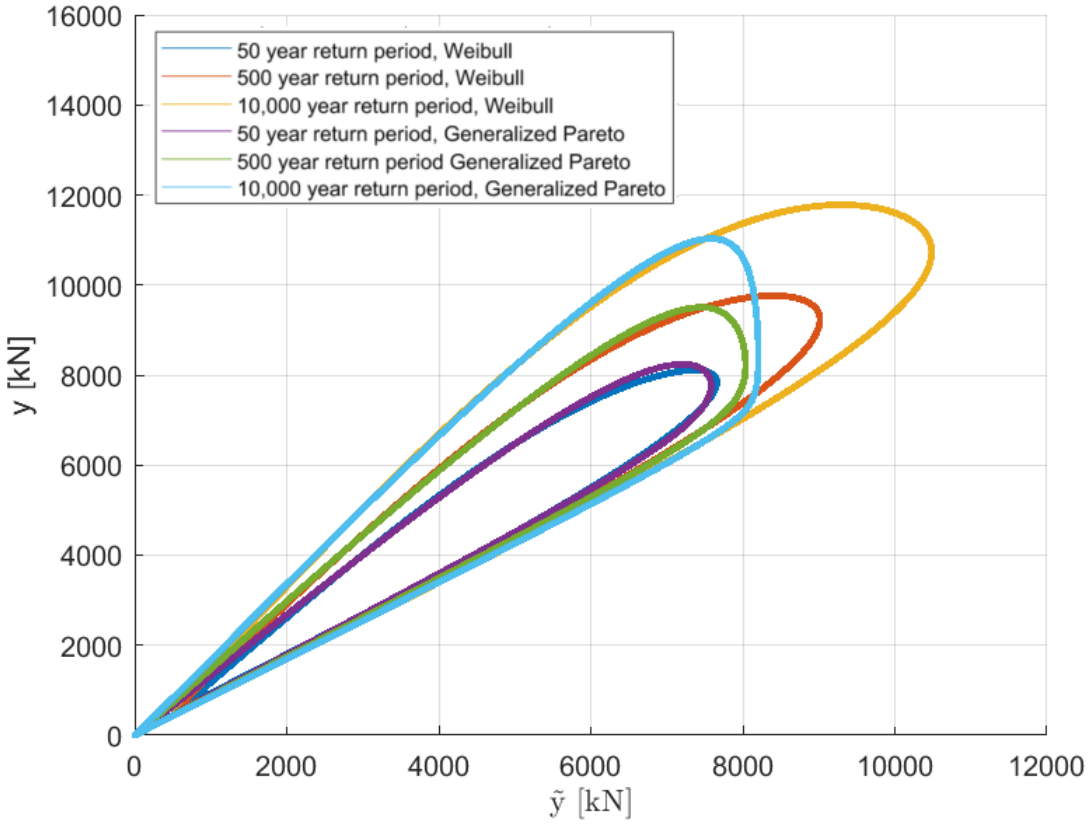

Figure 12.8: Comparison of contour lines found when using a Generalized Pareto distribution for $F_{\tilde{Y}}(\tilde{y})$ compared to those obtained using a Weibull distribution.

As seen from the plot, the contour found using the Generalized Pareto distribution for $F_{\tilde{Y}}(\tilde{y})$ provides slightly larger estimates for the maximum line tension along the contour corresponding to 50 year return period. However, the contours corresponding to 500 and 10.000 year return period found using the Generalized Pareto distribution are less conservative than those

obtained using the Weibull distribution. This is expected considering the differences in the tail behaviour of the the two distributions pictured in Figure 12.6.

The Generalized Pareto distribution provides an upper limit for $\tilde{y}$ as it approaches an vertical asymptote as illustrated in Figure 12.6. If an upper limit for $\tilde{y}$ exists, it can be argued that the Generalized Pareto distribution will provide a much better fit in the tail of the distribution than the Weibull tail fit. However, it is questionable if an upper limit for $\tilde{y}$ exists. In principle, the line tension is governed by environmental loads, which cannot become infinitely large. However, when the Generalized Pareto distribution is fitted to 38 years of data, it is likely that the upper limit will be set too low, so estimates for line tension corresponding to 500 year and higher return periods will be too low. Hence, the results obtained from using the weibull distribution to model $F_{\tilde{Y}}(\tilde{y})$ will be used for further comparison with the traditional short term design approach.

Chapter 13

Comparison of design methods

13.1 Comparison of characteristic tensions

The characteristic tensions found from the traditional approach outlined in *DNVGL-ST-0119 Floating wind turbine structures* (2018) are compared with the tensions corresponding to the same return periods found from the POT long term analysis. The results are shown in Table 13.1. The characteristic tension in the POT approach is taken as the largest value of y along the contour corresponding to the return period of interest.

Characteristic tension	**Traditional short term approach**	**POT long term approach**
$T_{c,50}$ **[kN]**	10477	8108
$T_{c,500}$ **[kN]**	12694	9762

Table 13.1: Comparison of characteristic tensions.

Both $T_{c,50}$ and $T_{c,500}$ found using the traditional short term approach are about 30% higher than the corresponding maximum tensions found using the POT approach. This indicates that the way of modelling the sea states corresponding to 50 and 500 year return period in the traditional approach leads to conservative estimates for T_c. The sea state corresponding to 50 year return period was taken as a combination of H_s, mean wind speed and current

corresponding to 50, 50 and 10 year return periods respectively, all acting in the most unfavorable direction. The sea state corresponding to 500 year return period was taken as the combination of H_s, mean wind speed and current speed corresponding to 500, 50 and 10 year return periods.

In order to avoid too conservative estimates, a more refined way of modelling the sea states could be considered. For the location under consideration, the current loads is an important part of the total loads. Hence, if a joint model for current and the other metocean parameters was adopted, this would probably lead to more correct representation of the current in the sea states under consideration. One possibility could be to adopt a joint model of current and waves, Bruserud (2017). The assumption of all loads acting in the same direction will most likely also introduce conservatism in the estimates for T_c.

However, it is most likely desirable with some conservatism in the estimates of T_c. Instead of comparing the values of T_c found using the two different approaches, it is therefore more interesting to get an indication of the actual return periods corresponding to the estimates for T_c found using the traditional short term approach. This will be considered in the next section.

13.2 Safety level of traditional approach

It is desirable to get an indication of the actual safety level obtained by using the ULS design approach outlined in *DNVGL-ST-0119 Floating wind turbine structures* (2018). In Figure 13.1, the long term distribution of the maximum line tension, $F_Y(y)$, is plotted and the characteristic tensions and the design tension found using the traditional approach are indicated using vertical lines.

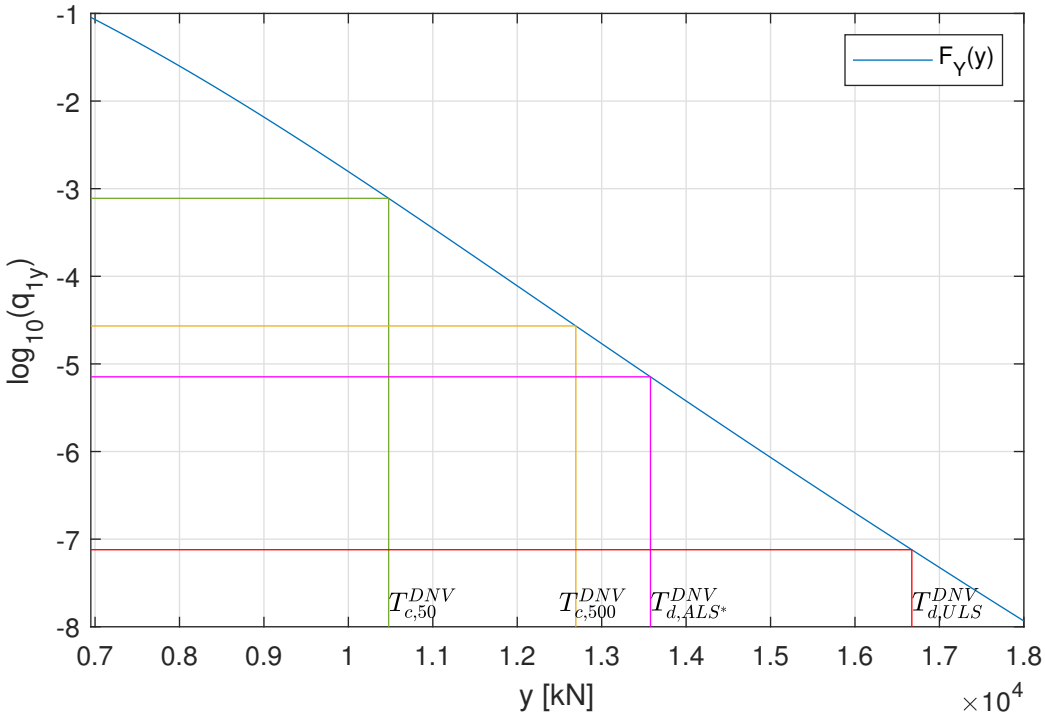

Figure 13.1: Probability of exceedance obtained from $F_Y(y)$ corresponding to the characteristic- and design tensions found using the traditional approach. q_{1y} is the yearly probability of exceedance.

The annual probability of exceedance corresponding to the characteristic and design tensions found using the traditional approach are summarized in Table 13.2. As seen from both the table and the plot, the ULS design tension found using the traditional approach corresponds to an annual exceedance probability of $7.6 \cdot 10^{-8}$ according to the long term distribution of maximum line tension, $F_Y(y)$.

According to *DNVGL-ST-0119 Floating wind turbine structures* (2018), the target safety level of mooring line design in safety class 1 is nominal annual probability of failure of 10^{-4}. The safety level should not only take into account the loads, but also statistical uncertainty of capacity of the different parts of the mooring lines. Nevertheless, the long term analysis indicates that the traditional design approach provides estimates for the ULS design tensions corresponding to a much higher safety level than intended.

It is important to keep in mind that there is uncertainty related to the tail behaviour of

$F_Y(y)$, mainly due to the uncertainty related to the tail of $F_{\tilde{Y}}(\tilde{y})$. Hence, when considering annual exceedance probabilities of magnitude 10^{-7}, there is significant uncertainty related to the estimates for y. Nevertheless, the long term distribution provides an indication of the conservativism in the traditional short term design approach.

Tensions found from traditional design approach [kN]		**Corresponding q_{1y} found from $F_Y(y)$**
$T_{c,50}$	10477	$7.8 \cdot 10^{-4}$
$T_{c,500}$	12694	$2.7 \cdot 10^{-5}$
$T_{d,ULS}$	16673	$7.6 \cdot 10^{-8}$
T_{d,ALS^*}	13578	$7.1 \cdot 10^{-6}$

Table 13.2: Annual exceedance probabilities corresponding to the characteristic tensions and design tensions found using the traditional approach.

Chapter 14

Tower bending moment

The main focus of the thesis is design methods for mooring systems. However, this chapter will briefly describe how the simplified SIMA model can be used for the purpose of performing long-term analyses of tower bending moments. The focus is to discuss some general principles of how the model can be used for this purpose rather than going into details.

14.1 Simplified model

By considering the whole FWT structure as completely stiff, a simplified model for the bending moment in a specified point as function of platform motions can be established. The forces and moments are found by using Newton's 2nd law on the part of the tower above the point in which the bending moment is estimated. This is best explained referring to Figure 14.1. It is desirable to compute the bending moment in point A. Hence, Newton's 2nd law is used only on the part of the tower above this point. Although not drawn into the figure, this also includes the nacelle and rotor. From now, the tower part above the point where it is desirable to compute the bending moment, including the rotor and the nacelle, will be referred to as the tower body. The center of gravity for the tower body will be referred to as COG_{loc} as shown in Figure 14.1.

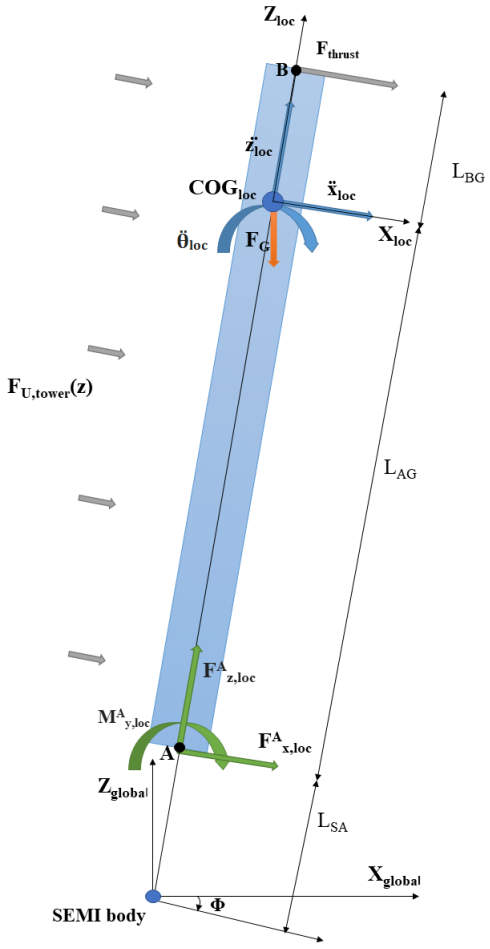

Figure 14.1: Simplified model for tower bending moment.

Two different coordinate systems are defined in the model, one global and one local. The global reference system follows the translational motions of the SEMI body and is the coordinate system to which the accelerations outputted from SIMO refers to. The local system is fixed to the tower with origin in the mass center of the tower body.

14.1.1 Forces in the simplified model

The forces in the model are briefly explained below. Focus is to qualitatively explain where they come from. Note that it is assumed that the point where the tower bending moment is estimated is located above the part of the tower that will experience wave forces. Hence , no

wave forces acting directly on the tower are included in the model.

$\boldsymbol{F_{thrust}}$
The thrust force is the force from the wind on the rotor blades and is described in more detail in Chapter 9.1. In the simplified tower bending moment model it is assumed that the thrust always acts normal on the rotor and hence always in the x-direction of the local reference system.

Below rated wind speed or in the shutdown condition above, the thrust force times series can be estimated from the time series of the wind velocity in hub height outputted by SIMO. For the operational wind regime with wind speeds above the rated, the thrust force is approximated as a constant force. References are made to Chapter 9.2.9 for further details regarding modelling of thrust force.

$\boldsymbol{F_{U,tower}(z)}$
This is wind force on the tower. As shown in Chapter 9.2.4, the drag forces on the tower will be small compared with the thrust in the operational wind regimes, so it can most likely be neglected in these wind regimes. For the shutdown wind regime, it can be included, but will most likely be small compared to the gravitational forces acting on the tower body.

If included, the wind force on the tower should be calculated from the relative velocity between the tower section and the air particles.

$\boldsymbol{F_G}$
The gravity force will always act in the negative z-direction in the global reference frame. It can simply be estimated as $F_G = m \cdot g$, where m is the mass of the tower body.

$\boldsymbol{F^A_{x,loc}}$, $\boldsymbol{F^A_{z,loc}}$ and $\boldsymbol{M^A_{y,loc}}$
These are the unknown axial force, shear force and bending moment it is desirable to estimate.

14.1.2 Estimating the unknown forces and moments

It is assumed that the accelerations of the tower body are known. How these accelerations can be found from the output of the SIMO analyses is described in Chapter 14.2.

Newton's 2nd law applies in all degrees of freedom in the local coordinate system:
Vertical equilibrium of forces

$$F^A_{z,loc} - F_{Gz,loc} = m \cdot \ddot{z} \tag{14.1}$$

where $F_{Gz,loc}$ is the component of the gravitational force acting in the local z-direction.

Horizontal equilibrium of forces

$$F_{thrust} + F_{U,tower} + F^A_{x,loc} = m \cdot \ddot{x} \tag{14.2}$$

where $F_{U,tower}$ is the total wind force on the tower.

Moment equilibrium about point A

$$F_{thrust} \cdot (L_{AG} + L_{BG}) + F_{U,tower} \cdot z_{a,U} + F_{Gx,loc} \cdot L_{AG} - m\ddot{x} \cdot L_{AG} + M^A_{y,loc} = \ddot{\theta} \cdot I^A_y \tag{14.3}$$

where $z_{a,U}$ is the attack point of the total wind force on the tower calculated from the wind profile and the tower velocity in the x-direction, the term $m\ddot{x} \cdot L_{AG}$ is the moment from the inertial force acting in the opposite direction of the acceleration of the center of gravity, I_A is the moment of inertia of the tower body around the y-axis in point A and $\ddot{\theta}$ is the angular acceleration.

14.2 Finding the accelerations in the local center of gravity

The accelerations in all 6 degrees of freedom are outputted by SIMO referring to a global coordinate system with origin located on the mean water surface. In order to get the accelerations in the local center of the gravity referring to the local coordinate system as pictured in Figure 14.1, the coordinates have to be transformed using a rotation matrix. References are made to Fossen (2011) for further details.

14.3 Consequences of assuming totally stiff structure

A load effect which is not included in the simplified model is the loads induced due to the tower shadow effect. This load will have a frequency three times higher than the rotation frequency of the rotor because it will be induced every time a blade passes in front of the tower. The rotor speed of the DTU 10 MW reference turbine is 6-9.6RPM (0.1-0.16 HZ), González Horcas et al. (2016). This implies that the frequency of a blade passing in front of the tower, the 3p frequency, will vary between 0.3 and 0.48 Hz.

According to Wang (2014), the first eigenmode of the fixed DTU 10MW reference wind turbine structure has a natural frequency of 0.25Hz. Since the 3p loads are relatively close to the first eigenmode of the turbine, significant dynamic amplification of the 3p load can be expected. Due to the high frequency and high dynamic amplification of the 3p load, this should be accounted for when performing fatigue analysis. Hence, the simplified model is not suited for performing fatigue analyses. It should also be investigated further if the 3p loads could have any significant contribution to the ULS design loads. If so, it should be looked into how 3p loads can be included in the simplified model when performing long-term analyses.

Chapter 15

Conclusion and recommendations

15.1 Conclusion

The main objective of the thesis is to increase the competence related to floating wind turbines with special focus on design methodology for the mooring system. It was found that a simplified model of the floating wind turbine can be established by modelling the aerodynamic loads differently in the three main wind speed regimes; below rated wind speed, operating regime above rated and in shutdown condition.

The comparison of the characteristic tensions found using a traditional short term design approach outlined in *DNVGL-ST-0119 Floating wind turbine structures* (2018) with the results of a POT long term analysis suggests that the traditional design approach results in conservative values for the characteristic tensions. It was found that $T_{c,50}$ found using the traditional approach corresponds to a line tension with annual exceedance probability of $7.8 \cdot 10^{-4}$ according to the long term distributions established using a POT approach. $T_{c,500}$ found using the traditional short term approach corresponds to an annual exceedance probability of $2.7 \cdot 10^{-5}$. This suggest that modelling the sea states in the traditional approach using H_s, wind speed and current all acting in the same direction and corresponding to 50, 50 and 10 year return period respectively for the ULS case and 500, 50 and 10 year return periods respectively, for the ALS case, introduces significant conservatism in the estimates for T_c.

The ULS design tension, T_d, estimated using the traditional short term approach as outlined

in *DNVGL-ST-0119 Floating wind turbine structures* (2018) corresponds to a line tension with annual exceedance probability less than 10^{-7} according to the long term distribution established in the long term POT analyses. Considering that the target safety level for safety class 1 stated in *DNVGL-ST-0119 Floating wind turbine structures* (2018) is an annual probability of failure of 10^{-4}, the result indicates that the traditional design approach introduces more conservatism than desired for the case considered in this thesis.

In the POT long term analysis, the selection criteria used for establishing a storm sample was $H_s > 6m$. Due to the sensitivity of storm direction to the mooring line response, the sample of most probable storm line tensions, was mixed consisting of both small and high values. Only the 45 highest values for $\tilde{y}$ was used to fit the Weibull distribution used to model $F_{\tilde{Y}}(\tilde{y})$. In other words, $F_{\tilde{Y}}(\tilde{y})$ is fitted to a relatively small sample and there is uncertainty related to the tail of the distribution. Hence, the estimates for y corresponding to return periods of 500 years and more are expected to be related to a significant degree of uncertainty. Nevertheless, the results from the long term analysis provide an indication of the level of conservatism in the traditional short term mooring design approach.

For future POT long term analyses of mooring line tension, it is recommended also to include a directional criteria for the wave and wind heading when selecting a storm sample. In that way, the storm sample will consists of the storms resulting in the highest mooring line tensions for the mooring line under consideration and $F_{\tilde{Y}}(\tilde{y})$ can be established using the results of the simulations of all storms in the sample.

The simplified model can also be used for long term analysis of tower bending moments. It should be investigated further which implications the assumption of completely stiff tower will have for the estimation of ULS loads.

15.2 Recommendations for further work

- The simplified SIMA model used in this thesis should be further verified by comparing response characteristics with a complete model where the turbine blades are modelled and a control system is implemented. This will be useful in order to investigate how well the simplified aerodynamic model represents the thrust loads on the rotor.

- The current model used in the long term analysis should be refined. If possible, a corresponding long-term analysis should be performed in an area where long-term current measurement data are available. This will indicate the level of conservatism implemented in the simplified current model used in the long-term statistical analysis.
- A bootstrap test should be performed on the tail fit of $F_{\tilde{Y}}(\tilde{y})$ in order to investigate the stability of the tail fit.
- The mooring line tension is strongly dependent on the heading of the storm. Hence, a corresponding POT analysis could be performed where the criteria for selection of a storm sample not only includes a H_s-threshold, but also a directional criteria.
- Corresponding long-term analyses should be performed for other floating wind turbine concepts in other locations. The results could indicate if the traditional design approach outlined in *DNVGL-ST-0119 Floating wind turbine structures* (2018) is consequently providing conservative estimates for ULS design of mooring lines.

Bibliography

Baarholm, G. S., Haver, S. & Økland, O. D. (2010), 'Combining contours of significant wave height and peak period with platform response distributions for predicting design response', *Marine Structures* **23**(2), 147–163.

Bak, C. & Zahle, F. (2013), 'Description of the dtu 10 mw reference wind turbine', *DTU Wind Energy Report-I-0092* .

Bruserud, K. (2017), 'Simultaneous stochastic model of waves and currents for prediction of structural design loads', *PhD thesis, NTNU* .

Chakrabarti, S. K. (2005), *Handbook of Offshore Engineering*, Elsevier Science & Technology.

DNVGL-OS-E301: Position mooring (2015).

DNVGL-RP-C205 Environmental conditions and environmental loads (2017).

DNVGL-ST-0119 Floating wind turbine structures (2018).

Equinor (2018), 'Hywind - leading floating offshore wind solution - equinor.com'.
URL: *https://www.equinor.com/en/what-we-do/hywind-where-the-wind-takes-us.html (Accessed 15.10.18)*

Faltinsen, O. M. (1990), *Sea Loads on Ships and Offshore Structures*, Cambridge University Press.

Flory, J. F. (2016), 'Mooring systems for marine energy converters', *IEEE Conference 19th-23rd of September 2016* .

Fossen, T. I. (2011), *Marine Craft Hydrodynamics and Motion Control*, Wiley.

González Horcas, S., Debrabandere, F., Tartinville, B., Hirsch, C. & Coussement, G. (2016), *CFD study of DTU 10 MW RWT aeroelasticity and rotor-tower interactions*, pp. 309–334.

Haver, S. (2017), 'Metocean modelling and prediction of extremes', *NTNU, Lecture Notes* .

Haver, S. (2018), 'Joint probabilistic model for wind sea and swell: Results for cases with wind sea south - southeast field.', *Unpublished* .

Hole, K. B. (2018), *Design of Mooring Systems for Large Floating Wind Turbines in Shallow Water*, Master's thesis, NTNU.

ISO 19901-1:2015 (2015).

Kelley, N. & Jonkman, B. (2007), 'Overview of the turbsim stochastic inflow turbulence simulator', *Technical Report NREL/TP-500-41137 April 2007* .

Larsen, K. (2015*a*), 'Mooring and station keeping of floating structures –part 2 of 2 tmr4225 marine operations – lecture 8 and 9', *NTNU Lecture Notes* .

Larsen, K. (2015*b*), 'Static equilibrium of a mooring line', *NTNU Lecture Notes* .

Leira, B., Moan, T., Haver, S. & Spidsøe, N. (2010), *TMR4235, Stochastic Theory of Sea Loads: Probabilistic Modelling and Estimation*, NTNU Department of Marine Technology.

Lien, J. & Løvhøiden, G. (2015), *Generell fysikk for universiteter og høgskoler, Bind 1*, Universitetsforlaget.

Luan, C. (2014), 'Modeling and analysis of a 5 mw semi-submersible wind turbine combined with three flap-type wave energy converters', *ASME 2014 33rd International Conference on Ocean, Offshore, and Arctic Engineering* .

Mathisen, M., Meyer, A. & Kvingedal, B. (2014), 'Hywind buchan deep metocean design basis', *Internal Equinor document* .

Newland, D. (1993), *Random vibrations, spectralm and wavelet analysis, Third Edition*, Longman Scientific & Technical.

Nielsen, M. (2011), 'Parameter estimation for the two-parameter weibull distribution', *BYU ScholarsArchive* .

NORSOK N-003:2017 (2017).

Orsted (2018), 'Europe powered by green energy'.
URL: *https://orsted.com/en/About-us/About-orsted/Green-is-cheaper-than-black/North-seas (accessed 10.11.18)*

PrinciplePower (2018), 'Principle power, inc. - globalizing offshore wind'.
URL: *http://www.principlepowerinc.com/en/windfloat (Accessed 06.12.18)*

Ramnäs Bruk Product Catalogue (2015).

Ross, E., Astrup, O. C., Bitner-Gregersen, E., Bunn, N., Feld, G., Gouldby, B., Huseby, A., Liu, Y., Randell, D., Vanem, E. & Jonathan, P. (2018), 'On environmental contours for marine and coastal design', *Cornell University* .

S. Tromans, P. & Vandersohuren, v. (1995), 'Response based design conditions in the north sea: Application of a new method', *OTC7683, Texas* .

Sandbakken, S. (2015), 'Long term analysis of semi submersible offset', *Master's Thesis, NTNU* .

SimoManual (2017), *SIMO 4.10.1 Theory Manual*.

Singh, V. & Guo, H. (1997), 'Parameter estimation for 2-parameter generalized pareto distribution by pome', *Stochastic Hydrology and Hydraulics 11:211-227* .

Statoil (2014), 'Presentation, mooring hywind scotland', *Internal Equinor document* .

Subcon (2018), 'Subcon supplies gravity anchors for sapurakencana on the john brookes pipeline repair project'.
URL: *http://www.subcon.com/subcon-supplies-gravity-anchors-for-sapurakencana-on-the-john-brookes-pipeline-repair-project/ (Accessed 04.12.18)*

Vikenes, O. K. (2018), 'Assessment of necessary air gap of semi-submersible accounting for simultaneous occurrence of wind, wind sea and swell sea', *Master's Thesis, NTNU* .

Vryhof (2010), 'Anchor manual', *Vryhof Anchors B.V* .

Wang, Q. (2014), 'Design and dynamic analysis of a steel pontoon-type semi-submersible floater supporting the dtu 10mw reference turbine', *Master's thesis, NTNU* .

Wind, O. (2018), 'Hywind – offshore wind suction anchor buckets'.
URL: *https://gegroup.com/renewables/offshore-wind (Accessed 07.12.18)*

Xu, K., Gao, Z. & Moan, T. (2018), 'Effect of hydrodynamic load modelling on the response of floating wind turbines and its mooring system in small water depths', *Journal of Physics: Conference Series* **1104**, 012006.

Appendix A

Scatter diagram

Figure A.1: Scatter diagram for Hywind Scotland location.

	Tp [s]																									
Hs [m]		1	2	3	4	5	6	7	8	9	10	11	12	13	14	15	16	17	18	19	20	21	22	23	24	25	SUM	CUMULATIVE SUM
	0.5	0	0	46	606	1169	618	252	192	160	137	88	32	19	8	8	6	1	2	2	0	0	0	0	0	0	3346	3346
	1	0	0	52	1577	4830	4663	3913	2395	1389	964	532	284	166	73	34	9	4	0	2	0	0	0	0	0	0	20887	24233
	1.5	0	0	0	126	4126	5540	4581	4359	2817	1786	1383	737	369	201	83	34	19	2	1	0	0	0	0	0	0	26164	50397
	2	0	0	0	1	730	4837	4758	3227	2763	1857	1389	996	576	239	81	52	11	2	3	0	0	0	0	0	0	21522	71919
	2.5	0	0	0	0	48	1301	4322	2931	1972	1367	873	706	581	238	95	61	22	2	3	0	0	0	0	0	0	14522	86441
	3	0	0	0	0	1	226	2039	2765	1574	1126	616	442	339	224	84	49	12	2	1	0	0	0	0	0	0	9500	95941
	3.5	0	0	0	0	0	17	547	1787	1544	956	479	259	185	124	76	31	14	5	1	1	0	0	0	0	0	6026	101967
	4	0	0	0	0	0	0	109	665	1284	845	469	198	104	67	38	28	9	2	1	0	0	0	0	0	0	3819	105786
	4.5	0	0	0	0	0	0	21	155	776	690	369	163	72	43	15	14	4	0	0	0	0	0	0	0	0	2322	108108
	5	0	0	0	0	0	0	1	29	309	499	348	146	39	36	20	8	9	3	1	0	0	0	0	0	0	1448	109556
	5.5	0	0	0	0	0	0	0	3	108	279	257	127	37	18	11	4	5	0	0	0	0	0	0	0	0	849	110405
	6	0	0	0	0	0	0	0	0	27	121	172	118	51	22	7	4	1	1	0	0	0	0	0	0	0	524	110929
	6.5	0	0	0	0	0	0	0	0	6	49	89	82	36	11	7	7	1	0	0	0	0	0	0	0	0	288	111217
	7	0	0	0	0	0	0	0	0	0	10	28	57	24	9	6	2	0	0	0	0	0	0	0	0	0	136	111353
	7.5	0	0	0	0	0	0	0	0	0	6	26	17	24	10	1	1	0	0	0	0	0	0	0	0	0	85	111438
	8	0	0	0	0	0	0	0	0	0	1	4	6	11	4	5	3	0	0	0	0	0	0	0	0	0	34	111472
	8.5	0	0	0	0	0	0	0	0	0	0	3	6	6	6	3	3	0	0	0	0	0	0	0	0	0	27	111499
	9	0	0	0	0	0	0	0	0	0	0	1	1	3	2	4	0	0	0	0	0	0	0	0	0	0	11	111510
	9.5	0	0	0	0	0	0	0	0	0	0	0	0	0	1	1	0	0	0	0	0	0	0	0	0	0	2	111512
	10	0	0	0	0	0	0	0	0	0	0	0	0	0	0	0	0	0	0	0	0	0	0	0	0	0	0	111512
	SUM	0	0	98	2310	10904	17202	20543	18508	14729	10693	7126	4377	2642	1336	579	316	112	21	15	1	0	0	0	0	0		

Appendix B

Conditional distribution of H_s given U_{10}

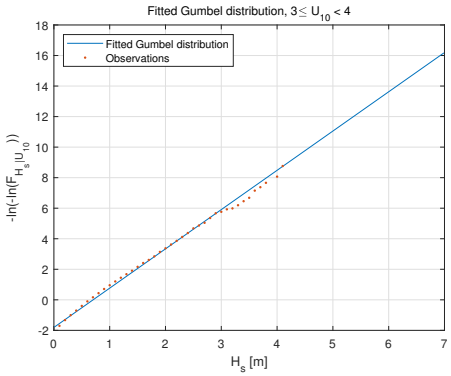

Fitted Gumbel distribution.

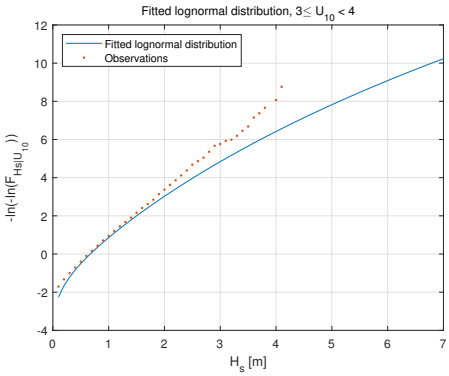

Fitted lognormal distribution.

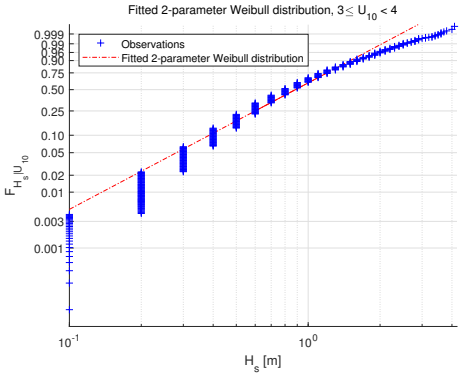

Fitted Weibull distribution plotted on Weibull paper.

Figure B.1: Fitted conditional distributions of Hs for $3 < U_{10} < 4$ m/s

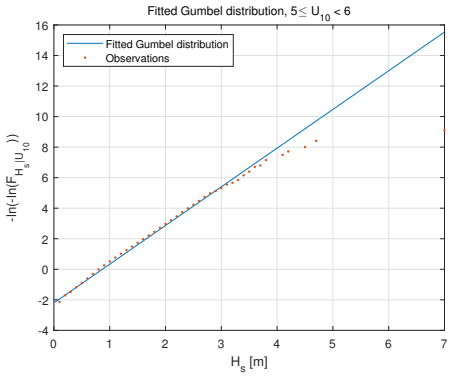

Fitted Gumbel distribution.

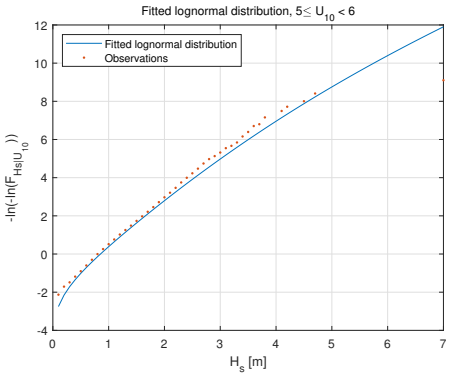

Fitted lognormal distribution.

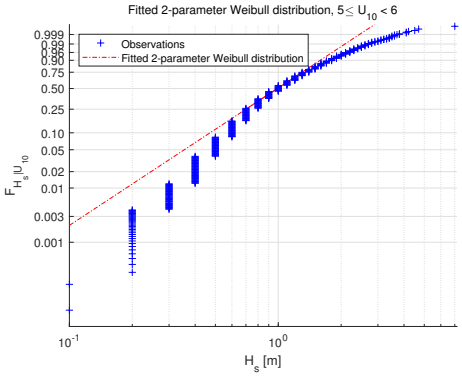

Fitted Weibull distribution plotted on Weibull paper.

Figure B.2: Fitted conditional distributions of Hs for $5 < U_{10} < 6$ m/s

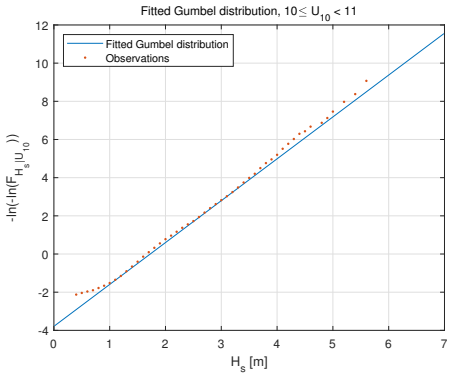

Fitted Gumbel distribution.

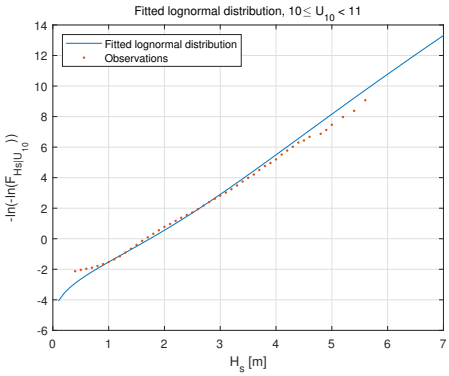

Fitted lognormal distribution.

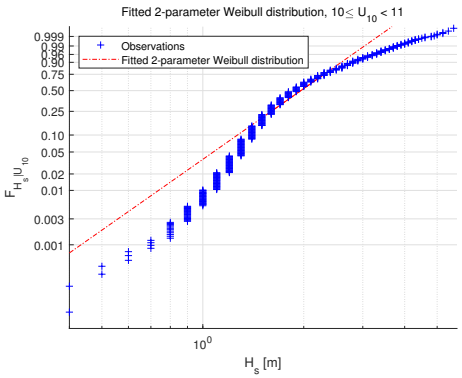

Fitted Weibull distribution plotted on Weibull paper.

Figure B.3: Fitted conditional distributions of Hs for $10 < U_{10} < 11$ m/s

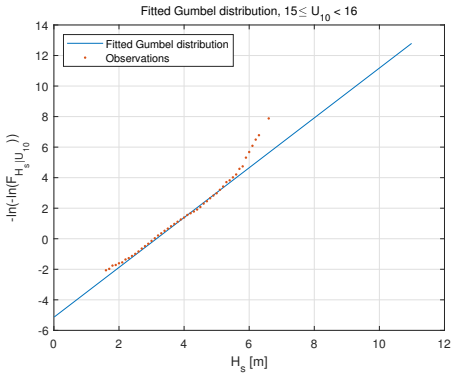

Fitted Gumbel distribution.

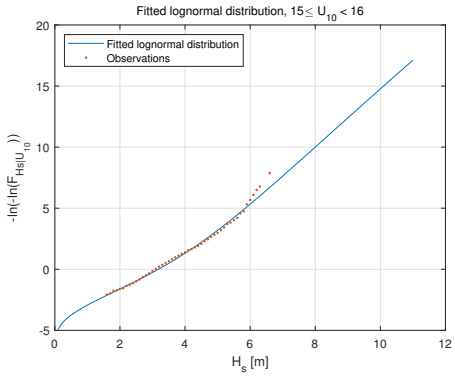

Fitted lognormal distribution.

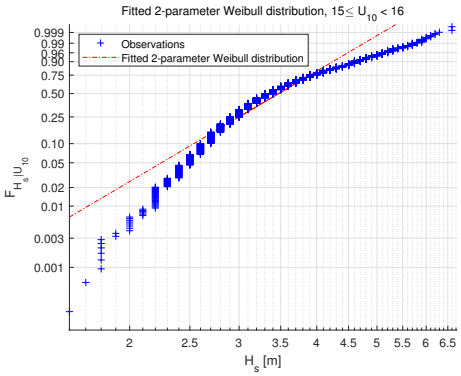

Fitted Weibull distribution plotted on Weibull paper.

Figure B.4: Fitted conditional distributions of Hs for $15 < U_{10} < 16$ m/s

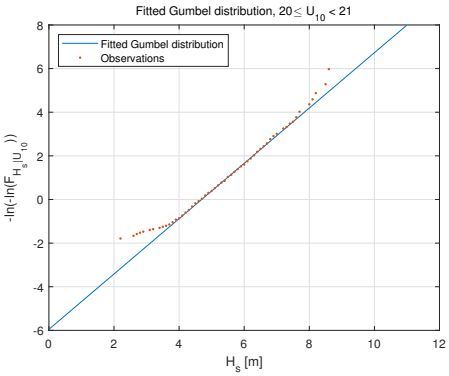

Fitted Gumbel distribution.

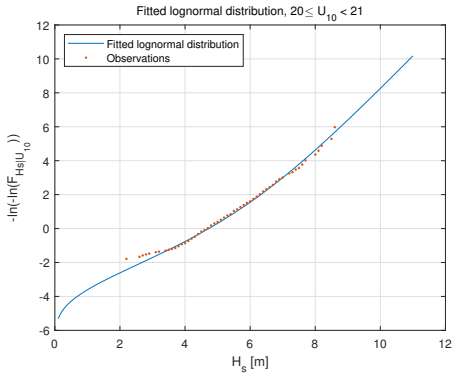

Fitted lognormal distribution.

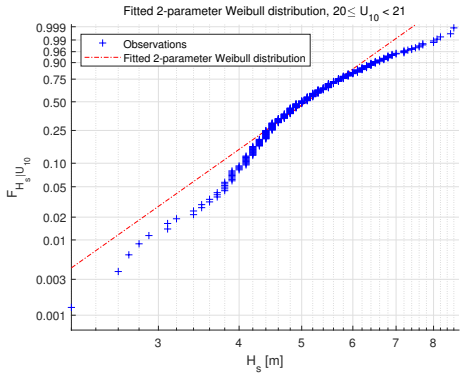

Fitted Weibull distribution plotted on Weibull paper.

Figure B.5: Fitted conditional distributions of Hs for $20 < U_{10} < 21$ m/s

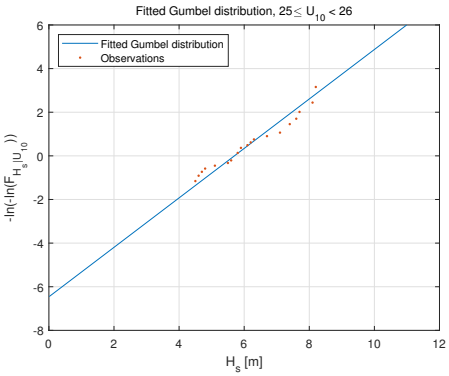

Fitted Gumbel distribution.

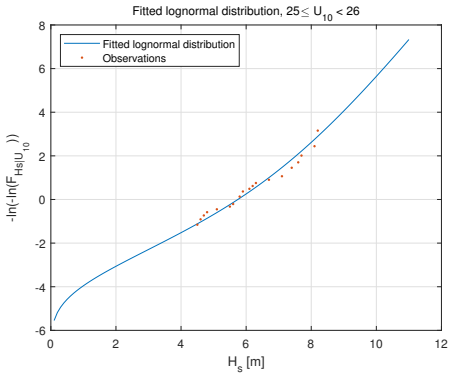

Fitted lognormal distribution.

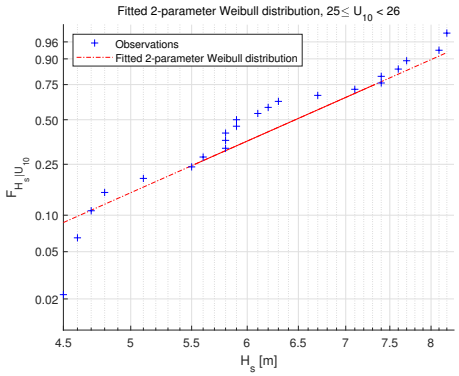

Fitted Weibull distribution plotted on Weibull paper.

Figure B.6: Fitted conditional distributions of Hs for $25 < U_{10} < 26$ m/s

Appendix C

Time series for ULS Load Case 1-4

C.1 ULS Load Case 1

C.1.1 Tension in mooring line 1

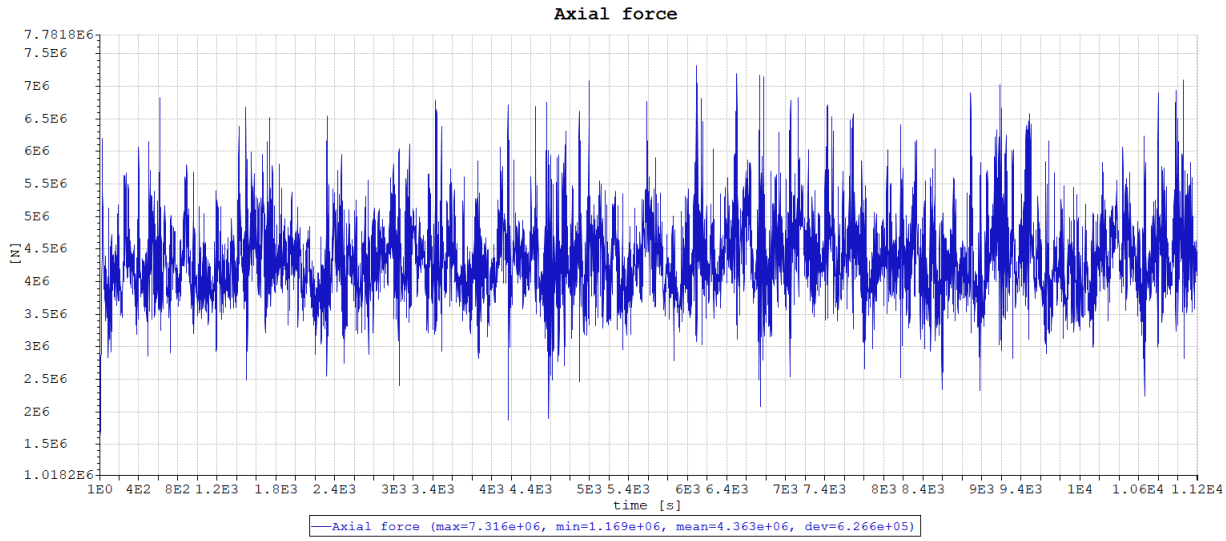

Figure C.1: Time series of tension in mooring line 1.

C.1.2 Surge motion of FWT body

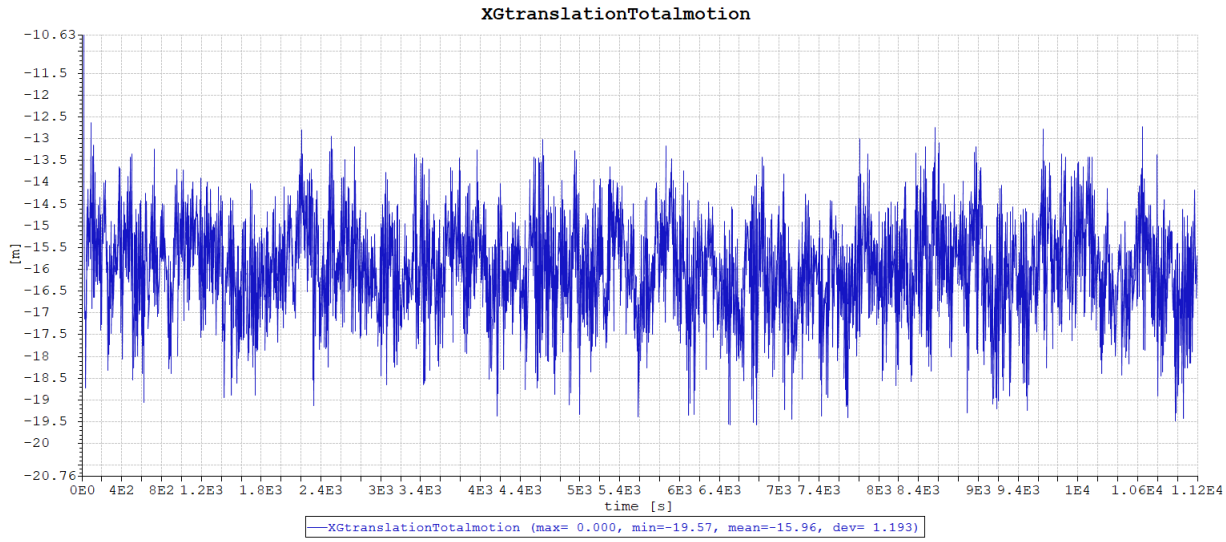

Figure C.2: Time series of surge motion of the FWT.

C.1.3 Heave motion of FWT body

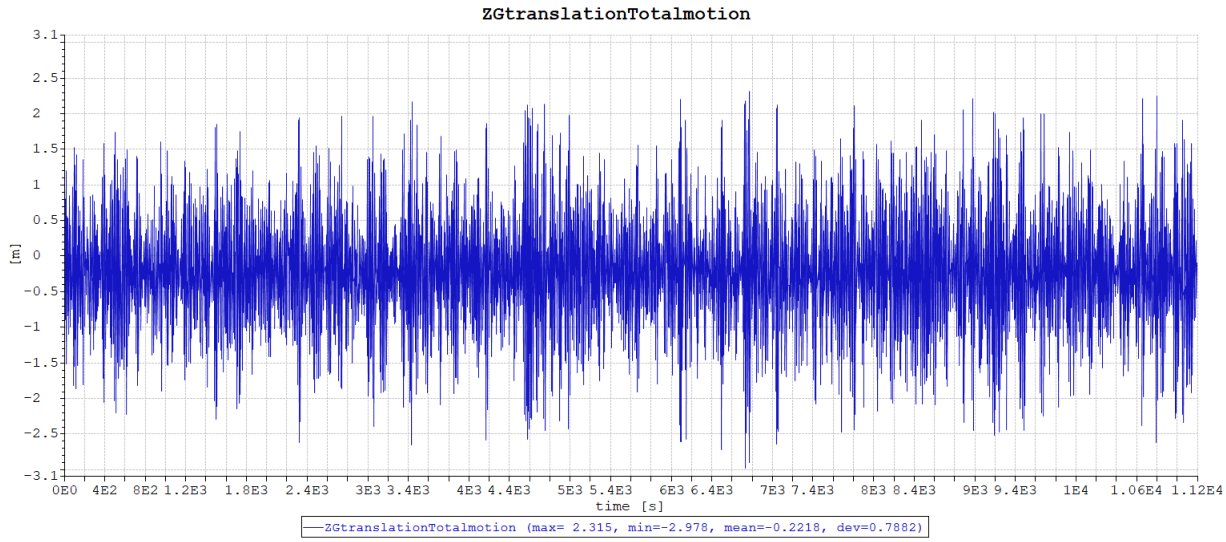

Figure C.3: Time series of heave motion of the FWT.

C.1.4 Pitch motion of FWT

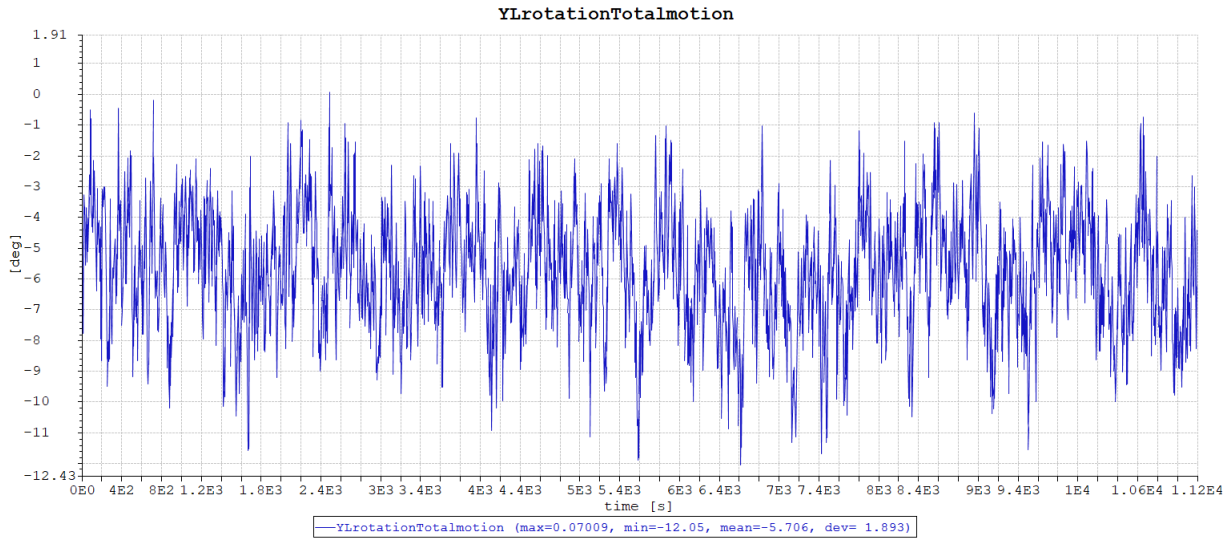

Figure C.4: Time series of pitch motion of the FWT.

C.2 ULS Load Case 2

C.2.1 Tension in mooring line 1

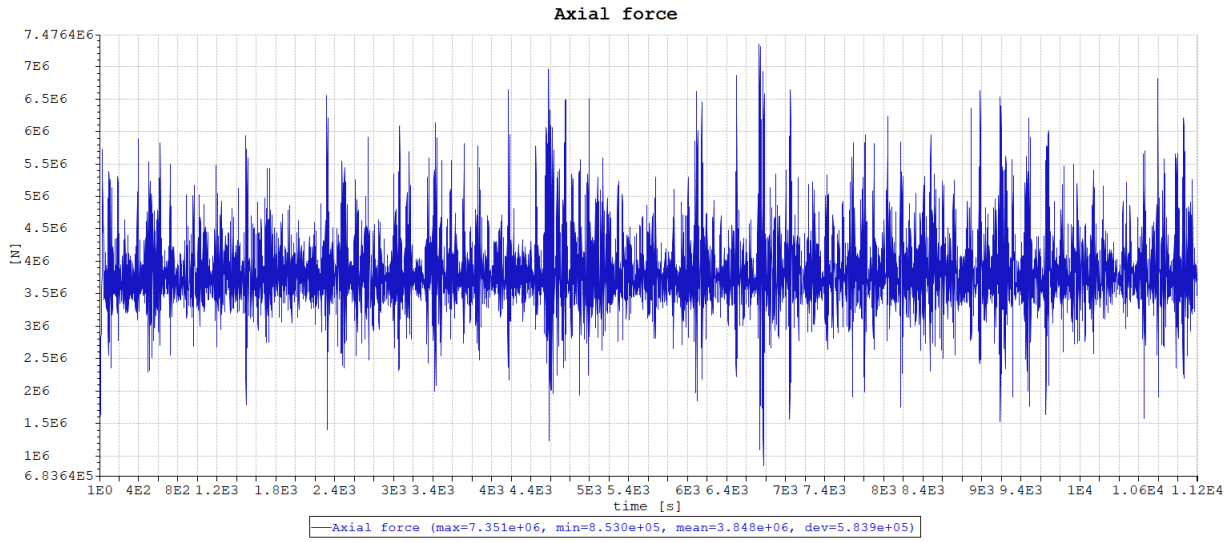

Figure C.5: Time series of tension in mooring line 1.

C.2.2 Surge motion of FWT body

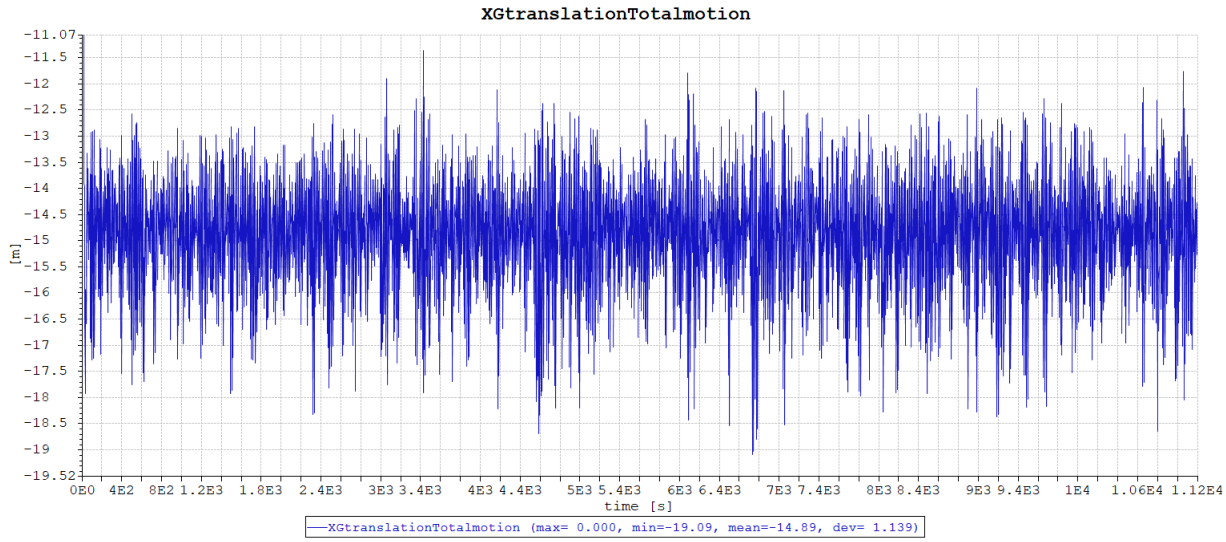

Figure C.6: Time series of surge motion of the FWT.

C.2.3 Heave motion of FWT body

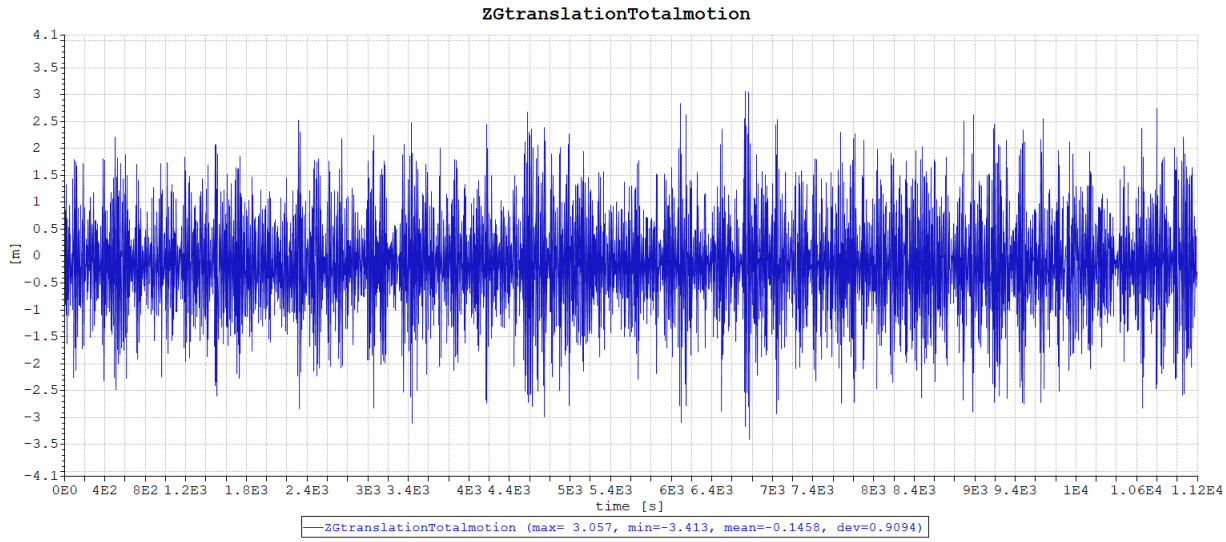

Figure C.7: Time series of heave motion of the FWT.

C.2.4 Pitch motion of FWT

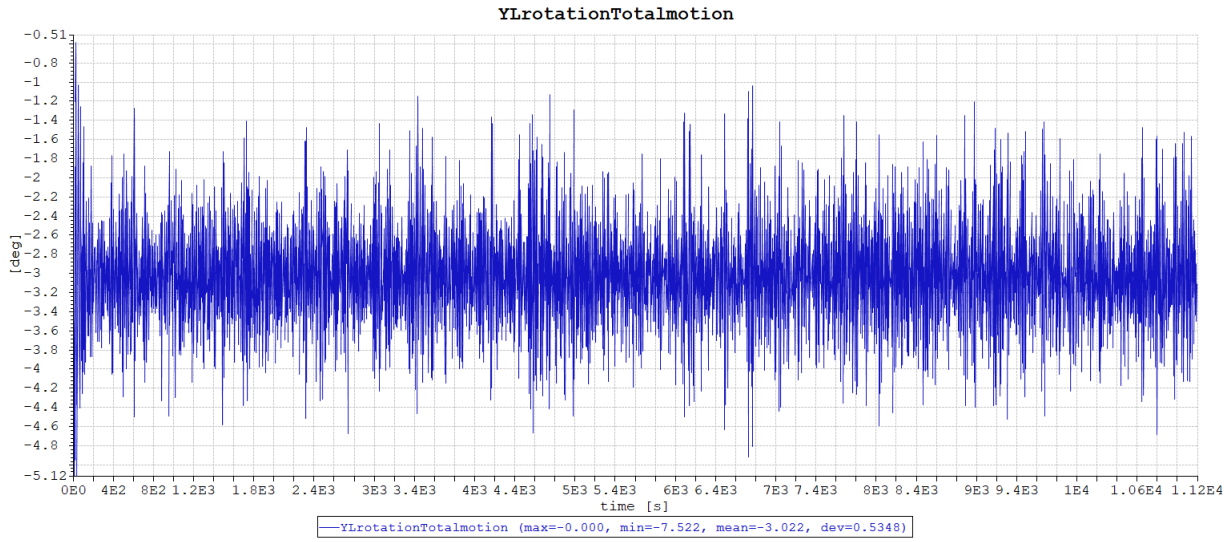

Figure C.8: Time series of pitch motion of the FWT.

C.3 ULS Load Case 3

C.3.1 Tension in mooring line 1

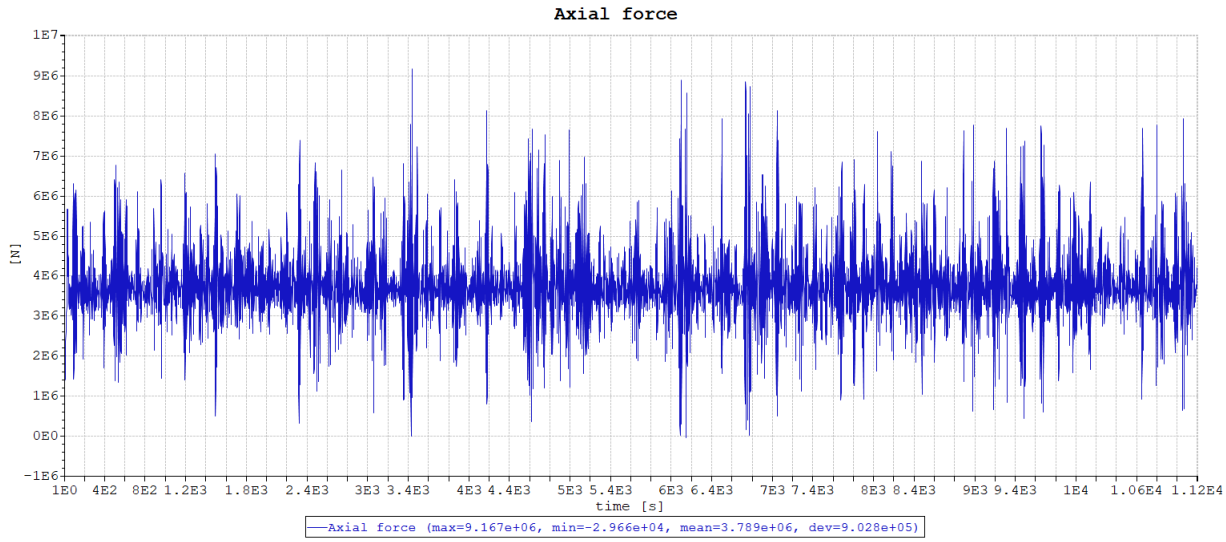

Figure C.9: Time series of tension in mooring line 1.

C.3.2 Surge motion of FWT body

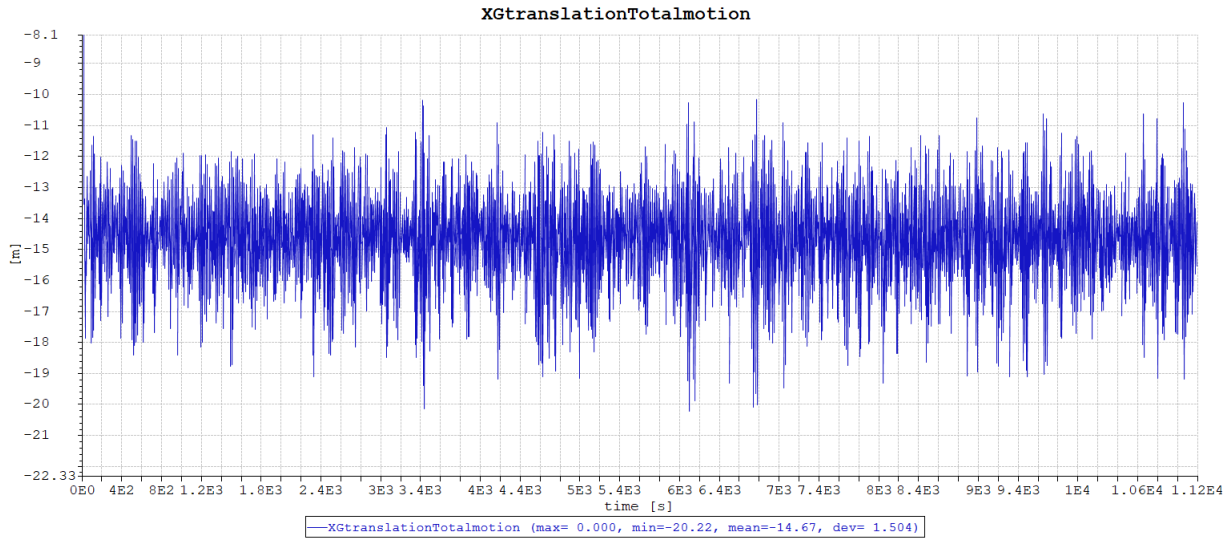

Figure C.10: Time series of surge motion of the FWT.

C.3.3 Heave motion of FWT body

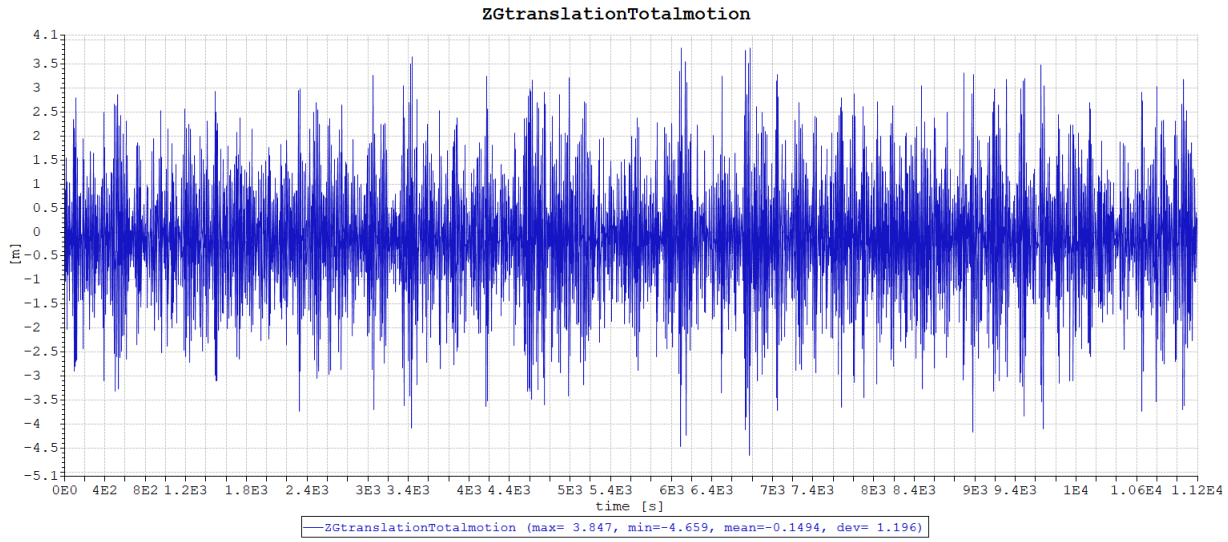

Figure C.11: Time series of heave motion of the FWT.

C.3.4 Pitch motion of FWT

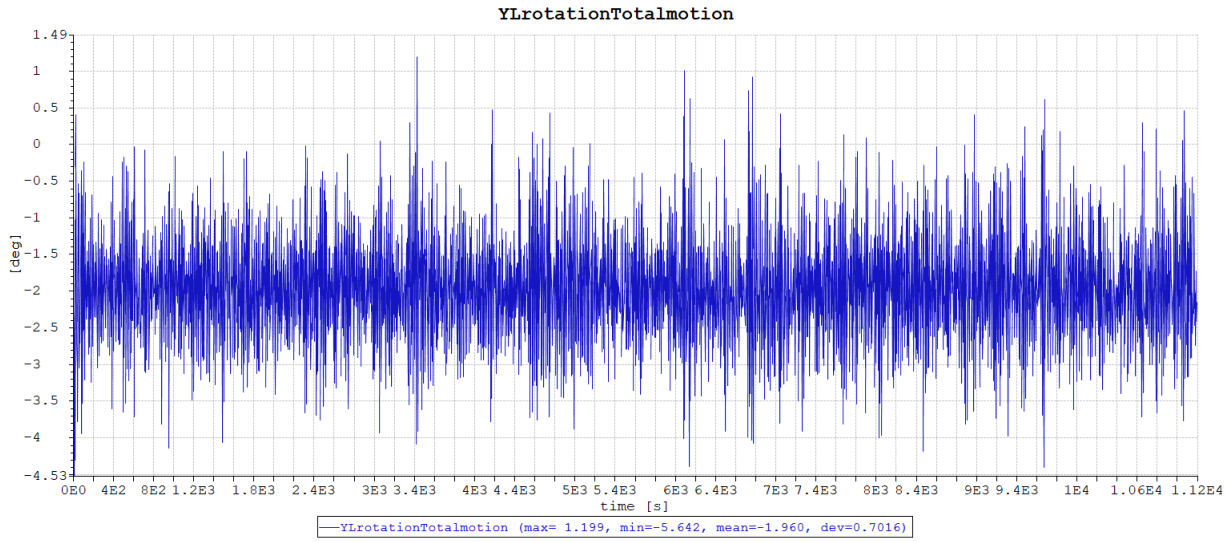

Figure C.12: Time series of pitch motion of the FWT.

C.4 ULS Load Case 4

C.4.1 Tension in mooring line 1

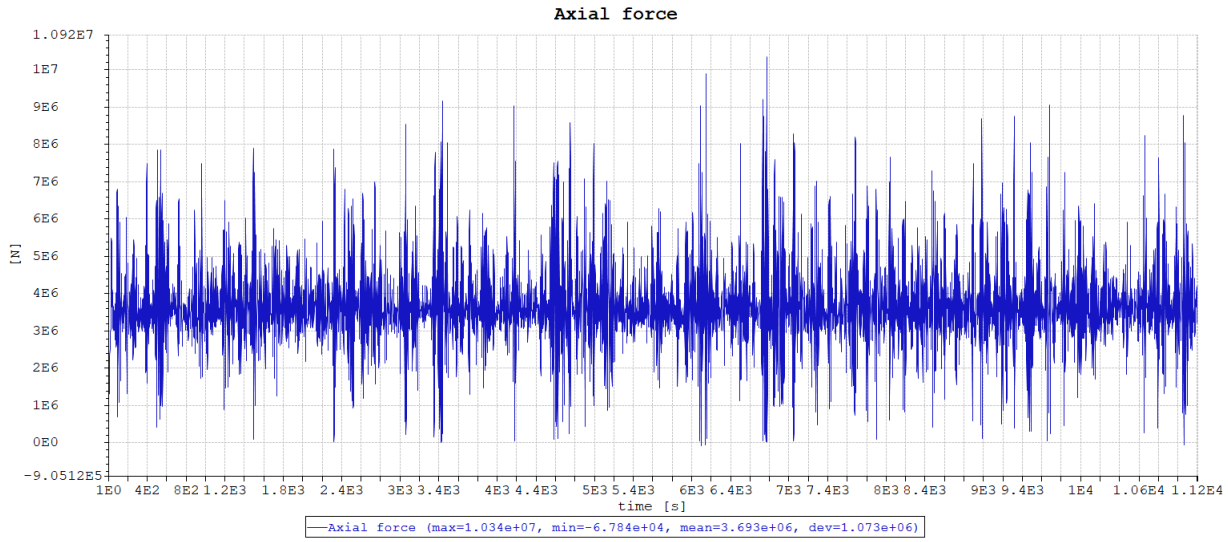

Figure C.13: Time series of tension in mooring line 1.

C.4.2 Surge motion of FWT body

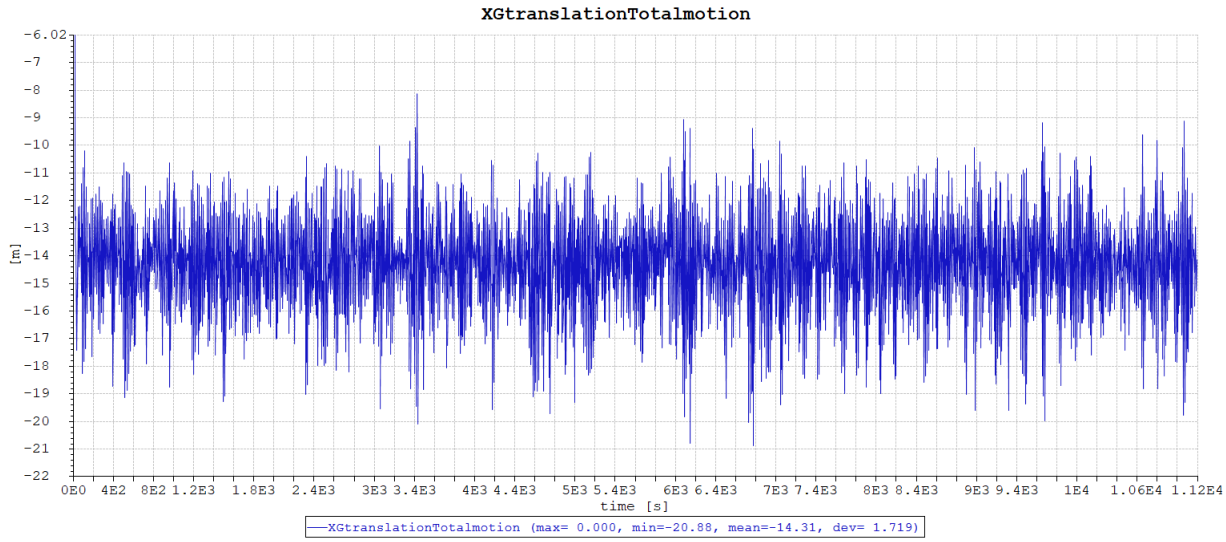

Figure C.14: Time series of surge motion of the FWT.

C.4.3 Heave motion of FWT body

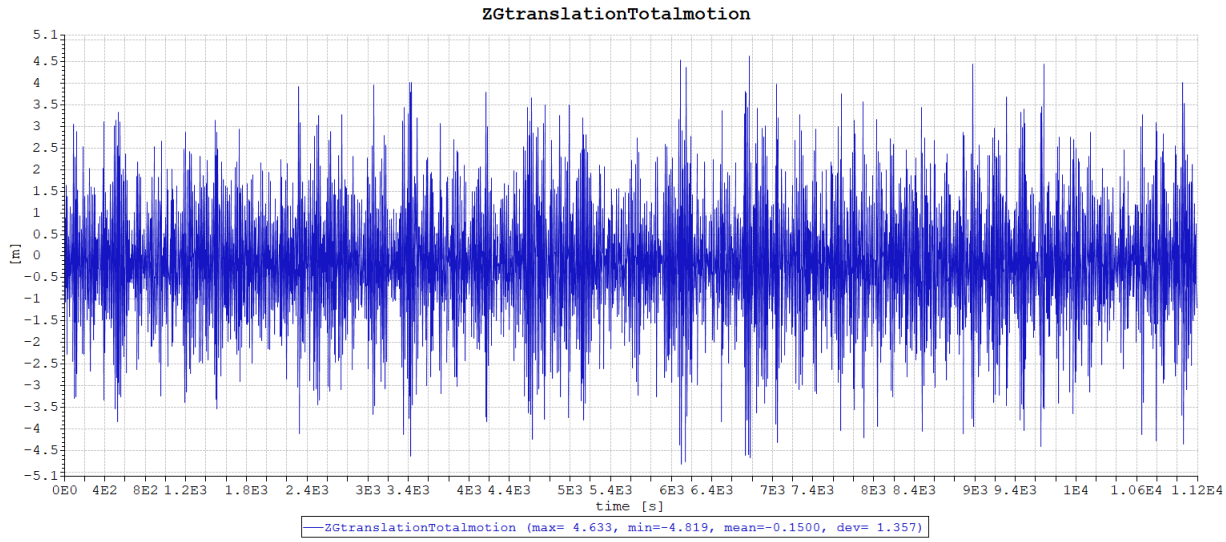

Figure C.15: Time series of heave motion of the FWT.

C.4.4 Pitch motion of FWT

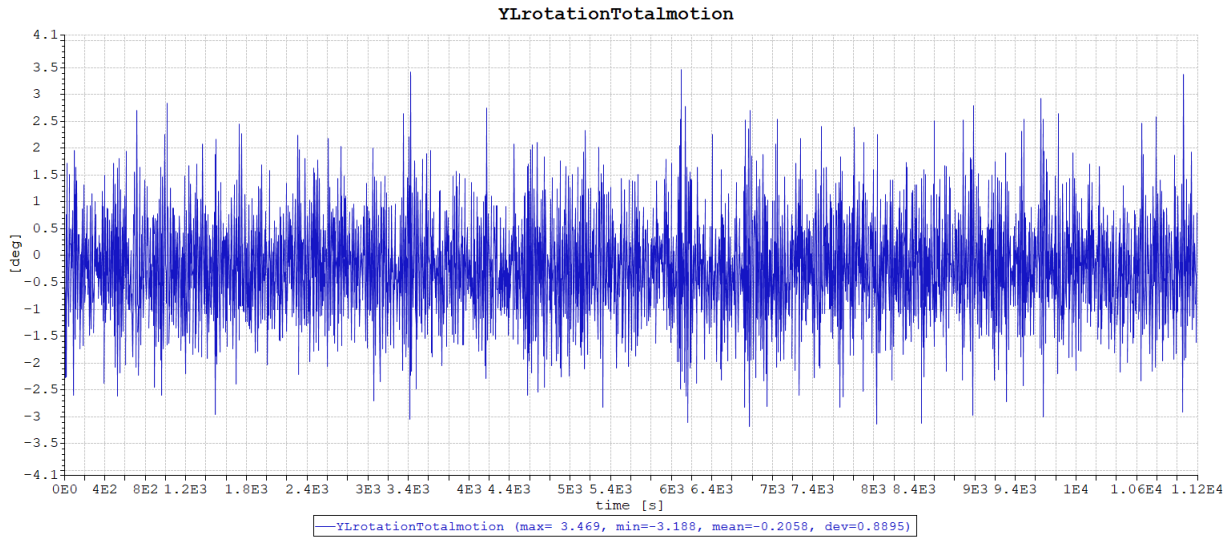

Figure C.16: Time series of pitch motion of the FWT.

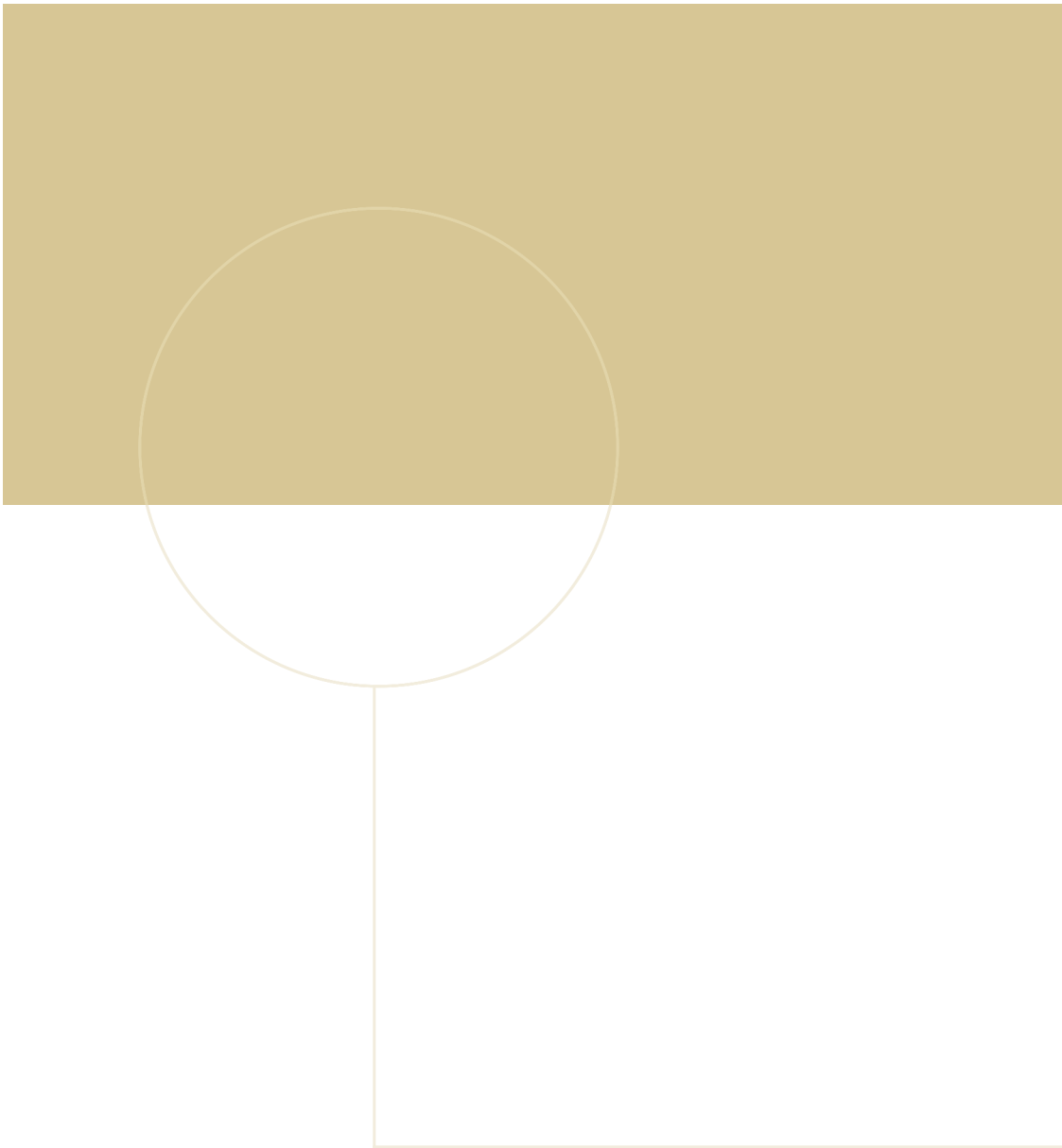

NTNU
Norwegian University of
Science and Technology